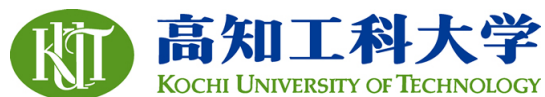


Title	Study on Dynamic Analysis and Wearable Sensor System for Golf Swing
Author(s)	LI, Zhiwei
Citation	高知工科大学, 博士論文.
Date of issue	2015-03
URL	http://hdl.handle.net/10173/1281
Rights	
Text version	ETD



Kochi, JAPAN

<http://kutarr.lib.kochi-tech.ac.jp/dspace/>

Study on Dynamic Analysis and Wearable Sensor System for Golf Swing

A Thesis Submitted for
the Degree of Doctor of Philosophy.

Mail : 166008j@gs.kochi-tech.ac.jp
Present on Spring 2015
Kochi University of Technology
Doctoral Program
Engineering Course

Applicant of Dissertation defense

Zhiwei LI



The Thesis Defense Committee :

Prof, Yoshio INOUE (Supervisors)
Associate Prof, Kyoko SHIBATA (Co-supervisor)
Prof, Masahiro FUKUMOTO (Co-supervisor)
Prof, Shuoyu WANG
Prof, Koichi Oka

12th, February, 2015

Acknowledgements

My deepest gratitude goes first and foremost to my supervisor Prof. Yoshio INOUE, who provided me with his enthusiastic suggestions and advice to support my research works, for his constant encouragement and guidance in my pursuing the Ph.D. He gave me the chance to continue doctoral course and guided me all the 3 years. Without his consistent assistance and instruction, this thesis could not have reached its present form. His ethos of dedication and perfectionism to work will have a far-reaching impact on my life. I also have appreciated your advice for not only this dissertation, but also my future career that I would not have obtained anywhere except from you.

Next, I am very grateful to my Co-supervisor Associate Prof. Kyoko SHIBATA and Prof. Masahiro FUKUMOTO, who gave me so many useful suggestions about the research in every discussion meeting. Thank Prof. Shuoyu Wang and Prof. Koichi Oka for their insightful comments on my research. Many valuable advices were gotten from them at assessment of doctoral dissertation, so this thesis can be improved. And thanks to Dr. Kunihiko TACHIBANA, golf research team and all other members of Inoue laboratory, thanks for three years supporting and accompanying, without you guys, none of this would be possible. I will miss every one of you.

As a SSP student, I would like to appreciate Kochi University of Technology for supporting my life during abroad study. I would also like to express my thanks to all staff in the IRC. Your hard work really touched me, and make me feel cheerful in Japan. All things happened in the past three years, happiness or sadness, have filled a large part of my life.

Last, but not least, I would like to appreciate my parents for their selfless love and support to my life all along. I also owe my sincere gratitude to you who gave me all your attention, touch and time.

Kami city, 4 February 2015

Lee.

Abstract

The dynamics research on the golf swing has been the subject of scientific debate for many years but there is little consensus regarding if golfers could benefit from releasing their wrists in the swing motion as a “late hitting”. The effect of the acceleration pattern on impact outcome has not been ascertained. The aim of this thesis was to determine and explain the mechanism of the release point of the golf swing and the effect of parameters of golf club on body kinematics key performance indicators including club head speed, impact location and launch conditions.

For this purpose, initially, the *Lagrangian* method is used to obtain two coupled differential equations describing the motion of a double pendulum swing model. It is found that wrists begins to uncocking when the angular velocity of the arm and the centrifugal force become to be sufficiently large compared to the angular acceleration and tangential inertial force, uncocking begins naturally without driving torque applied to the wrist joint. However, the increasing acceleration before release point, using a resistive wrist torque, provided a small benefit in terms of increasing club head speed at impact, but the percentage gain in club head speed was approximately half that previously reported by other researchers. Then, based on a new golf club model, equations of elemental parameters, such as mass and length of shaft, gravity center of club, and inertia moment of wrists, are removal of units by nondimensionalization method. Finally, variation trends of club parameters and their effects on the cock angle and the active wrist torque at the release point is verified in simulation.

A follow-up study involved design and motion plan of a golf swing robot to investigate human swing motion. From top position to impact position, swing motion is mapped into the output of a harmonic oscillator based on energy control strategy. And a proportional plus gravity and torque compensation controller was designed to brake the robot. Simulation study indicates validation of the controllers. In simulation study, corresponding to head speed of 24.78 m/s at impact position ($t_m = 0.425 \text{ s}$), the energy level reached at 237.24 J compared to theoretical impact speed 25 m/s and energy level 240 J , respectively. With the same desired parameters, experimental study shows that the impact speed equals to 22.45 m/s , and time consumption from top position to impact position is $t_m = 0.423 \text{ s}$. Though there are slight derivations of the

Acknowledgements

physical golf swing from the simulated trajectories, it is clear the experiment is consistent with the simulation and bears out the validity of proposed controllers.

At last, a quantitative evaluation system for golf swing was presented which incorporates wearable motion sensors to obtain inertial information and provides feedback on the swing quality. The sensors are placed on the player's wrists and lower limb which capture the unique movements of a swing motion. A Kalman filtering based joint angle measurement method with the wearable sensor system was developed to reduce joint angle error caused by offset drift of gyroscope. The wearable sensor system accurately measures the golf swing motion of two subjects. The data obtained by this system can be related quantitatively to skill criteria as expressed in respected golf textbooks. During experiment, a optical motion analysis system worked as reference system. In the process of motion analysis, a Kalman smoothing algorithm was proposed to improve estimation of joint kinematics based on measured marker trajectories. Compared with global optimization method, estimation errors for the joint moments were decreased by more than 30%. Compared with local marker estimation method, estimation errors for the joint moments were decreased by 50%.

Contents

Acknowledgements	i
Abstract	iii
List of figures	xiii
List of tables	xvii
1 Introduction	1
1.1 Research background	1
1.2 Outline	2
2 Literature review	7
2.1 Introduction	7
2.2 Modelling the golf swing	8
2.2.1 Double Pendulum Model	8
2.2.2 Three segments models	13
2.2.3 Three dimensional model	16
2.3 Mechanical properties of a golf shaft	19
2.3.1 Mass and density	20
2.3.2 Golf club length	20
2.3.3 Swing robot	21
2.4 Wearable sensors	22
2.4.1 Motion and position sensors	23
2.4.2 Force and pressure sensors	24
2.5 Summary	25
3 Dynamic Analysis for the Release Point of the Golf Swing	27
3.1 Introduction	27
3.2 The Double Pendulum Model	28
	ix

Contents

3.2.1	Conditions of release	31
3.2.2	Effect of parameters of golf club	34
3.3	Results	37
3.3.1	Conditions of release	37
3.3.2	Effect of parameters of golf club	41
3.4	Discussion	44
3.5	Summary	46
4	Marker-based Tracking Method	49
4.1	Introduction	49
4.2	Optical Tracking Systems	50
4.2.1	Feature extraction	53
4.2.2	Pinhole camera model	54
4.2.3	3D reconstruction	57
4.3	Materials and Methods	58
4.3.1	Kalman Smoothing Algorithm	58
4.3.2	Simulation	60
4.3.3	Experiment	63
4.4	Results	64
4.5	Discussion	66
4.6	Summary	68
5	A Golf Swing Robot to Simulate Natural Release	71
5.1	Introduction	71
5.2	Structure of the Prototype	72
5.3	Material and Methods	75
5.3.1	Swing motion capture based on the optical system	75
5.3.2	Principle of motion control	77
5.3.3	Realization of motion control	82
5.4	Results	83
5.4.1	Simulation	83
5.4.2	Experiment	85
5.5	Discussion	86
5.6	Summary	91

6	Kinematical Analysis of Golf Swing using Wearable Sensor System	93
6.1	Introduction	93
6.2	Coordinate Systems and Transformation	95
6.2.1	Translation in three-dimensional space	95
6.2.2	Rotations about the coordinate axes	96
6.3	Material and Methods	98
6.3.1	Wearable sensor system for upper limbs	99
6.3.2	Wearable sensor system for upper limbs	102
6.3.3	Signal fusion method for wearable sensor system	104
6.3.4	Experiments	108
6.4	Results	110
6.4.1	Validation of Kalman filter for lower limb measurement	110
6.4.2	Kinematical analysis and measurement for swing motion	112
6.5	Discussion	114
6.6	Summary	115
7	Conclusion	117
7.1	Overview	117
7.2	Summary	117
7.2.1	Dynamic analysis for the release point of the golf swing	117
7.2.2	Motion plan of a golf swing robot	118
7.2.3	Measurement and analysis of golf swing with wearable sensor system . .	118
	Bibliography	127
A	Appendix-List of Publications	129

List of Figures

2.1	Approaches commonly used in golf swing modelling study	9
2.2	Double pendulum model of the golf swing	9
2.3	Some of the weakness at the takeaway of left arm only swing	13
2.4	Examples of upper body swing model	17
2.5	Examples of full body swing model	18
2.6	Definition of club length	21
2.7	Commercial golf robots	22
2.8	Inertial sensors	23
2.9	M3D system	24
3.1	Double pendulum model of golf downswing	29
3.2	Combination of moments	29
3.3	Relationship between acceleration inclination	29
3.4	A golf club model	34
3.5	Three different acceleration patterns	39
3.6	Relationship between time and acceleration pattern during downswing	39
3.7	Relationship between time and acceleration pattern during downswing, acceleration is increasing	39
3.8	Relationship between time and acceleration pattern during downswing, acceleration is decreasing	39
3.9	Components of muscle power and joint-force power	40
3.10	Components of energy for the club segment as determined by integrating the respective power	40
3.11	Components of energy for the club segment as determined by integrating the respective power	40
3.12	Components of energy for the arm segment as determined by integrating the respective power	40
3.13	Effect of the active wrist torque τ on the normalized parameter λ	41

List of Figures

3.14 Effect of the normalized mass of the head μ_H/μ_{H0}	41
3.15 Effect of the normalized mass of the grip μ_W/μ_{W0}	42
3.16 Effect of the normalized mass of the shaft μ_S	42
3.17 Effect of the normalized mass of the shaft μ_S/μ_{S0}	42
3.18 Effect of the normalized mass of the head m_H/m_{H0}	42
3.19 Effect of the normalized club length γ/γ_0 without balanced mass of the club . .	43
3.20 Effect of the normalized club length γ/γ_0 with balanced mass of the club	43
3.21 Effect of the normalized supplementary angle of the cock angle α/α_0	43
3.22 Effect of the normalized mass of the grip	43
4.1 Vicon MX camera	51
4.2 ARTTRACK System	51
4.3 Raptor-4 Digital Realtime system	52
4.4 Optotrak certus motion capture system	52
4.5 Pinhole camera model	54
4.6 Similar triangles of a pinhole camera model	54
4.7 Transformation between the camera and world coordinate frame	56
4.8 Epipolar geometry	58
4.9 Time trajectories of the simulated STA for the markers on the body	61
4.10 Markers used to capture the motion	63
4.11 Estimates of angular position, velocity, acceleration and jerk	66
4.12 Estimates of angular positions and internal joint moments with instrumental errors	67
4.13 Estimates of angular positions and internal joint moments with STA	68
4.14 Percentage errors for the minimum and maximum internal joint moments using the GOM and KS	69
5.1 Three view diagram of supporting frame	72
5.2 Prototype of golf swing robot	73
5.3 Manipulator part of swing prototype	74
5.4 Key moments and phases of the golf swing	75
5.5 Placing swing prototype in the capture volume	76
5.6 Lateral view of the swing plane	78
5.7 Coordinates transformation	78
5.8 Control architecture	83
5.9 Swing phase of prototype	84

5.10 Simulation results of the golf swing with a impacting speed of 24.78 m/s	85
5.11 Swing phase of prototype	86
5.12 Experiment results of the golf swing with a hitting speed of 25 m/s	87
5.13 Swing phase of prototype	88
5.14 Simulation results of the golf swing with a hitting speed of 24 m/s	88
5.15 Swing phase of prototype	89
5.16 Simulation results of the golf swing with initial angular velocity of the wrist . .	89
5.17 Swing phase of prototype	90
5.18 Simulation results of the golf swing with initial angular velocity of the wrist . .	90
6.1 Transformation of a rigid body	96
6.2 Transformation of coordinate systems	97
6.3 Motion capture system	99
6.4 Motion sensor for golf swing	99
6.5 Definiation of gait phases	102
6.6 Position and coordinates of the sensor units	103
6.7 Signal processing blocks for motion analysis	104
6.8 Structure of Kalman filter	105
6.9 Definition of gait cycle	108
6.10 The lower limb model	108
6.11 Experimental subject and wearable sensor system	110
6.12 Comparison of the ankle joint angle	111
6.13 Comparison of the knee joint angle	111
6.14 Comparison of the hip joint angle	111
6.15 Joint angle measurement at slow walking speed	111
6.16 Joint angle measurement at normal walking speed	112
6.17 Joint angle measurement at fast walking speed	112
6.18 Data from upper sensor system	112
6.19 Measurement angles of golf swing in the local coordinate system	113
6.20 Measurement displacement of golf swing with camera motion capture system .	113

List of Tables

2.1	Mass ranges of golf shafts	20
3.1	Parameters of swing model	30
4.1	Marker error	64
4.2	Percentage errors for the estimates of the generalized co-ordinates	65
4.3	Percentage errors for the estimates of the generalized accelerations	65
4.4	Percentage errors for the joint moments	66
5.1	Parameters of the swing prototype	73
5.2	Parameters of the DC motor and gear head	74
5.3	Parameters of the swing prototype	76
5.4	Parameters of servo controller	83
6.1	Technical specifications of sensor system	100
6.2	Anatomical coordinate system definitions for the lower limb model	109
6.3	Comparison of evaluation results between with and without Kalman filter (<i>KF</i>)	114

1 Introduction

1.1 Research background

The dynamics of golf swing have been studied for many decades in an effort to improve the swing skills of golf players and to optimize the design of a golf club.

However, there has been much modelling and computer simulation of the golf swing, recording of data from golf players and instrumented clubs, attempts to quantify or categorize subjective impressions and other studies of components of the swing, yet understanding of the golfer's interaction with the club is still too crude to fit clubs to people properly [Farrally and Cochran(2003)]. Sophisticated analyses and simulations help understanding and optimising the technical aspect of equipment, but often human factors cannot be included in this process. This leaves the question of whether possible reactions of the human to changes in the equipment may invalidate the boundary conditions that were assumed in the isolated analysis and optimisation of the equipment. In case of the golf swing, various equipment factors have been subject to scientific analysis and debate. Examples include the golf ball [Li and Tsubokura(2014)], the face of the club head, [Winfield and Tan(1996)] and the shaft, [Milne and Davis(1992b)]. Yet, knowledge of how changes in any of these equipment properties affect the reaction of the player is often limited [Farrally(1999)], and it has been suggested that golf research should take a more holistic approach [Dillman(1994)]. Recently, wearable system combined with inertia sensors such as accelerometers, gyroscopes, and magnetic sensors draws more and more interest both in the sports and medical field. These sensors have been widely used to estimate body segments postures and orientations [Liu et al.(2011)Liu, Inoue, and Shibata]. Examples include the Pressure sensors have been widely used to estimate the values and the distribution of normal ground reaction

forces in the stance phase of a gait cycle [Inoue et al.(2003)Inoue, Matusda, and Shibata]. A wearable ground reaction force sensor system for extrinsic gait variability measurement [Liu et al.(2010b)Liu, Inoue, and Shibata]. Predict and detect localised muscle fatigue, the system which utilises surface electromyography can be used in sports to promote muscle growth or prevent injury [Mulla et al.(2011)Mulla, Sepulveda, and Colley], and there has been research for evaluate wrist rotation in golf by placing with wearable sensors on a golf club and play's body [Ghasemzadeh et al.(2009)Ghasemzadeh, Loseu, and Jafari]. Based on this, considering that human factors as well as mechanical behaviour, the general scope of this thesis is an dynamic evaluation of golf swing.

Most relevant for the majority of golfers may be the question of whether a wearable sensors system has the potential to help them perform better. This thesis therefore focuses on the a simple double pendulum model which describes what happen before release point, and the reaction of acceleration patterns to changes in golf club parameters. It is the purpose of this thesis to enhance understanding of the golf swing both in terms of performance and the underlying mechanisms that may lead to performance effects.

1.2 Outline

The thesis is organised in seven chapters consisting of a statement of the aims and objectives (Chapter 1), a literature review (Chapter 2), a discussion of mathematical model of golf swing (Chapter 3), a Kalman smoothing algorithm to improve estimates of reflective marker trajectories based on a camera motion capture system (Chapter 4), a golf swing prototype design and related experimental study (Chapters 5), a application study with designed wearable sensor system for golf swing motion (Chapter 6), and conclusions (Chapter 7).

Chapter 2 This chapter aims to present a summary of the current state of golf dynamics research in order to identify areas in which further research is needed. It describes the main properties of the dynamics of golf swing and discusses methods to characterise and simulate their effect. This is followed by a summary of the current state of research into the relationship of these mechanical properties with performance variables. The chapter concludes with the identification of key areas where more research is required and is followed by a definition of more specific aims for this thesis (Chapter 3).

Chapter 3 This chapter discusses the methodological aspects of this thesis in more detail, beginning with study design considerations. In order to clarify the mechanism of the release point of the golf swing and the effect of the parameters of a club and a human body on dynamic behavior at the release point. First, the mathematical model of the golf

swing is assumed to be a 2-dimensional double pendulum connected with a nonlinear rotational spring at the wrist joint. By applying *Lagrange* equation to this system, equations of the golf swing motion were derived. Assuming that the player's wrist joint begins to turn naturally under the centrifugal force of the swing. When the angular velocity of the arm and the centrifugal force become to be sufficiently large compared to the angular acceleration and tangential inertial force, uncocking begins naturally without driving torque applied to the wrist joint. Considering that uncocking begins naturally without driving torque applied to the wrist joint the angular velocity of the arm and the centrifugal force become to be sufficiently large compared to the angular acceleration and tangential inertial force. Establish the approximate equations which express the relationship between angular velocity and acceleration at the release point. Based on simple equations and different acceleration patterns of the down swing, calculation methods are derived to estimate the effect of the acceleration patterns expressed by the polynomial of time on the dynamic behavior at the release point which may affect significantly on the head speed. According to the results of simulation, we discussed two type acceleration patterns which are expressed by the 1st order function of time affect to the release point. Through the discussion, it can be seen that acceleration pattern which has positive gradient gives high angular velocity of the release point and later release point, and negative gradient pattern shows low angular velocity and earlier release point and these results can explain mechanism of so-called late hitting. Then, simplified equations which express the relationship between angular velocity and acceleration at the release point were derived. Based on derived equations and the motion control equations, mathematical expressions that demonstrate the effect of the parameters of a golf club on the dynamic behavior at the release point were deduced. According to the expressions, parameters (e.g. lengthen of shaft, gravity center of shaft, and head weight) of a golf club affects significantly on the head speed, and calculation and discussion are carried out on the effect of the parameters of the club, the cock angle and the active wrist torque on the release point. Through the discussion, it can be seen that the derived simple approximate equations exhibit a physical insight of the phenomena at the release point and will be helpful to understand the effect of the club parameters on the dynamic behavior of the double pendulum at the release point.

Chapter 4 In this chapter, kinematic analysis is performed to obtain both the linear and rotational accelerations of each model segment. This is for instance done by tracking small reflective balls by means of multiple synchronized video cameras and reconstructing the motion of the points from the images. However, the main complications associated

with creating the link between measured marker trajectories and the multi-body model are noise, kinematic over-determinacy, kinematic under-determinacy, missing marker visibility. Aim to that, a new method for kinematic analysis of rigid multi body systems subject to holonomic constraints was designed. This is accomplished by introducing a constrained optimization problem with the objective function given as a function of the set of system equations that are allowed to be violated while the remaining equations define the feasible set.

Chapter 5 Based on the double pendulum mode, take club speed and dynamic energy transition at impact into consideration, simulate different situations (specifically on the release point and patterns of uncocking) according to various parameters and variables (including patterns of torque, length ratio of club shaft to wrist, mass ratio of club shaft, and uncocking angles). A new golf robot with one actuated joint and one passive joint was designed to simulate the natural uncocking progress during swing. Considering that the special mechanism with the non-holonomic constraint of swing robot and the high speed motion, a energy level controller was designed to drive the rotation of a 250 *watt* DC motor with different desired parameters. The methodology is divided into two parts which is software development and hardware implementation. The works in software development are calculation of DC motor transfer function, simulation to determine the parameters value of controller and developing the software controller.

Chapter 6 Golf requires a complicated sequence of motions to swing the golf club properly with the primary goal of propelling the golf ball a certain distance in a desired direction. A proper golf swing can make the difference between a long straight ball flight and a shorter hook or slice as a result of an improper swing. A repeatable and consistent golf swing can also dramatically improve a golfer's score. However, this single movement which has such a major impact on the player's overall game is difficult to master and execute consistently for players who are new to the sport or have little experience. To resolve all of these complications, players who are serious about their game seek out instructors, golf instructional books, or other training aids to help them to obtain the "perfect" golf swing. These players can potentially benefit from wearable sensor systems where information on the quality of the performed swing can be provided in real time. Such a system must be mobile to be usable at the location where the sport takes place. In this research, a wearable sensor system was designed for velocity, acceleration, and energy transition measurement during golf swing. The sensor nodes collect data for the sequence of actions in a swing which is then preprocessed locally to facilitate subsequent in network operations. The data is then sent to a base station for further

analysis. At the base station, the quality of each segment is expressed as the amount of deviations from target line. In order to realize a simplified swing analysis system using wearable sensor system. A joint angle measurement method using Kalman filter to correct gyroscope signals from accelerometer signals was examined in measurement of play's wrist and thumb with the wireless wearable sensor system, in which sensors were attached on the body instead of on the golf shaft. In the measurement, Kalman filtering based measurement method was examined with the wearable sensor system during golf swing to reference data obtained from an optical camera system.

Chapter 7 Finally, This chapter draws general conclusions from research studies.

2 Literature review

2.1 Introduction

Considering that previous golf have already covered field, e.g. sports injuries in golf game [McHardy and Pollard(2006)], muscle activity during the golf swing [Dao and Tho(2014)], the biomechanics of the golf swing [McHardy and Pollard(2005)], and the general physics of the golf swing [Penner(2003)]. None of these reviews have specifically focused on the use of modeling and simulation to understand the dynamic aspects of the golf swing.

The purpose of this chapter is to classify relevant mechanical properties of golf club and critically review and classify published scientific studies that have examined the biomechanical models and simulations of the golf swing. Given the number of previous models, such a review could potentially be useful in giving suggestions and guidelines for future research.

The literature review begins with descriptive information characterising typical modelling and simulation methods which used in golf dynamic analysis. Following on from this, parameters of the golf club are described in detail, with a basic focus on the strength and weaknesses of the research methods currently used in practice. A full understanding of the modelling and simulation methods involved is deemed an important basis for biomechanical analysis. Following the discussion of wearable sensor techniques used in golf swing research. The final section of the chapter highlights the limitations of the current understanding of relationships between modelling properties and swing performance.

2.2 Modelling the golf swing

2.2.1 Double Pendulum Model

When the behavior of a system is too complex to be explained by an observer, it is useful to reduce the system to its essential elements in order to simplify and solve a research problem associated with it. The process of defining a representative alternative system is commonly referred to as ‘modeling’ [Dao and Tho(2014)], whereas the application of this model, such as run virtual experiments, is associated with the term ‘simulation’ [Dao and Tho(2014)]. In the case of the golf swing, numerous researchers have presented models and simulations using various degrees of sophistication to represent the system. Obviously, the amount of simplifications and assumptions depends on the aims and objectives of each individual project, but in all cases, care needs to be taken to create appropriate models that adequately describe the underlying physics without being too cumbersome. Over-simplifications, as well as too high a degree of fidelity, can make it impossible to use a model to solve a research problem. The true value of a model is being able to extrapolate rather than merely interpolate between observations. This is particularly poignant in multidimensional problems with many degrees of freedom, such as the open system intrinsic to the golf swing. In this context, it appears to be helpful to clearly distinguish between assumptions and simplifications. Throughout this article, the term ‘assumption’ will refer to model characteristics that are believed to resemble reality very closely. For example, it is known that gravity varies depending on geographical position, but is very likely that it is safe to assume that these variations will have no effect on the simulation results of the golf swing; therefore, a constant gravity value is assumed. In contrast to this, simplifications are derivations from reality that could be necessary to make it feasible to create a particular model or compute simulation results in a realistic time. An example of a typical simplification would be that, rather than trying to include all relevant soft tissues, most models of the golf swing deal with the human body as a rigid body system.

Models and simulations appears in in this chapter were classified as follows: (a) the number of spatial dimension (2D and 3D); (b) the number of segments involved in golf swing; and (c) whether an inverse dynamics or forward dynamics approach was chosen. The inverse dynamics solution typically involves the measurement of body movement and ground reaction forces, whereas input of the internal forces is required for the forward dynamics approach so that the output in here, body movement can be calculated as shown in figure 2.1.

In order to gain insight into the basic mechanics involved in the golf swing and to explain the optimal coordination of the swing [Cochran and Stobbs(1968)] suggested a simple model

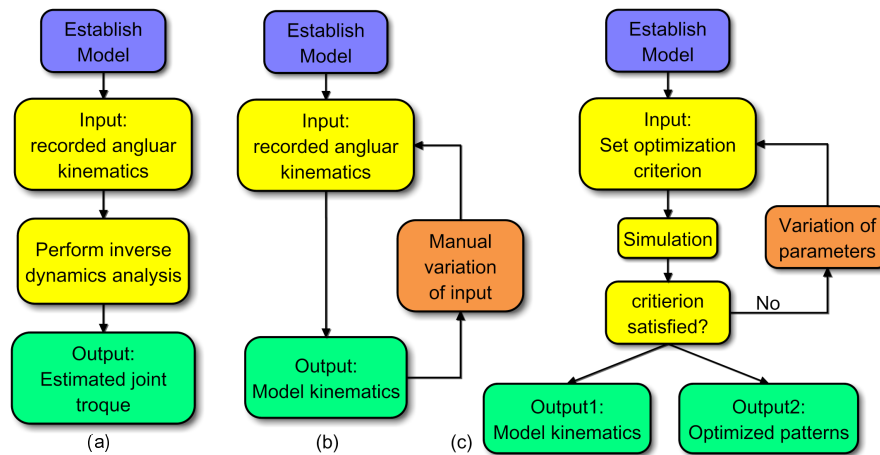


Figure 2.1 – Typical steps involved in (a) inverse dynamics analysis, (b) forward dynamics analysis (with manual or systematic variation of input parameters), and (c) forward dynamics analysis (with optimization algorithm).

of the downswing consisting of a double pendulum (Figure 2.2). They assumed that the two most relevant pivot points of the moving body segments were the wrist and a point roughly corresponding to the middle of the golfer's upper chest [Cochran and Stobbs(1968)]. This imaginary point is taken to be fixed in space and connected to an upper lever that is representative of the arms of the golfer. Another segment, representing the club, was connected to the upper lever via a hinge joint. This wrist hinge was assumed to behave passively, restricted only by a stop that prevented the club segment from moving too far back at the top of the backswing (set up position).

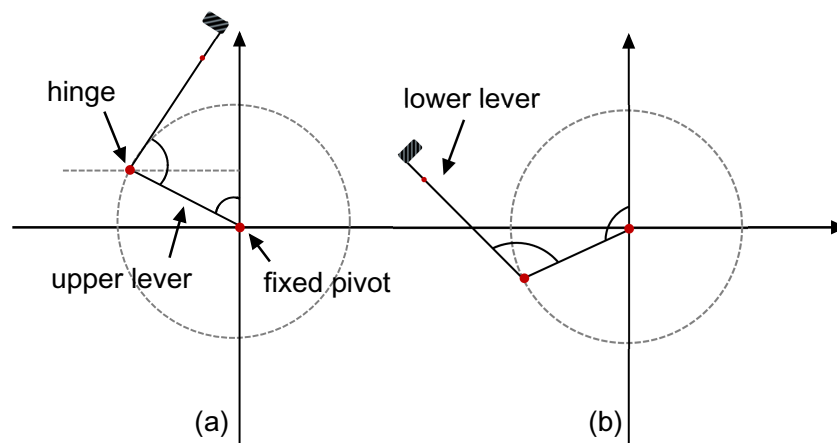


Figure 2.2 – Double pendulum model of the golf swing (a) set up position, (b) swing after wrists uncocking.

Cochran and Stobbs used this model to explain the basic mechanics of the swing and showed

that the combined effect of inertia and centripetal force acting on the lower lever can create a well coordinated downswing if the upper lever is accelerated using the correct force [Cochran and Stobbs(1968)]. In this case, no wrist torque is required to coordinate the rotation about the lower hinge other than the passive torque provided by the stopper in the wrist joint. Based on this observation, the concept of natural wrist release emerged. This concept describes a swing pattern in which no active muscular wrist torque is applied to accelerate the club during the downswing. Instead, the motion of the arm is coordinated in a way that allows the club to accelerate naturally, driven by the centrifugal force acting on its centre of gravity. Cochran and Stobbs presented their model as a simplified mechanical representation of the swing to explain the principles that underlie the golf swing, whereas others successfully used their approach for inverse dynamics analyses [Jorgensen(1999)] and forward dynamics swing simulations. Of these forward dynamics simulations, some applied simplified torque profiles at the fixed pivot and the wrist hinge [Hume et al.(2005)Hume, Keogh, and Reid], thereby keeping the number of input parameters manageable for manual manipulation, whilst others used optimisation algorithms to define more complex input torque profiles for multiple torque generators [Pickering and Vickers(1999)].

The two segments, double pendulum model of the golf swing cannot account for rotations of the arms about the shoulder joint and rotations of the torso as there is only a single body segment representing the arms. Therefore, some researchers have introduced another hinge in the model representing a simplified shoulder joint. These three segments models have been utilised for inverse dynamics analyses of joint torques [Tsujiuchi and Koizumi(2002)] as well as forward dynamics swing simulations [Turner and Hills(1998)]. Furthermore, three segments swing models have formed the basis for a number of studies using optimisation schemes to determine joint torque patterns [Aicardi(2007)]

Inverse dynamics models

[Budney and Bellow(1982)] used a double pendulum model to predict the joint torques that would be required to replicate angular kinematic data recorded from real swings. They then compared two club matching approaches, both aiming to allow the player to use the same swing kinematics for all clubs from the driver to the shortest iron. The first approach was the conventional static swing weight method. The second approach was based on the dynamic swing model and scaled the club masses so that the maximum circumferential force the player has to overcome when accelerating the club would be identical for all clubs within the set. They found that the static method as well as the dynamic club matching would result in a

similar, monotonic progression of club masses throughout a typical set of clubs.

Forward dynamics Models

[Jorgensen(1999)] presented a mathematical simulation model based on the double pendulum approach. One of his aims was to analyze how wrist torque could be used to enhance performance. Using the Lagrangian approach, he described the system with a pair of coupled differential equations. After simplifying these equations, he found that the impact velocity of the club head could be increased if torque was applied at the wrist hinge to prevent the lower lever from changing its position too early.

The double pendulum model has also been applied to study the bending of the shaft throughout the swing [Milne and Davis(1992a)], who included a flexible shaft. They derived simplified ramp torque functions for the wrist and shoulder joints, which were, in the case of the wrist joint, matched to bending moments at the top end of the shaft as recorded with strain gauges. They concluded that the statically measured shaft flexibility does not affect swing kinematics significantly and that common static shaft tests should be replaced by dynamic tests to increase the validity of the tests. Milne and Davis have been criticized for not correctly incorporating the offset of the centre of gravity of the club head in their model. Instead of including the 3-D position of the centre of gravity, they projected it onto the swing plane of their 2-D model using a correction factor obtained from their player testing rather than appropriate torques and forces to change its position relative to the longitudinal axis of the shaft.

[Miura(2001)] used the double pendulum model of the swing to analyze whether a translational displacement of the position of the central rotation axis of the system just before impact could increase impact velocity. Miura noted that skilled players appeared to pull the club towards the rotation axis just before impact (vertical/upwards relative to the global reference frame). Therefore, he created a modified double pendulum model by including an additional translational actuator and found that the club head velocity at impact could in fact be increased by this inward pull.

[White(2006)] used the double pendulum model to revisit the effects of fundamental physical principles on the efficiency of the golf swing. Using an undriven double pendulum model, it was confirmed that arm and club would re-arrange themselves without any active wrist contribution. The author then split the overall stroke efficiency into swing and collision efficiency. Swing efficiency was defined as the fraction of the total kinetic energy of the system that is present in the club head immediately before the collision, and the collision efficiency

was determined as the ratio between ball mass and club head mass. Total strike efficiency was then calculated by multiplying swing efficiency and collision efficiency so that an optimum between the two conflicting factors, swing and collision efficiency, could be found. White then used a modified version of the equations from [Pickering and Vickers(1999)] with a constant shoulder explore the effects of changes of some of the input parameters on stroke efficiency. These parameters were club head mass, shaft length, shaft mass, wrist angle at initiation of the downswing, and time of wrist release. When analyzing the effects of an active wrist torque after wrist release, White that this caused the club head velocity to peak before impact. This demonstrates the limitations of the proposed model as it does not adjust its torque patterns to maintain an efficient swing when the model configuration changes.

[Chaochao and Yoshio(2007)] examined the effect of different wrist torque profiles and ball positions on club head speed at impact. Using the Lagrangian approach, they obtained the equations of motion for a double pendulum swing model. They then applied four different wrist torque profiles: natural release; passive wrist is held rigid until preset negative torque is reached; positive torque is used to accelerate wrist joint after release; and a combination of passive and positive torque. Keeping the maximum torque values constant, the highest impact speed could be achieved using the PAW wrist torque pattern. Because no impact model was included that would cause the club head to slow down after impact, the peak club head speed could always be determined, even if it occurred after the club head passed the intended impact position. It was found that peak club head speed always occurred after the club head passed a neutral tee position. Therefore, right-handed golfers would benefit from placing the tee closer towards their left, which is in agreement with Pickering and Vickers's results. It should be noted that the position of the ball within the stance is also associated with launch conditions rather than just optimal club head speed.

The double pendulum model was used to analyze the effects of a variation of impact position between club head and ball. Pickering observed that for swings performed with an iron, there is an advantage in positioning the ball aligned with the pivot axis of the swing because this results in the club face having a velocity component directed towards the ground [Pickering and Vickers(1999)]. This gives the ball more backspin, which they believe is desirable for iron hits to prevent the ball from rolling too far on the ground after landing. It could be postulated that even more backspin would be achieved if the ball was placed further backward, but this option was not simulated. For drivers, however, another study by Pickering and Vickers provided evidence that higher impact velocities could be achieved if the ball was moved to the left, towards the target.

2.2.2 Three segments models

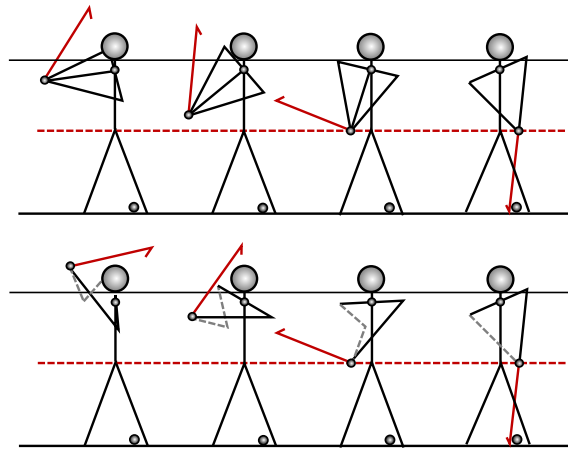


Figure 2.3 – Some of the weakness at the takeaway of left arm only swing.

Obviously, the two segments, double pendulum model of the golf swing does not account for rotations of the arms about the shoulder joint and rotations of the torso as there is only a single body segment representing the arms. Therefore, some researchers have introduced another hinge in the model representing a simplified shoulder joint. [Cochran and Stobbs(1968)] stated that they considered this option when suggesting their model and mention that they found that adding another joint to their model helped to achieve increased club head velocity at impact (figure 2.3). However, they concluded that utilizing another joint would make it more difficult to coordinate the segments in a way that would result in an efficient swing..

Inverse dynamics models

It appears that [Tsuijiuchi and Koizumi(2002)] used an inverse dynamics approach to study the shoulder, elbow, and wrist torques applied during downswings performed by three players. The methods that were used are not described in detail in the paper. They state that marker trajectories were recorded in three dimensions and then projected onto a single plane. The Newton–Euler method was used to derive equations of motion for a three-segment model, including a flexible shaft. However, it is not clear how the slope and position of the projection plane were determined or how the rigid body model was modified to account for the flexibility of the shaft. Tsuijiuchi found that all three golfers analyzed in their study had a negative torque acting in their wrist joints that would slow down the uncocking of their wrists just before impact. There was a weak correlation between the magnitude of this negative torque and shaft deflection, indicating that the forward bending of the shaft at impact could be caused by the torque pattern applied by the player. However, the swing model presented by Tsuijiuchi et

al. was based on a 2-D approach. Neither the off centre position of the club head's centre of gravity nor the wrist rotation that golfers use to square the face before impact was considered. The centre of gravity position of the club head would also tend to cause forward deflection of the shaft at impact. Therefore, in a real swing, the centre of gravity position may cause the forward bending that the authors explained by an active wrist torque

Forward dynamics Models

[Turner and Hills(1998)] proposed a three segments model consisting of a shoulder, arm, and a club segment, all of which move in one plane. After formulating the equations of motion for the system, forward dynamics simulations were run using constant torque settings. The timing of these constant torques was then varied, and the wrist torque manipulated by using a cubic polynomial. The authors then present a number of effects that could be achieved by modifying the torque function.

A study presented by [KR and RE(1985)] was the earliest application of optimum control theory that was found as part of this article. Using Pontryagin's maximum/minimum principle, they predicted torso, shoulder, and wrist torque profiles under different optimization criteria. The first optimization criterion was to achieve maximum impact speed while not exceeding predefined torque limits. The second criterion was to reach a predefined impact speed with minimum mechanical work. The results obtained by Campbell and Reid showed that, with the minimum work optimization criterion, the mechanical work decreased by 67 percent, while impact speed was only reduced by 25 percent at the same time. The presented torque profiles for the more efficient swing showed a notable sequencing of peak torques. In a similar but more comprehensive study design, [Kaneko and Sato(2000)] obtained initial torque profiles by using inverse dynamics. Based on this, they found that a minimum power optimization criterion led to the most accurate torque predictions when applying optimum control theory. They calculated how torque profiles were likely to change when the mechanical characteristics of the club were altered length, mass distribution, and total mass. Their simulations showed how heavier clubs or clubs with a centre of gravity closer to the club head caused increases of the joint torques. When the club length was increased, less power was required to reach the same club head velocity.

[Sprigings and Neal(2000)] used a three segments model to determine whether using active wrist torque to accelerate the club just before impact rather than just releasing the wrist joint passively natural release has advantages for the golfer. Besides including a third segment in their model, they also installed torque generators in the joints that do not neglect the physio-

logical properties of human muscle. Namely, these characteristics include the velocity–force relationship and the maximum activation rates of human muscles. After setting up Newtonian equations of motion for the system, they used an optimization algorithm to find the torque patterns that produced maximum club head velocities under three different boundary conditions. By comparing the results of these simulations, they found that club head speed could be increased if the golfers actively applied a wrist torque accelerating the club just before impact rather than letting the club head accelerate only passively as suggested in previous studies. Unsurprisingly, they were able to demonstrate that if the model configuration was set to ignore physiological muscle limits, higher club head velocities could be achieved. However, the unrealistic, steep changes in joint torque showed that the resulting motion patterns could never be reproduced by real golfers. This shows that the physiological properties of muscle have to be kept in mind when modeling the swing. Using the same model, [Sprigings and Neal(2001)] were able to analyze the mechanical power flow among the segments. They found that there is a proximal to distal power flow with maximum power values reached for the wrist joint. The majority of energy transferred to the club originates from passive joint forces rather than active muscle forces. Additionally, [Sprigings and Mackenzie(2002)] showed that their three-segment model applied more realistic shoulder joint torques than previous two segments models.

[Sprigings and Neal(2001)] describe another application of their model in order to analyze the feasibility of a simple device for club performance testing. This test device consisted of a pendulum where clubs could be mounted and only driven by gravitational force acting on the club after its release. Sprigings and Neal modeled both this simple device, only driven by gravitational torque, and the same set-up, but driven by a more realistic torque function. Their results showed that a simple, one-link pendulum model driven by gravitational torque is not suitable to test the efficiency of new club designs because the results were inconsistent with the more realistic model that included a wrist torque function. By this, Sprigings and Neal present a good example of a model that used too extreme a simplification to create valid results.

More recently, a new approach to manipulate the shape of torque curves when optimizing forward dynamics swing simulations has been suggested [Aicardi(2007)]. This method reduces the number of input parameters to three per joint without restricting the shape of the input torque curve. This was achieved by assuming: constant segment masses and dimensions, that joint velocities and torques at the top of the backswing were zero, that joint torques at impact were zero, that impact would occur at a predefined impact position, and that the joint angles

would change monotonically throughout the downswing. After making these assumptions, an upper torque limit was set for each joint, and maximum impact velocity was used as an optimization criterion. While the previous assumptions could probably be justified based on previous studies, it was also necessary to set the downswing duration to a fixed value so that the optimization could be performed. This does not seem realistic, as it is likely that for an optimized swing with an increased club head velocity the downswing duration would shorten.

[Iwatsubo et al.(2002)Iwatsubo, Adachi, and Kitagawa] presented a comparison of a two link and a four link model of the golf swing. Using the Newton–Euler method, they found the equations of motion for two different swing models and used motion capture data to obtain the joint angle histories of the swings of four golfers. Using inverse dynamics, they calculated the joint torques applied by the golfers. Results for the wrist joint were almost the same for both models. For the shoulder joint, however, some characteristics of the individual swings were no longer distinguishable when using the two-link model of the swing. Iwatsubo et al. concluded that the more complex, four link model of the swing is better suited to analyze the skill level of golf players.

2.2.3 Three dimensional model

Golfers perform their swing in 3 dimensional space, and it is unclear how much the simplified view of regarding the swing as a planar motion influences the results of the studies presented in the previous section. Therefore, potentially more realistic, yet also more complex models have been developed that consider the movement of up to 15 body segments in three dimensional space.

upper body models

An early study of the 3-D kinetics of the golf downswing was carried out by [Vaughan(1981)]. Using inverse dynamics and a rigid model of a golf club, he analyzed the torques and forces applied by four golfers to their clubs. The motion of the club was recorded using two cameras. He found that the players he studied did not swing the club in one static plane. Nevertheless, he confirmed some observations made with the earlier 2-D models of the swing by finding that golfers applied negative torque to the club just before impact causing the hands to slow down and the club head to accelerate . [RJ and BD.(1981)] used an approach similar to Vaughan to determine the 3-D forces and torques applied to the club. They confirmed most of Vaughan's findings, added estimates for shoulder joint forces, and described the angular kinematics of

the club segment in more detail. Interpretation of some of their results is difficult because all kinematic and kinetic data are presented in a global coordinate system rather than in the local club or arm reference system.

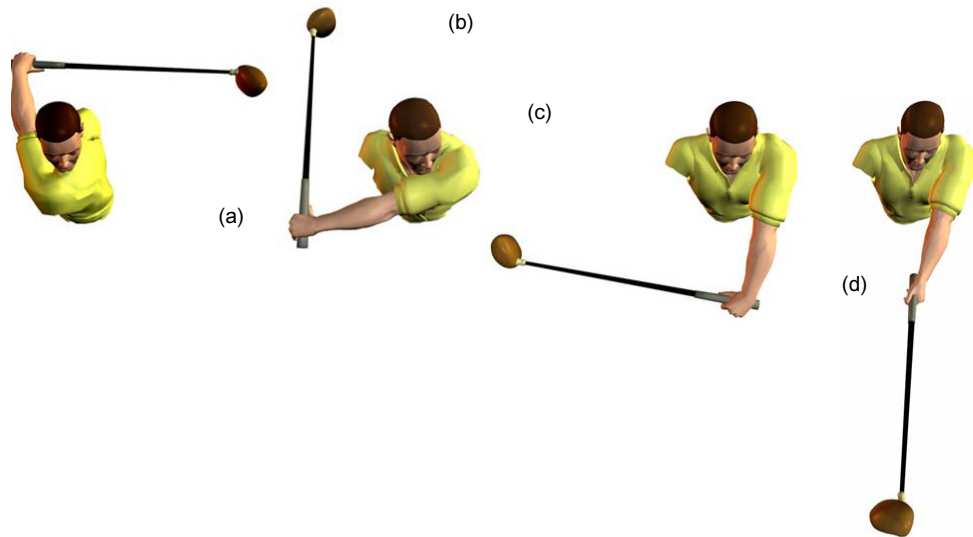


Figure 2.4 – Examples of upper body swing models [MacKenzie(2005)], (a)Position at start of downswing; (b)Torso rotation; (c)Shoulder abduction; (d)Rotation of the lead arm about its longitudinal axis.

While the initial inverse dynamics analyses of the 3D kinetics of the golf swing mainly focused on just one rigid segment, more recent studies also involved the consideration of two or three segments and of flexible club models. [JR(2002)] presented a mathematical, 3-D model of the golf swing. The model consisted of two segments, one of which represented the arms and the shoulder and the other one the club. The two segments were connected to each other by using a spherical joint. This joint allowed movement in all three rotational degrees of freedom and represented the wrist joint of the player. The arm/shoulder segment was connected to a joint whose coordinates were fixed in space and that allowed two kinds of rotation: about a neck axis, and rotation about an axis, connecting both shoulders. For his swing simulation, Jones split the downswing into two phases. In the first phase, the wrists were locked while the arm segment started to rotate. In the second and final phase of the downswing, the wrists were released, allowing a natural acceleration of the club towards the ball caused by centrifugal forces. To demonstrate the capabilities of the model, Jones presented examples for the effects of changing the club orientation at the beginning of the downswing or changing the position of the centre of gravity of the club. Even small variations of these parameters caused major changes in the position of the model segments at impact, jeopardizing the accuracy of the swing. This demonstrates how small changes in the mechanical characteristics of golf

equipment can have significant effects on the outcome of the swing unless the coordination of the motion is adapted to these changes by the golfer. Unfortunately, Jones provided no details on the joint torques driving the model and acting on the wrist joint, and gave no information regarding the validation of his model.

Full body models

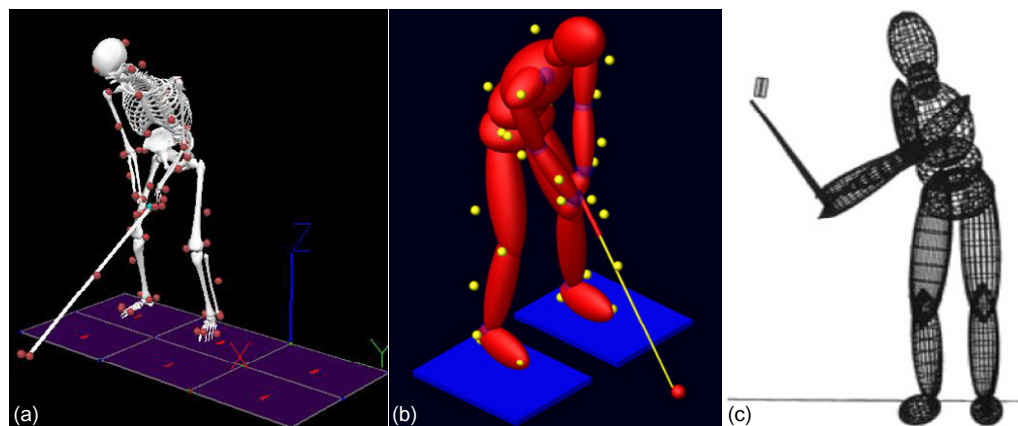


Figure 2.5 – Examples of full body swing models, (a)the model made by transformed markers position to body part position and orientation [Heldoorn and Vlasblom(2010)]; (b)eighteen-segment model [Betzler et al.(2008)Betzler, Shan, and Witte]; (c)fifteen-segment model [Nesbit(2005)].

An early full-body model of a golfer performing a downswing was presented by [S(1996)], who utilized the multibody dynamics software ADAMS. The body segment trajectories of McGuan's simulation were based upon data obtained from a golf swing. McGuan pointed out that there are two intrinsic problems when driving complex rigid body models with motion capture data obtained from real movements. In most cases the equations of motion of the model will be mathematically over-determined when the trajectories of multiple markers are constraining the system, and the motion capture markers will change their position relative to their corresponding body segments because of skin movement or instrumental errors. McGuan overcame these problems by introducing weightless spring elements, which connect each motion capture marker with the corresponding virtual marker on the rigid body model of the golfer, thereby allowing the rigid body movement to fit the recorded marker trajectories. He then used a two-step approach in order to allow a simulation of the movement. During the first step, the body segments were moved by the marker trajectories as described earlier, and angular kinematics were recorded at each joint. During the second step, the marker trajectories from motion capture were ignored and the model was set into motion by joint torques. McGuan demonstrated that this model could be used to show the effects of shaft

stiffness variations on club head velocity and dynamic loft angle at impact. It is interesting to note that the simulated swings were relatively inefficient in terms of club head speed and loft angle when the shaft stiffness was changed, unless the torque curves of the model were adapted.

More recently, [Nesbit(2005)] presented the results of another simulation study using a more complex model (figure 2.5.c), consequently applied this model for a work and power analysis of the swing [Nesbit and Serrano(2005)], and published a detailed description of the model [Nesbit(2007)]. His objective was to characterize the complete 3-D kinetics and kinematics of the golf swings of several subjects. After doing so, his aim was to highlight similarities and differences among golfers. He analyzed one swing of each of 85 subjects. All players used the same driver for their swings. The angular displacement histories of each joint were used to define the movement of a full body model of the golfer, which included sub models of a rigid android, a flexible club, an impact model, and a ground surface model. It was assumed that the load between both hands was distributed equally, all joints were either ideal ball and socket or hinge joints, and the model did not include any representation of muscles or tendons, so no strain energy could be stored. Validation was performed by comparing manually calculated joint torques, results from other studies, and ground reaction force data, and showed reasonable agreement. However, it was not possible to use the derived joint torque profiles to drive all the degrees of freedom of the model's joints in a forward dynamics way because this resulted in un- predictable results and simulation failure [Nesbit(2007)]. Nesbit's results support the idea that each golfer has a unique kinematic and kinetic swing 'signature'. The overall coordination was found to be a very important factor for maximizing club head velocities: the subjects did not use hindrance torques to block their wrists as proposed by earlier simulation studies; instead they coordinated the full-body motion in such a way as to delay wrist release and to achieve peak club velocity at impact. These findings highlight the value of including the full body motion of the player in golf simulation studies, as important information regarding body segment coordination might be missed if only 2-D data are considered. Using a similar approach, yet without performing a detailed analysis of muscle forces, swings performed by one golfer with four different club models have also been simulated [Betzler et al.(2008)Betzler, Shan, and Witte] (figure 2.5.b).

2.3 Mechanical properties of a golf shaft

This section focuses on the mechanical properties of the shaft. The purpose of this section is to put the subsequent sections of the literature review into context and to provide background

information. It is deemed necessary to fully understand the mechanical characteristics of the club in order to correctly interpret its dynamic behaviour.

2.3.1 Mass and density

As for the geometry of the golf shaft, published data describing typical mass properties of shafts is limited and, in most cases, anecdotal and not based on scientific study. [Lee and Kim(2006)] mentioned a number of categories of mass ranges, which are summarised in table 4.1. The overall mass range stated by Lee and Kim is similar to values presented by [Howell(1992)], who stated the minimum and maximum mass of composite shafts as 59g and 110g, respectively. [Penner(2003)] mentioned that the typical weight is 90g for a graphite shaft and 120g for steel shafts, which is within the range given by the other authors.

Table 2.1 – Mass ranges of golf shafts(adapted from [Lee and Kim(2006)]).

Mass	Category
< 60 g	light carbon shafts
60 - 80 g	general user carbon shafts
80-100 g	professional carbon shafts
> 100 g	steel shafts

The mass ranges presented by Lee and Kim indicated that there is a trend for weaker players to prefer lighter shafts, presumably to reduce the inertia of the club.

In terms of density, [Huntley et al.(2006)]Huntley, Davis, Strangwood, and Otto] found that it was consistent for the 33 shafts he sectioned ($1.5g/cm^3$). This is close to a value of $1.55g/cm^3$ identified in a material database as a typical density of carbon/epoxy composite material.

2.3.2 Golf club length

For an assembled golf club, rather than measuring the length of the shaft in isolation, it is common to use the overall club length as a measure. This is due to the fact that the effective club length can be different for two clubs even if they have identical shaft lengths, depending on the construction of their club heads. Therefore,[Maltby(1995)] defines club length as the distance from the cap of the grip to the intersection of the shaft centre line with the ground with the club sole resting on the ground. This definition is similar to the definition of club length in the Rules of Golf as displayed in figure 2.6. The Rules of Golf limit the club length for all clubs except putters to a maximum of 1.219 m. The only club of a typical set with a length

close to this limit is the driver. driver. The length of the other clubs decreases gradually as the loft angle of the clubs increases, with the possible exception of the putter.

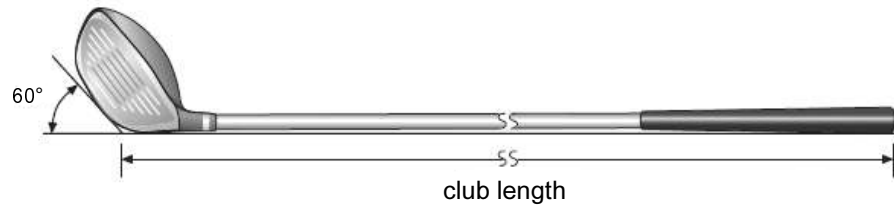


Figure 2.6 – Definition of club length (adapted from [Maltby(1995)]).

2.3.3 Swing robot

The construction of one of the first golf robots was triggered by the need for objective shaft tests. This led to the construction of a robot called the “Golf Club Testing Device”, but later the term “Iron Byron” emerged (figure 2.7.a). Other manufacturers of golf robots are Miyamae (Japan) and Golflabs (USA) (figure 2.7.b) and (figure 2.7.c), respectively). As illustrated by figure 2.7, the majority of current robot models are based on variations of the double pendulum model of the swing, which consists of two links. The arm link connects a stationary shoulder hub with the wrists. Attached to the artificial wrist is the club, thereby representing the second part of the double pendulum. The golf robots are controlled by compressed air (Iron Byron) or a servo-motor that drives the shoulder joint. The wrist is passive (e.g. Golflabs) or driven by additional motors (e.g. Miyamae 5). It is generally accepted that the swing motion of robots is much less complex than a human swing. However, it is common to validate the robot generated launch conditions against launch conditions recorded from human swings in order to ensure the validity of a robot test. The assumption is that, due to the short impact duration, the robot results are transferable to humans as long as the robot presents the club head to the ball in the same way a human player does (identical club head velocity and path).

Several researchers presented methods to determine torque patterns to control robots. The difficulty is that most robots are under-actuated because one motor controls two joints. This makes it a complex task to design a torque pattern to achieve the desired joint trajectories and impact conditions. One approach that has been presented in a series of papers by Ming and colleagues. It involves the use of a relatively simple mechanical model (ignoring shaft flexibility and friction) to determine a basic torque pattern. This is combined with an artificial neural network (ANN), which automatically adjusts the torque pattern over a number of learning cycles until the robot swings the club following the target trajectory. This approach has been successfully used to control a prototype robot by using a simple ANN [Ming and Kajitani(2003a)] and

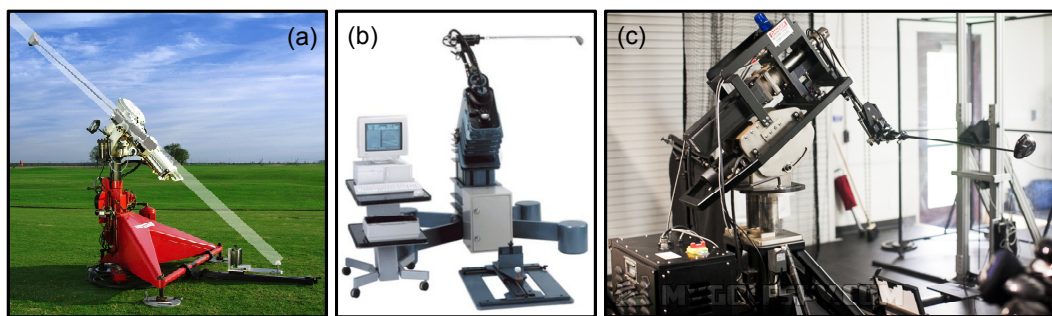


Figure 2.7 – Commercial golf robots (adapted from internet), (a)Iron Byron; (b)Miyamae 5; (c)Golflabs robot.

a recurrent ANN [Ming et al.(2006)Ming, Furukawa, Teshima, Shimojo, and Kajitani].

In summary, it appears that robot tests are a common tool to validate new club head designs, and the validity of results for club head tests can easily be confirmed by comparing the launch conditions produced by the robot to launch conditions achieved by human players. However, little work has been published to verify that the shaft loading profiles of humans and robots are comparable, with the work by [E(2006)] summarised above being the only exception. Therefore, it appears to be necessary to compare robotic and human shaft loading patterns before it is possible to use a robot as a valid tool to simulate human shaft loading.

2.4 Wearable sensors

Vision-based sensing provides a rich source of information but is not always accurate enough for certain kinematic features. This can be caused by instrument frame rate or image resolution. Thus far, typical uses of wearable sensors include general activity monitoring [Liu and J(2000)], medical studies [Awad and Jiang(2007)] and sport performance analysis [J Pansiotand R(2006)]. Two main classes of wearable sensors have been popular: physiological sensors and inertial sensors (motion, position and forces). Physiological sensors focus on measurements of human vital signs, such as blood pressure, internal body and skin temperatures, ECG, electroencephalography (EEG)and EMG. Such as indoor temperature and humidity, the unconditioned physiological signals are in the order of micro volts and always coupled with large common mode noise. This characteristic necessitates the proper analog signal conditioning circuit before the physiological signals are fed into the analog-digital converter. Moreover, the physiological signals are sensitive to the environment around the human body.

Inertial sensors (figure 2.8), such as accelerometers and gyroscopes, which measure accelera-

tion and rotation angular rate of the human body, can infer the subject's position, velocity, and orientation. However, most inertial sensors have several error sources, which are more difficult to deal with. Therefore, two challenges are proposed when inertial sensors are integrated into Microelectromechanical systems (MEMS): calibration and data filtering. Every inertial sensor is required to be calibrated after assembly in order to remove null bias error and scale factor error. Null bias error is the deviation from zero when the inertial sensor is experiencing no stimulus, and scale factor error is the deviation from ideal of the sensor's sensitivity. Orientation estimation and location tracking are more sensitive to those noise: if they are not treated properly, small errors in angular velocity readings will be integrated into progressively larger errors in orientations, and cause the rapid degrade of performance. The same situation will also occur when accelerations are integrated into positions. Therefore, data filtering is necessary once inertial sensors acquire the raw biokinetic parameters.

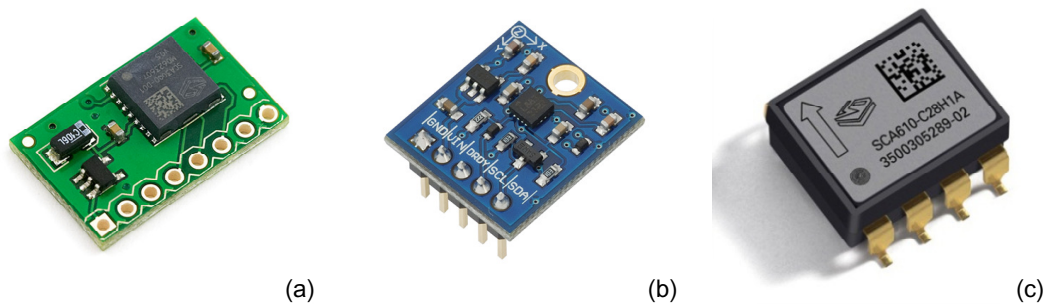


Figure 2.8 – Inertial sensors (adapted from internet), (a) accelerometer; (b) magnetic sensor; (c) gyroscopes.

2.4.1 Motion and position sensors

For motion sensors, MEMS based inertial sensors such as accelerometers and gyroscopes are widely used for human motion capture [Liu et al.(2009a)Liu, Inoue, and Shibata]. Such Inertial Measurement Units (IMU) allow a subject-centric description of the motion. In contrast to vision-sensors, motion capture from IMU is not dependent on external conditions such as the light or occluding objects. However, IMU lack absolute localisation in the environment. Commonly, accelerometers only measure the three dimensional (3D) acceleration in their own coordinate system, the orientation of which is often unknown.

Moreover, simply integrating twice the acceleration signal to evaluate the position of the sensor is often not practical as signal noise can cause considerable drift over time. Alternatively, an accelerometer can be used to measure the angle with respect to the vertical (sometimes

referred to as tilt or lean) when it is stationary. In this case, the only acceleration is enforced by the Earth's gravity.

Gyroscopes, on the other hand, measure angular velocities. They lack absolute angle measure and the derived signal must be integrated to provide an angular value. Therefore, just as with accelerometers, angles calculated from a gyroscope will be subject to drift over time.

Digital magnetic sensors provide an absolute angle with respect to the direction of the Earth's magnetic field but their output is susceptible to a wide range of noise generated by ferromagnetic objects and surrounding electric and electronic devices. Furthermore, the magnetic field intensity at the surface of the Earth is subject to local variations. Kalman filtering is often used to derive a more stable signal and a combined use of accelerometers, gyroscopes and magnetic sensors can also solve some the issues mentioned above.

2.4.2 Force and pressure sensors

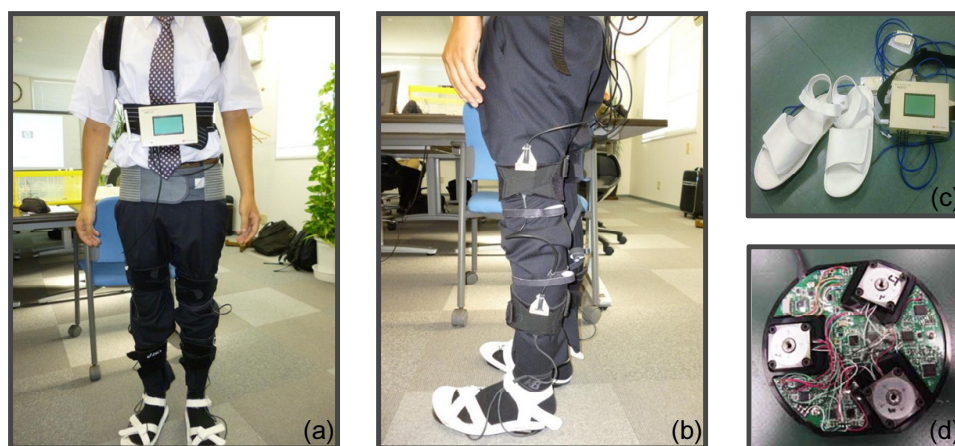


Figure 2.9 – M3D system (adapted from [Liu et al.(2009a)Liu, Inoue, and Shibata], (a)front view of system set up; (b)side view of system set up; (c)top view of system; (d)the wearable force plate.

Strain and bend sensors can also be placed on the user's joints to monitor their motion [King and Atallah(2009)]. They are typically based on materials whose electromagnetic properties (resistance or capacitance) change in response to stress. Optic fibre sensors are also popular for practical applications. These sensors are often fixed onto garments or woven into the textile, making them ubiquitous. Foot pressure sensors such as the force sensors and M3D system [Liu et al.(2009a)Liu, Inoue, and Shibata] have also been used extensively in gait analysis for both sport and healthcare (figure 2.9). They are typically based upon piezo-electric materials. They can provide detailed information about the GRF while the subject is perform-

ing an activity such as walking or running. The trajectory of the centre of pressure during a walking cycle provides valuable information on a runners stride.

2.5 Summary

As outlined in the introduction, the motivation for this work is an attempt to rectify the lack of scientific understanding of the interaction between player and shaft and its implications for golf performance. The following conclusions were drawn based on the literature review:

1. The relationship of body motion and shaft deflection appears to be least well understood, but it is likely to be the most important aspect when analysing the interaction between player and club.
2. One difficulty in understanding the relationship between wrist action and performance in golf play is that there are many different swing styles rather than one. Swing modeling and simulation has significantly improved our understanding of a number of factors influencing golf performance. There is little evidence supporting the conventional view that a delay in wrist release can increase impact velocity.
3. Robots could be used for repeatable, dynamic tests, but most applications focus on estimation of club shaft properties.
4. Advancements in microelectronics and wireless communication have enabled the design of light-weight wearable sensor devices. The advantages of wearable sensors are small size, increasing accuracy, low power consumption, and mobility to be usable. It would be desirable if future wearable sensors could provide feedback to golf players on the quality of the performed swing in real-time.

3 Dynamic Analysis for the Release Point of the Golf Swing

3.1 Introduction

The list of factors influencing the success of a golf swing is long. Very often it is not easy to understand the relationships of the various parameters and variables involved. This study is made in the belief that understanding of dynamics of the golf swing should help players to increase both the distance and the precision they achieve in their shot.

Most dynamics studies of golf swing have employed models of varying degrees of sophistication systems. Recently, three-dimensional (3D) models, which are much more realistic models of the golf swing, have been developed [Nesbit and Serrano(2005)]. Compare to 3D models, the double pendulum model of the golf swing was first analyzed by Williams [Williams(1967)] and Jorgensen [Jorgensen(1999)] which are used to gain insight into the basic mechanics involved in the golf swing and to explain the impact of various parameters on the golf swing.

From the "natural release point", when the wrist joint turns freely due to the centrifugal torque of the golf club, even though the input torque about the wrist joint is zero, to impact of the club with the ball, the acceleration patterns are generally divided into three patterns: angular acceleration gradually increased from the downswing start, angular acceleration gradually decreasing from the downswing start, and angular acceleration kept fixed during the whole downswing process. Over the years, golfers and researchers have asked the question: which kind of acceleration pattern can provide the optimum club head speed at impact? Based on the study of the stroboscopic photograph of Bobby Jones' swing, Williams [Williams(1967)] found that no additional wrist torque was necessary after the "natural release point", and the club freewheeled at the latter stage of the downswing. [Jorgensen(1999)] and [Cochran and Stobbs(1968)] believed that the passive wrist action (the so called "delay release") enhanced the club head speed

at impact. [Cochran and Stobbs(1968)] also considered that the club head speed at impact could be increased by the passive active wrist action with an appropriately "timed" wrist torque. Using a three segment model, [Sprigings and Neal(2000)] also confirmed that the passive active wrist action could provide an advantage in club head speed at impact. However, the golf ball position the point where impact occurs was assumed to be constant in these studies. [Pickering and Vickers(1999)] used the maximum criterion (the maximum criterion can determine the maximum horizontal club head speed at impact) to study the passive wrist action, yet the active and passive active wrist actions were not considered. It has been reported that the shaft positions of many professional golfers are always maintained vertical at impact when viewed "face on" [Sprigings and Mackenzie(2002)]. The impact criterion (vertical club shaft at impact) was therefore applied to examine the role of the wrist action in this paper. The acceleration pattern was investigated by the transient response analysis, and the computational results between golf club and wrist were compared. As far as the authors are aware, the way the wrist action alters the club head speed at impact has not been thoroughly investigated, although some researchers did include this point in their work. [Jorgensen(1999)] attributed the role of the passive wrist action to the change of a mysterious "timing" term, yet an explicit explanation was not presented. [Sprigings and Mackenzie(2002)] used a three-segment model comprising the torso, arm and golf club to identify the mechanical sources of power that are responsible for the increase in club head speed. The ball position, however, remained constant in their simulation model and thus the influence of ball position on the energy transfer between the arm and golf club at impact was neglected. In addition, little attempt has been made by earlier researchers to identify the patterns of acceleration that produce the energy flow through the chain link system.

The primary purpose of this chapter was to re-examine the release phenomenon in the golf swing using a double pendulum model that incorporated the properties of simplified release condition into the simulation.

3.2 The Double Pendulum Model

As shown in Figure 3.1, it was assumed that the swing took place in a plane tilted at an angle φ to the vertical direction. The assumption of the planar movement of the downswing is well supported in the work of [Cochran and Stobbs(1968)] and [Jorgensen(1999)].

The mathematical model of the golf downswing was deemed to be a two dimensional double pendulum. This model consists of a rigid arm link, which is constrained to rotate about a fixed

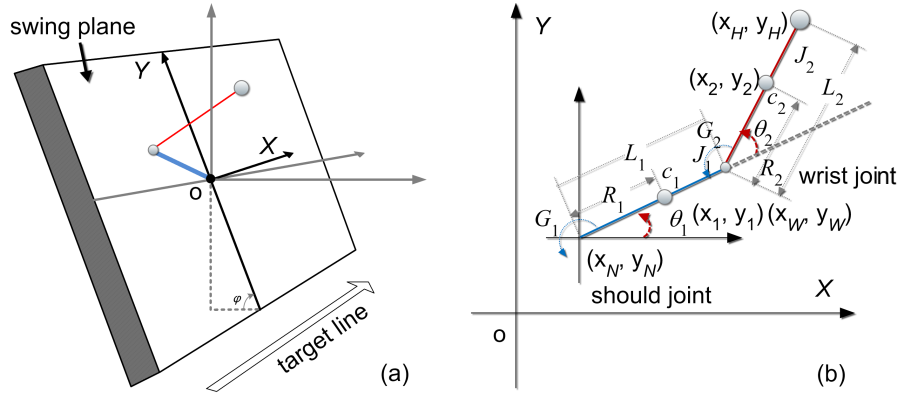


Figure 3.1 – Double pendulum model of golf downswing. (a) plane of swing motion; (b) coordinate system of golf swing. c_1 , c_2 are the centres of the mass of arm and club, respectively.

horizontal axis at the point $N (x_N, y_N)$. And a rigid club link, which is connected to the arm link at the point $W (x_W, y_W)$, with a joint representing the wrists of the golfer. Both links have distributed mass, indicated by m_1 at a distance R_1 from N for the arm and m_2 at a distance R_2 from W for the club. The position of arm link is determined by the angle θ_1 measured counterclockwise from the horizontal, and the position of club link is determined by the angle θ_2 measured counterclockwise from the extension line of the arm link.

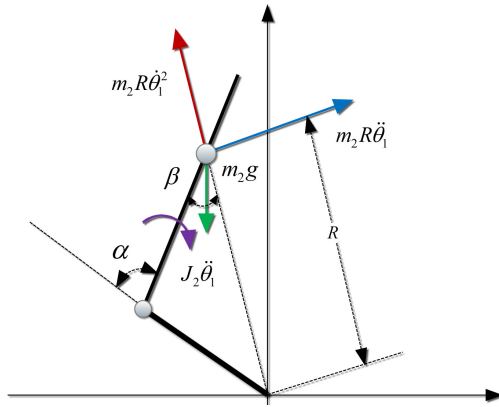


Figure 3.2 – Combination of moments

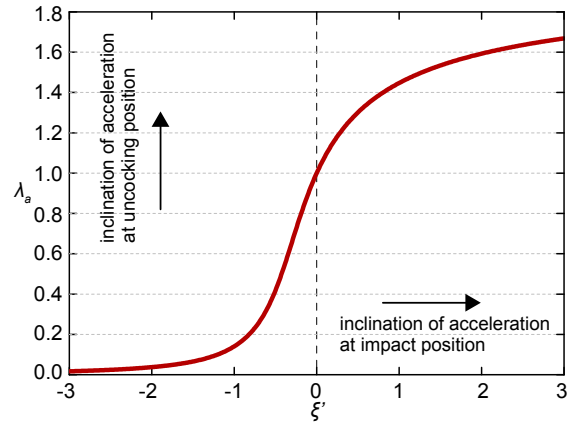


Figure 3.3 – Relationship between acceleration inclination.

The downswing was separated into two phases. In phase 1, the two rigid bodies rotate as one body with a constant wrist-cock angle. In phase 2, the various types of wrist actions were employed. The following notation was applied:

G_1, G_2 : Torque on arm and club, respectively.

m_1, m_2 : Mass of arm and club, respectively.

Chapter 3. Dynamic Analysis for the Release Point of the Golf Swing

L_1, L_2 : Length of arm and club, respectively.

R_1, R_2 : Length from shoulder joint to N and from wrist joint to M , respectively.

J_1 : Moment of inertia of arm about shoulder joint.

J_2 : Moment of inertia of club about M .

θ_1, θ_2 : Angle of arm and club, respectively.

ϕ : Inclination of plane of downswing.

g : Gravitational acceleration.

Table 3.1 – Parameters of swing model.

Parameter	Value
m_1	7.312 kg
m_2	0.394 kg
a_1	0.615 m
a_2	1.105 m
L_1	0.326 m
L_2	0.753 m
J_1	1.150 kg · m ²
J_2	0.077 kg · m ²
ϕ	60°
g	9.81 m/s ²

The values of arm and club parameters used in the calculation were those given by [Lampsa(1975)], as shown in table 3.1, together with club data which was considered to be appropriate for a driver.

The differential equations of swing motion were derived using the *Lagrangian* method. The potential energy is function of θ_1 and θ_2 . The kinetic energy of the system is a function of θ_1 and θ_2 and their time derivatives $\dot{\theta}_1$ and $\dot{\theta}_2$. When *Lagrange* equations are used with these functions, the detailed differential equations in two phases are obtains as follows: In phase 1, the angle between arms and golf club is constant, where, $\theta_2 = -\alpha$, as shown in Figure 3.2:

$$\begin{aligned}
 Q_1 = & \{J_1 + J_2 + (R_2^2 + L_1^2)m_2 + R_1^2m_1 + 2L_1R_2m_2 \cos \alpha\} \ddot{\theta}_1 \\
 & + (g_\phi + \ddot{y}_N) \{R_2m_2 \cos(\alpha - \theta_1) + (L_1m_2 + R_1m_1) \cos \theta_1\} \\
 & - \{(L_1m_2 + R_1m_1) \sin \theta + R_2m_2 \sin(\theta - \alpha)\} \ddot{x}_c
 \end{aligned} \tag{3.1}$$

In phase 2:

$$\begin{aligned}
 Q_1 = & (g_\phi + \ddot{y}_N)(L_1 m_2 \cos \theta_1 + R_1 m_1 \cos \theta_1 + R_2 m_2 \cos(\theta_1 + \theta_2)) \\
 & - 2L_1 R_2 m_2 \dot{\theta}_1 \dot{\theta}_2 \sin \theta_2 - L_1 m_2 R_2 \dot{\theta}_2^2 \sin \theta_2 + (J_1 + J_2 + L_1^2 m_2 \\
 & + R_1^2 m_1 + R_2^2 m_2 + 2L_1 R_2 m_2 \cos \theta_2) \ddot{\theta}_1 + (J_2 + R_2^2 m_2 \\
 & + L_1 R_2 m_2 \cos \theta_2) \ddot{\theta}_2 - \ddot{x}_N \{L_1 m_2 \sin \theta_1 + R_1 m_1 \sin \theta_1 + R_2 m_2 \sin(\theta_1 + \theta_2)\} \quad (3.2)
 \end{aligned}$$

$$\begin{aligned}
 Q_2 = & (g_\phi + \ddot{y}_N) R_2 m_2 \cos(\theta_1 + \theta_2) + L_1 R_2 m_2 \dot{\theta}_1^2 \sin \theta_2 + (J_2 + R_2^2 m_2 \\
 & + L_1 R_2 m_2 \cos \theta_2) \ddot{\theta}_1 + (J_2 + R_2^2 m_2) \ddot{\theta}_2 - \ddot{x}_N R_2 m_2 \sin(\theta_1 + \theta_2)
 \end{aligned}$$

where, $g_\phi = g \cdot \cos \phi$ represents the component of gravitational acceleration in swing plane ϕ . Q_1 and Q_2 are torques exerted on arms and wrists, respectively.

3.2.1 Conditions of release

Prior to impact, wrist are kept cocked; meaning, the club link is maintained a constant angle with the arm link. Then release the club by allowing the wrist to uncock. Equation 3.2 is a second order differential equation. It can only be solved numerically. It will solved for the part of the swing where the wrists are uncocked, and subject to the following initial conditions at the release point, given as: $\theta_2 = -\alpha$, $\dot{\theta}_2 = \ddot{\theta}_2 = 0$, and $Q_2 = Q_{2W}$. Substitute initial conditions into equation 3.2, the uncocking condition equation is as follows:

$$\begin{aligned}
 Q_{2W} = & M_{OW} + M_{CW} + M_{gW} + M_{xW} + M_{yW} \\
 & - L_1 R_2 m_2 \dot{\theta}_{1W}^2 \sin \alpha + (R_2^2 m_2 + L_1 R_2 m_2 \cos \alpha) \ddot{\theta}_{1W} + J_2 \ddot{\theta}_{1W} \quad (3.3) \\
 & + g_\phi R_2 m_2 \cos(\theta_{1W} - \alpha) + \ddot{y}_{NW} R_2 m_2 \cos(\theta_{1W} - \alpha) - \ddot{x}_{NW} R_2 m_2 \sin(\theta_{1W} - \alpha)
 \end{aligned}$$

As show in figure 3.2, mainly forces applied moment to the wrist joint. Among which, angular acceleration causes a tangential inertial force (plotted with the blue arrow), an inertial moment (plotted with the purple arrow) applied negative moment M_{CW} to the wrist joint, and angular velocity causes a centrifugal force (plotted with the red arrow) applied positive moment M_{OW} . The green arrow represents the gravity force component M_{gW} in plane ϕ . M_{xW} and M_{yW} are moments produced by accelerations along with x and Y -axis, respectively.

Although the golfer swings the club in the earth's gravitational field, the effect of this field on the motion of a vigorously swung club was expected to be negligible. This point was investigated starting with the study of stroboscopic photographs of golf swings, and for a full swing of driver

Chapter 3. Dynamic Analysis for the Release Point of the Golf Swing

the average gravitational torque was estimated to be about 6% of the torque supplied by the golfer, and the average deviation from this value estimated to be about 2% [Jorgensen(1999)]. Assuming that the effect of gravity on swing motion is negligible, simplified equation of release condition becomes:

$$Q_{2W} = M_{OW} + M_{CW} = -L_1 R_2 m_2 \dot{\theta}_{1W}^2 \sin \alpha + \{J_2 + R_2^2 m_2 + L_1 R_2 m_2 \cos \alpha\} \ddot{\theta}_{1W} \quad (3.4)$$

Thus, we have:

$$\dot{\theta}_{1W}^2 = \frac{R_2 \{1 + J_2 / (m_2 R_2^2)\} + L_1 \cos \alpha}{L_1 \sin \alpha} \ddot{\theta}_{1W} - \frac{Q_{2W}}{m_2 R_2 L_1 \sin \alpha} \quad (3.5)$$

The length of golf club R_{2E} is expressed by:

$$R_{2E} = R_2 \{1 + J_2 / (m_2 R_2^2)\} = \frac{m_2 R_2^2 + J_2}{m_2 R_2} \quad (3.6)$$

The ratio of club length R_{2E} to L_2 is defined as $\eta_{R2E} = R_{2E} / L_2$, the length ratio of arm link to club link is defined as $\gamma = L_2 / L_1$. The ratio of torque Q_{2W} to torque Q'_{1W} is defined as $\tau = Q_{2W} / Q'_{1W}$ at release point. Then, defined ϕ and ε as:

$$\phi = \frac{\eta_{R2E} \gamma + \cos \alpha}{\sin \alpha}$$

$$\varepsilon = \frac{\tau J_0}{\phi m_2 R_2 L_1 \sin \alpha}$$

Rewrite equation 3.5 as:

$$\dot{\theta}_{1W}^2 = (1 - \varepsilon) \phi \ddot{\theta}_{1W} = \lambda \phi \ddot{\theta}_{1W} \quad (3.7)$$

In the condition that wrist is released with combination of moments located on wrist, the swing system changes from one pendulum model to double pendulum model. Direction of M changes from anticlockwise to clockwise. Therefore, at the release point, assuming that torque $Q_{2W} = 0$, then $\lambda = 1$, rewrite equation 3.7 as:

$$\dot{\theta}_{1W}^2 = \phi \ddot{\theta}_{1W} \quad (3.8)$$

where, θ_{1W} is angular between arms and horizontal direction at release point, $\dot{\theta}_{1W}$, $\ddot{\theta}_{1W}$, are angular velocity and angular acceleration respectively at release point. ϕ is determined by the length of player's arm, θ_2 , and properties of golf club. In this research, assume that ϕ is

constant. Take differentiation of both sides of equation 3.2:

$$\begin{aligned} Q'_1 &= \{J_1 + J_2 + (R_2^2 + L_1^2)m_2 + R_1^2 m_1 + 2L_1 R_2 m_2 \cos \alpha\} \ddot{\theta}_1 \\ &= Q_1 - g_\phi \{R_2 m_2 \cos(\theta_1 - \alpha) + (L_1 m_2 + R_1 m_1) \cos \theta_1\} \end{aligned} \quad (3.9)$$

According to equation 3.9, $\ddot{\theta}_1$ can be expressed as:

$$\ddot{\theta}_1 = \frac{Q'_1}{m_1 R_1^2 + m_2 \{L_1^2 + R_2^2 + 2L_1 R_2 \cos \alpha\} + J_1 + J_2} = \frac{Q'_1}{J_0} \quad (3.10)$$

where, J_0 is inertia moment produced in swing phase 1. Assume that rotation center is fixed, note that $J_2 = m_2 R_J^2$, $r_J = R_J / R_2$. To a further step, according to Equation (3.8), ratio of angular acceleration $\ddot{\theta}_{1W}$ at release point to average angular acceleration α_0 can be described as Figure 3.3. In order to resolve motion equations containing angular velocity $\dot{\theta}_1$ and angular acceleration $\ddot{\theta}_1$, assuming that shoulder joint is fixed, Q'_1 is the torque including gravity influence. At the release point, if $Q'_1 = Q_0$ is, the angular acceleration will be determined according to equation 3.10:

$$\ddot{\theta}_{1W} = \frac{Q_0}{J_0} = a \quad (3.11)$$

Define initial conditions, t_W is the period from top position to release point, $\theta_1 = \theta_{10}$, $\dot{\theta}_{10} = 0$, Angular velocity $\dot{\theta}_{1W}$ and angular θ_{1W} can be written as:

$$\dot{\theta}_{1W} = at_W \quad (3.12)$$

$$\theta_{1W} = at_W^2 / 2 + \theta_{10}$$

Substitute equation 3.12 into the release condition:

$$(at_W)^2 = \lambda \phi a \quad (3.13)$$

Resolve t_W according to equation 3.13:

$$t_W = \sqrt{\lambda \phi / a} = \sqrt{\lambda \phi J_0 / Q_0} \quad (3.14)$$

where, $\lambda \phi$ is the function of α , substitute equation 3.14 into equation 3.12:

$$\dot{\theta}_{1W} = at_W = \sqrt{\lambda \phi a} = \sqrt{\lambda \phi Q_0 / J_0} \quad (3.15)$$

Chapter 3. Dynamic Analysis for the Release Point of the Golf Swing

substitude equation 3.15 into equation 3.13, the angular displacement δ from top position to starting point of release is described as:

$$\delta = \theta_{1W} - \theta_{10} = \frac{1}{2} a t_W^2 = \frac{\lambda \phi}{2} \quad (3.16)$$

The energy T delivered to release point is written in the form of:

$$T = Q_0 \delta = Q_0 \lambda \phi / 2 \quad (3.17)$$

When release begin, angular θ_2 is decreasing. In the condition that link 1 parallels to link 2, $\theta = 0$. At the meantime, inertia moment about rotation joint is defined as J_R , energy T , torque θ_{1R} , club head speed V_{HR} is:

$$T = J_0 \dot{\theta}_{1W}^2 / 2 = J_R \dot{\theta}_{1R}^2 / 2 \quad (3.18)$$

$$\dot{\theta}_{1R} = \sqrt{\frac{J_0}{J_R}} \dot{\theta}_{1W} = \sqrt{2T/J_R} = \sqrt{Q_0 \lambda \phi / J_R}$$

$$V_{HR} = (L_1 + L_2) \dot{\theta}_{1R} = (1 + \gamma) L_1 \sqrt{2T/J_R} = (1 + \gamma) L_1 \sqrt{Q_0 \lambda \phi / J_R} \quad (3.19)$$

3.2.2 Effect of parameters of golf club

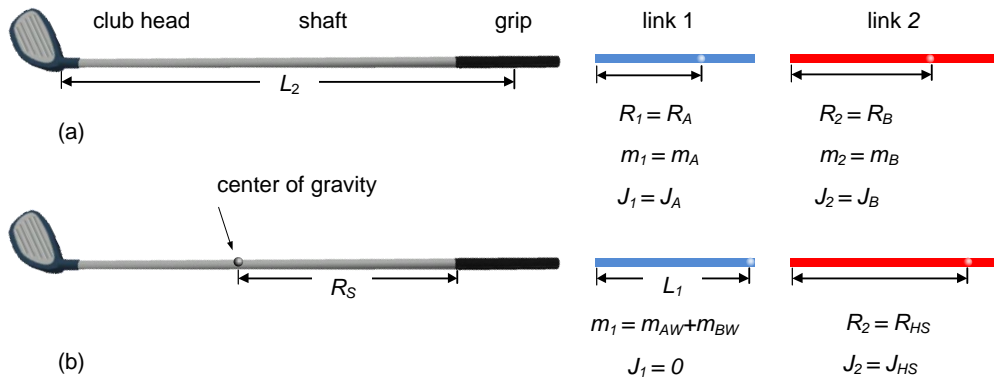


Figure 3.4 – A golf club model. (a) conventional mathematical model for 2-link system; (b) proposed golf club model for 2-link system.

Golf clubs are the tools used to strike the golf ball. A traditional golf club has three components: the head, the shaft and the grip, as show in figure 3.4. The rules of golf constrain golf club designs, but the goal of club makers is to create golf clubs, within those constraints that

maximize the physics behind a golfer's swing while allowing for some range of swing error to provide an accurate, long, and forgiving shot. Based on traditional model of the club (figure 3.4.a), regardless of inertia moments of grip and club head, there are 6 parameters, mass of club head m_H , mass of shaft m_S , lengthen from wrists to gravity center of shaft R_S , inertia moment of the shaft J_S , mass of grip $m_B W$, and the lengthen of club L_2 . Among these parameters mentioned above, m_S , R_S , and J_S are related to shaft. Assuming that cross-section area of the grip and the shaft are the same, m_S , R_S , and J_S are interact. More specifically, $\eta_{RS} = R_S/L_2$ and $\eta_{JS} = J_S/L_2^2$ are changed with variation of m_S . For example, with the same dimension of shaft, $\eta_{RS} = 1/2$, $\mu_{JS} = 1/12$, parameters of the club become to m_H , m_S , $m_B W$, L_2 . On the conditions that the mass of wrists is m_A , lengthen from gravity center to rotation center R_A , inertia moment of gravity center J_A , and the lengthen of link 1 L_1 , a more real golf club model is established, as shown in figure 3.4.(b).

Since the beginning of golf, the golf club has been modified to improve performance. Any serious discussion of golf swing requires an understanding of the properties of the club. These dynamic parameters determine how the club swings in the hands of the player. One of these dynamic parameters is the total mass m_2 of the club, which is proportional to club's weight. Another is the moment J_{A0} about the wrist-cock axis. The torque tending to pull club head downward is proportional to J_A . The third is the moment of inertia J_B about the same axis. The torque in wagging the club at a certain rate is proportional to J_B . The fourth dynamic parameter is the position of center of gravity R_2 , which determines the distribution of mass in the club about an axis. The inertia moment J_{A0} is written as:

$$J_{A0} = J_A + m_A R_A^2 \quad (3.20)$$

where, m_A is the mass of wrists, R_A is lengthen between end of the club and gravity center R_A , J_A is inertia moment about wrist gravity axis. Equivalent mass of wrists m_{AW} :

$$m_{AW} = J_{A0}/L_1^2 \quad (3.21)$$

Until now, the independent and dependent variables of golf club are all identify. To eliminate concentration units from this system, replace the original variables with rescaled values: equivalent mass of wrists m_{AW} , as defined in equation 3.21, it is the normalization of parameters related to the mass and the lengthen. Replace the mass of club head m_H and the mass of grip m_{BW} with parameters μ_H and μ_{BW} , respectively, where $m_H = \mu_H m_{AW}$, $m_{BW} = \mu_{BW} m_{AW}$. Replace m_S with the ratio μ_S of m_S to m_H , where $m_S = \mu_S \mu_H m_{AW}$. Gravity center of shaft $R_S = \eta_S L_2$. Inertia moment of shaft is defined as $J_S = \mu_{JS} m_S L_2^2 = \mu_{JS} \mu_S \mu_H m_{AW} L_2^2$. Rewrite

Chapter 3. Dynamic Analysis for the Release Point of the Golf Swing

expression of m_{1W} , with respect of L_1 :

$$m_{1W} = m_{AW} + m_{BW} = m_{AW}(1 + \mu_{BW}) \quad (3.22)$$

About link 2, mass of m_2 is the residual club mass, which is to remove m_{BW} :

$$m_2 = m_{HS} = m_H + m_S = m_H(1 + \mu_S) = \mu_H m_{AW}(1 + \mu_S) \quad (3.23)$$

with the same consideration, R_2 is defined as:

$$R_2 = R_{HS} = \frac{m_S R_S + m_H L_2}{m_S + m_H} = L_2 \frac{\mu_S \eta_S + 1}{\mu_S + 1} = L_2 \eta_{R2} = L_2 f_{R2}(\mu_S, \eta_S) \quad (3.24)$$

Then, combine the mass m_{BW} with link 1, in which $m_S = \mu_S \mu_H m_{AW}$. The inertia moment J_2 is defined as:

$$\begin{aligned} J_2 &= J_{HS} = m_S (R_2 - R_S)^2 + m_H (L_2 - R_2)^2 + J_S \\ &= \mu_H m_{AW} L_2^2 \left\{ \mu_S \left(\frac{\mu_S \eta_S + 1}{\mu_S + 1} - \eta_S \right)^2 + \left(1 - \frac{\mu_S \eta_S + 1}{\mu_S + 1} \right)^2 + \mu_{JS} \mu_S \right\} \\ &= \mu_H m_{AW} L_2^2 f_{J2}(\mu_S, \mu_{JS}, \eta_S) \end{aligned} \quad (3.25)$$

Defined R_{2E} with parameters mass m_2 , lengthen R_2 , and inertia moment J_2 :

$$R_{2E} = \frac{m_2 R_2^2 + J_2}{m_2 R_2} = R_2 \{1 + J_2 / (m_2 R_2^2)\} = L_2 \eta_{R2E} = L_2 f_{R2E}(\mu_S, \mu_{JS}, \eta_S) \quad (3.26)$$

After nondimensionalization, R_{2E} is expressed by L_2 and parameters related to the shaft. Note that, $\eta_{R2E} = R_{2E} / L_2$ is the function $f_{R2E}(\mu_S, \mu_{JS}, \eta_S)$ with respect to the shaft. Based on assumption that gradient of club cross-section is certain, parameters η_S and μ_{JS} are deemed to be constant values, $\mu_{R2E} = f_{R2E}(\mu_S)$. Function $f_{R2E}(\mu_S, \mu_{JS}, \eta_S)$ is only related with α and γ .

$$\phi = \frac{\eta_{R2E} \gamma + \cos \alpha}{\sin \alpha} = \frac{f_{R2E}(\mu_S, \mu_{JS}, \eta_S) \gamma + \cos \alpha}{\sin \alpha} \quad (3.27)$$

Equation 3.27 describes the effect of shaft related parameters on ϕ . Because parameters of club shaft, η_S and μ_{JS} assumed to be certain. Therefore, the left parameter μ_S is becoming critical to the ϕ .

About inertia moment J_0 , define parameter $\rho_W = J_0/(m_{AW}L_1^2)$, more specifically:

$$\begin{aligned}\rho_W &= \frac{J_{10} + J_2 + (R_2^2 + L_1^2)m_2 + 2L_1R_2m_2\cos\alpha}{m_{AW}L_1^2} \\ &= (1 + \mu_{BW}) + \mu_H\gamma^2 f_{J2}(\mu_S, \mu_{JS}, \eta_S) + (\gamma^2 f_{R2}(\mu_S, \eta_S)^2 \\ &\quad + 1)\mu_H + 2\gamma f_{R2}(\mu_S, \eta_S)\mu_H\cos\alpha \\ &= f_{\rho0}(\mu_H, \mu_W, \mu_S, \mu_{JS}, \eta_S, \gamma, \alpha)\end{aligned}\quad (3.28)$$

where, inertia moment ρ_W is the function about mass distribution of club with respect to μ_H , μ_W , μ_{JS} , η_S , γ , and α . With the equation 3.28, the interaction of above parameters are obvious.

3.3 Results

3.3.1 Conditions of release

The criterion of maximum horizontal club head speed at impact was used to investigate the effects of different kinds of acceleration patterns on the golf downswing. The following equation indicates the maximum criterion.

$$-L_1(\sin\theta_1\ddot{\theta}_1 + \cos\theta_1\dot{\theta}_1^2) - L_2[\sin(\theta_1 + \theta_2)(\ddot{\theta}_1 + \ddot{\theta}_2) + \cos(\theta_1 + \theta_2)(\dot{\theta}_1 + \dot{\theta}_2)^2] = 0 \quad (3.29)$$

Equation (3.29) was obtained by differentiating the equation of the horizontal club head speed v_b , with respect to time, and then equated to zero.

$$v_b = -L_1\sin\theta\dot{\theta}_1 - L_2\sin(\theta_1 + \theta_2)(\dot{\theta}_1 + \dot{\theta}_2) \quad (3.30)$$

Drive the simulation model, to obtain the swing motions of the arm and club at impact, including $\theta_1(t_{imp})$, $\theta_2(t_{imp})$, $\dot{\theta}_1(t_{imp})$, $\dot{\theta}_2(t_{imp})$, by the maximum criterion, the root of Equation (3.29) at the time of impact, t_{imp} was solved which was used to applied to achieve the angles and angular velocities of the arm and club at impact. After obtaining the swing motion of the arm and club at impact, the maximum horizontal club head speed v_m was determined from Equation (3.31).

$$v_m = -L_1\sin[\theta_1(t_{imp})]\dot{\theta}_1(t_{imp}) - L_2\sin[\theta_1(t_{imp}) + \theta_2(t_{imp})][\dot{\theta}_1(t_{imp}) + \dot{\theta}_2(t_{imp})] \quad (3.31)$$

The different acceleration patterns including constant, increasing, and decreasing during downswing as shown in Figure 3.5 were studied using the maximum criterion. Six positive

Chapter 3. Dynamic Analysis for the Release Point of the Golf Swing

constant wrist torques were employed: 5 *Nm*; 10 *Nm*; 15 *Nm*; 20 *Nm*; 25 *Nm* and 30 *Nm*. Here, the maximum wrist torque 30 *Nm* was given by [RJ and BD.(1981)], who measured this from a low handicap amateur golfer, using inverse dynamics.

For the decreasing acceleration pattern, the arm release angle, θ_1^r , given by Equation (3.32), which denotes when the wrist joint can be opened, was delayed in every degree of freedom from the natural release point until the point at which the set negative wrist torque was reached. The absolute value of the regulated negative wrist torque is the same as that of the positive wrist torque but with the opposite sign.

$$\theta_1^r = \theta + p1, \dots, p1 = 1^\circ, 2^\circ, \dots, \theta_1^p \quad (3.32)$$

θ is the integer part of θ_1^n , where θ_1^n is the arm rotational angle when the natural release point is reached and θ_1^p is the arm rotational angle when the regulated negative wrist torque is reached.

For the increasing acceleration pattern, the onset and end of the positive wrist torque were determined when the arm rotational angle satisfied Equation 3.33, respectively.

$$\theta_1^\circ = \theta + p2, \dots, p2 = 1^\circ, 2^\circ, \dots, \theta_1^\circ(t_{imp}) - 1^\circ \quad (3.33)$$

$$\theta_1^t = \theta_1^\circ + p3, \dots, p3 = 1^\circ, 2^\circ, \dots, \theta_1^\circ(t_{imp})$$

where θ is the integer part of θ_1^n . θ_1^n and θ_1^t are the arm rotational angles when the positive wrist torque is activated and deactivated respectively. $\theta_1^\circ(t_{imp})$ is the arm rotational angle when impact occurs.

For the constant acceleration pattern. The application of the negative wrist torque was the same as that in the decreasing acceleration, in which the negative torque kept the wrist cock angle constant until the desired arm release angle θ_1^r was reached. The onset and termination of the positive wrist torque, following the passive wrist action, were given by equations 3.34.

$$\theta_1^{\circ 1} = \theta_1^r + p4, \dots, p4 = 0^\circ, 1^\circ, \dots, \theta_1^\circ(t_{imp}) - 1^\circ \quad (3.34)$$

$$\theta_1^{t1} = \theta_1^\circ(t_{imp})$$

where $\theta_1^{\circ 1}$ and θ_1^{t1} are the arm rotational angles as the positive wrist torque is activated and deactivated respectively and $\theta_1^\circ(t_{imp})$ is the arm rotational angle when impact occurs.

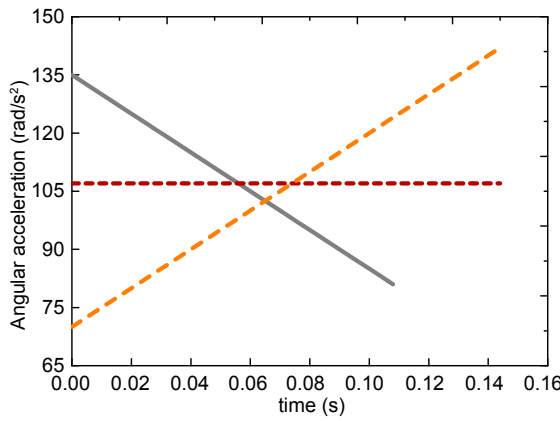


Figure 3.5 – Three different acceleration patterns(constant, increasing, and decreasing) during downswing.

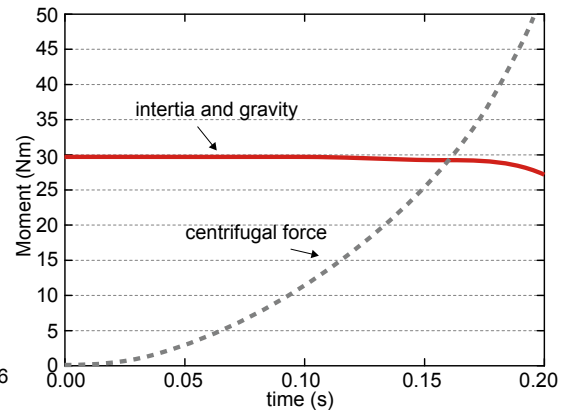


Figure 3.6 – Relationship between time and acceleration pattern during downswing, acceleration is constant.

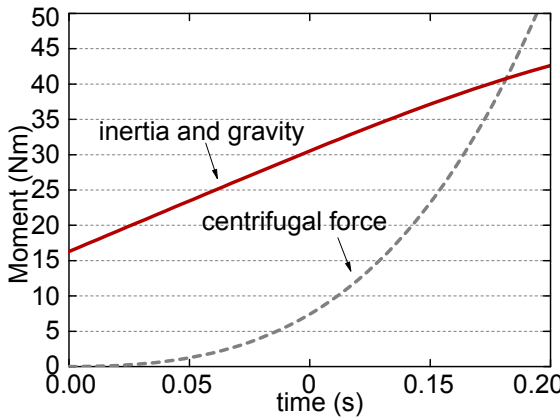


Figure 3.7 – Relationship between time and acceleration pattern during downswing, acceleration is increasing.

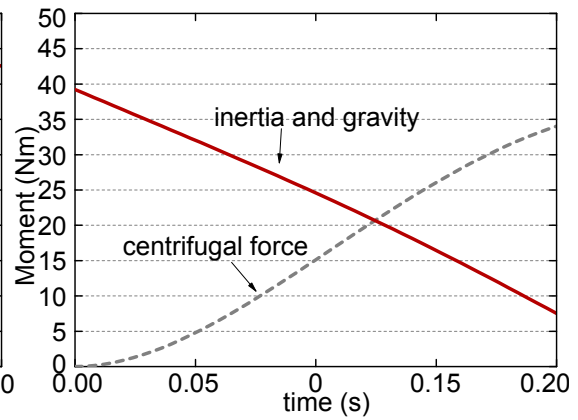


Figure 3.8 – Relationship between time and acceleration pattern during downswing, acceleration is decreasing.

The natural release wrist action, where no wrist torque is employed after the natural release point, was also studied for the purpose of comparison with the three wrist actions as mentioned above. Concerning the club shaft position at impact, both observations made by Mclean, an acclaimed professional golf instructor, and many swing photographs of professional golfers, clearly indicate that the shaft is held vertical at impact when viewed face-on. Thus, in the second simulation adopted the impact criterion vertical club shaft at impact to investigate the role of the wrist action. The impact criterion was given by Equation 3.35.

$$\theta_1(t_{imp}) + \theta_2(t_{imp}) - 270^\circ = 0 \quad (3.35)$$

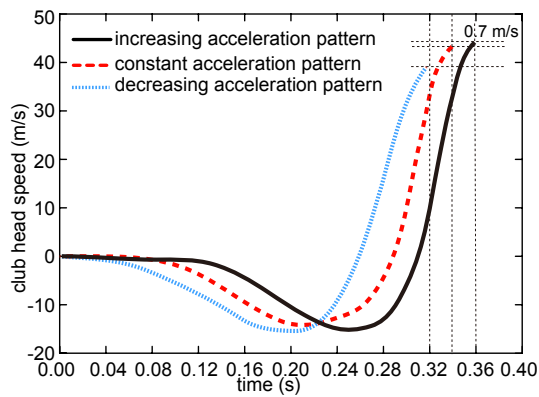


Figure 3.9 – Components of muscle power and joint-force power acting at the proximal end of the club segment.

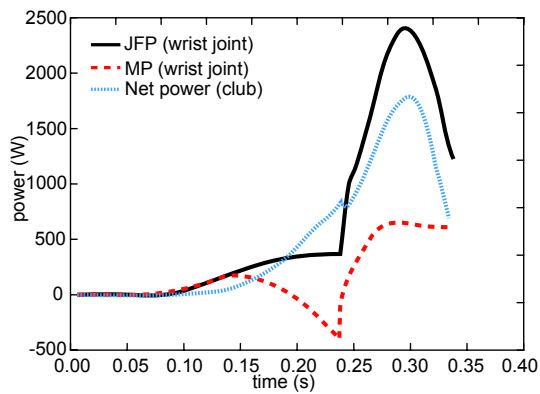


Figure 3.10 – Components of energy for the club segment as determined by integrating the respective power

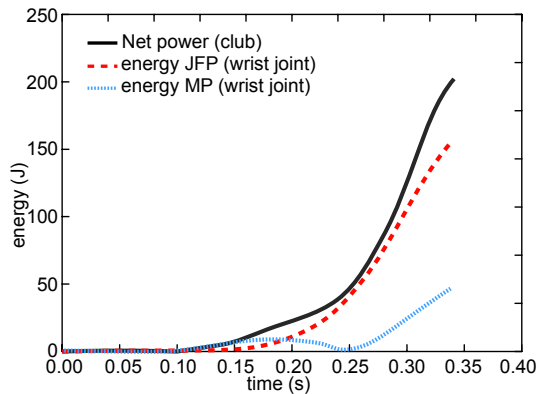


Figure 3.11 – Components of energy for the club segment as determined by integrating the respective power.

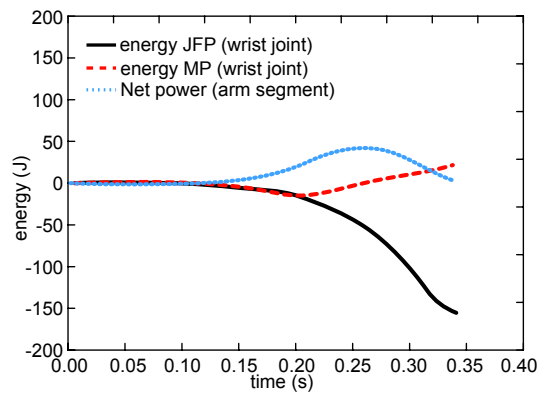


Figure 3.12 – Components of energy for the arm segment as determined by integrating the respective power.

Solved function to obtain the impact time. Then the club head speed at impact could be determined using the same method as that in the maximum criterion. It has been noted that there are many different types of torque functions of the shoulder joint that have been applied in previous studies: [Jorgensen(1999)] considered that the shoulder input torque was constant during the downswing.

The impact position constraint is consistent with the observation made by internationally acclaimed professional golf instructor, that the greatest drivers of the modern era when viewed face on, had his club shaft vertical at impact. The simulation sequence was terminated when the club head reached a position 0.2 m horizontally past the proximal end of the torso segment. This termination point corresponds to striking a ball positioned off the inside of the left heel.

Although a maximum time step of 0.002 s was used during the simulation runs, the exact time of impact was determined by means of interpolation.

As mentioned previously, the required torque at the wrist joint to maintain the wrist cock angle during the early phase of the downswing was computed dynamically. The energy flow through the three segments was computed by first calculating, and then integrating with respect to time, the two power sources at both the proximal and distal ends of the segments.

3.3.2 Effect of parameters of golf club

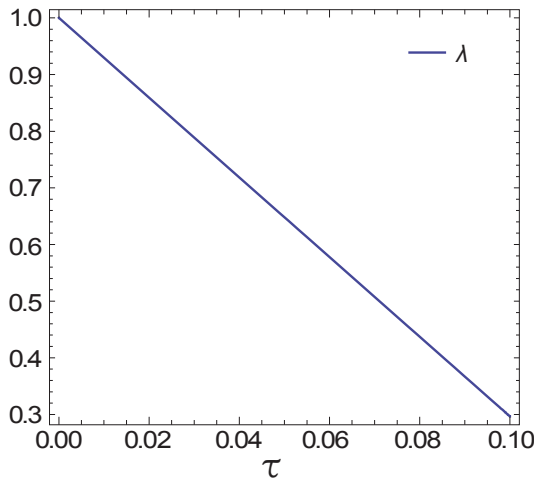


Figure 3.13 – Effect of the active wrist torque τ on the normalized parameter λ .

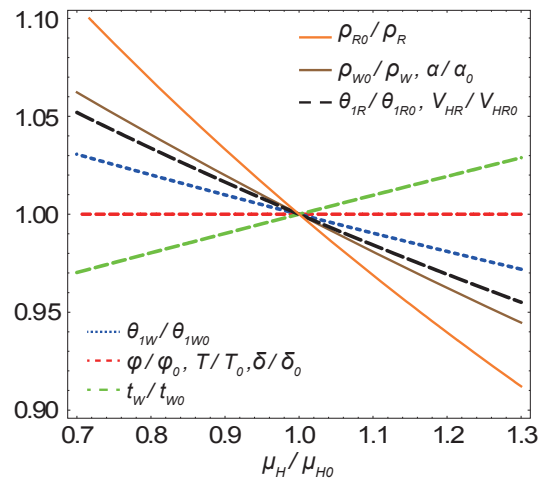


Figure 3.14 – Effect of the normalized mass of the head μ_H/μ_{H0} .

With the consideration that cross section area of club shaft is a certain value, parameters η_S and μ_{JS} is determined. Assuming that mass distribution of club shaft is uniform, defined $\mu_{JS} = 1/2$ and $\mu_{JS} = 1/12$. Parameters related to release point are μ_H , μ_S , μ_W , μ_H , γ , and α . Defined standard conditions $\mu_W = 0.016$, $\mu_H = 0.08$, $\mu_{SH} = 0.25$, $\gamma = 1.3$, $\alpha = \pi/2$, and $\tau = 0$. In figure 3.14, figure 3.15, figure 3.17~3.21, horizontal axis is zoomed 0.7 ~ 1.3 times around standard conditions, vertical axis represents normalization results of standard conditions. In figure 3.22, horizontal axis is zoomed 0 ~ 2 times, subscript 0 represents results derived by standard conditions.

According to equation 3.24, 3.26, and 3.27, there is no relationship between ϕ (η_{R2} , η_{R2E}) and parameters μ_H and μ_W . Dimensionless inertia moment ρ_W and ρ_R decreases with increasing μ_H and μ_W . As show in figure 3.4, m_H located at the top of link 2, and m_{BW} located at link 1. Distance between m_H and mass rotation center is bigger than that of m_{BW} . As shown in

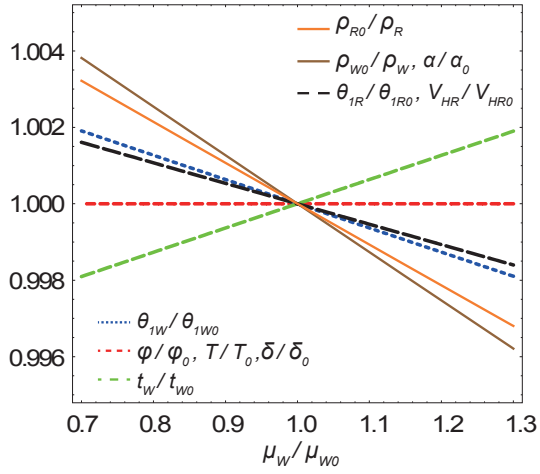


Figure 3.15 – Effect of the normalized mass of the grip μ_W/μ_{W0} .

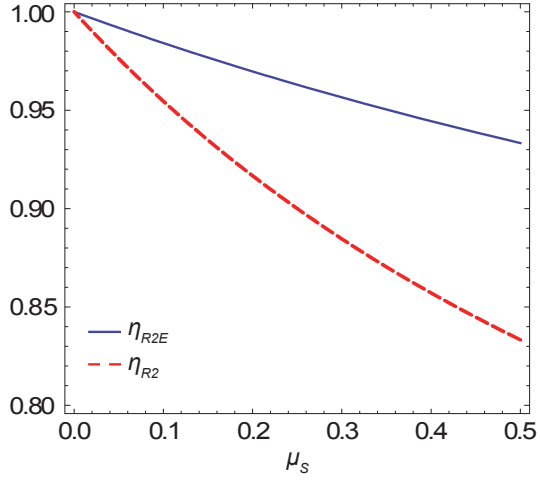


Figure 3.16 – Effect of the normalized mass of the shaft μ_S .

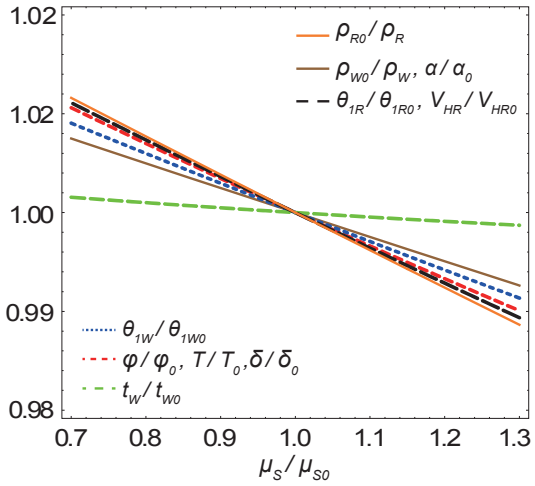


Figure 3.17 – Effect of the normalized mass of the shaft μ_S/μ_{S0} .

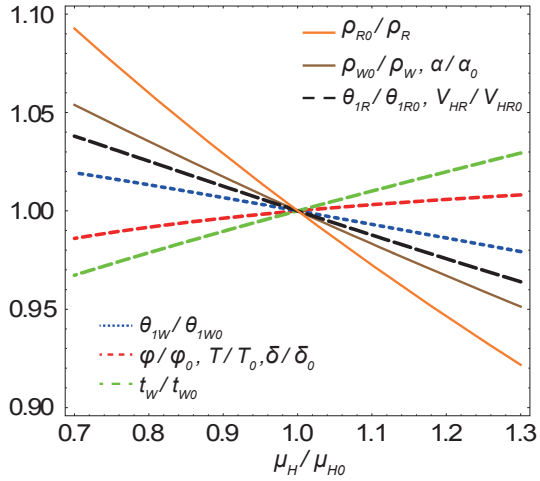


Figure 3.18 – Effect of the normalized mass of the head m_H/m_{H0} .

figure 3.14 and 3.15, with the same change of m_H and m_{BW} , m_H exerts more influence. ρ_R and θ_{1R} significantly changes compare to ρ_W and θ_{1W} against the change of μ_H . To the contrary, ρ_W and θ_{1W} significantly changes compare to ρ_R and θ_{1R} . δ and T do not change with the change of μ_H and μ_W . θ_{1W} which is inverse proportion to $\sqrt{\rho_W}$ increases with decreasing μ_W . Likewise, θ_{1R} increases with decreasing μ_W .

Figure 3.16 is the effect of the normalized mass of the club shaft μ_S on η_{R2} and η_{R2E} . Both parameters become to be larger in relation to the decrease of μ_S . μ_S is related to shaft material properties. Compared to μ_H and μ_W , μ_S exerts an influence on ϕ (η_{R2} , η_{R2E}) which is one of

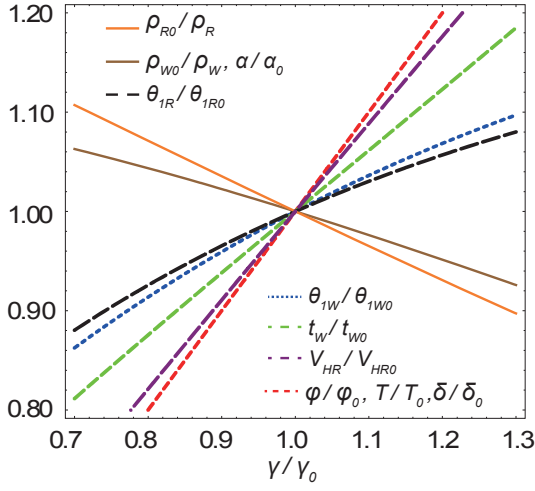


Figure 3.19 – Effect of the normalized club length γ/γ_0 without balanced mass of the club.

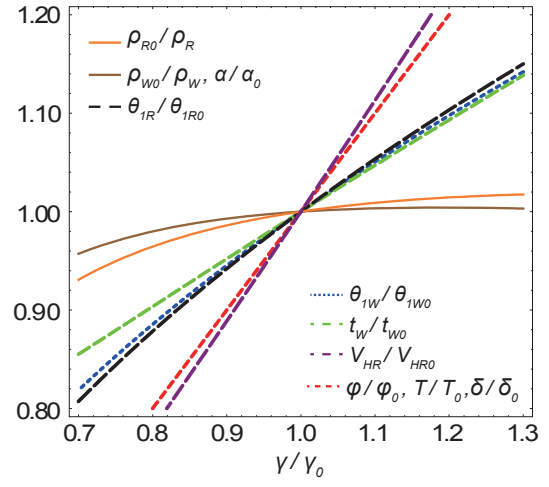


Figure 3.20 – Effect of the normalized club length γ/γ_0 with balanced mass of the club.

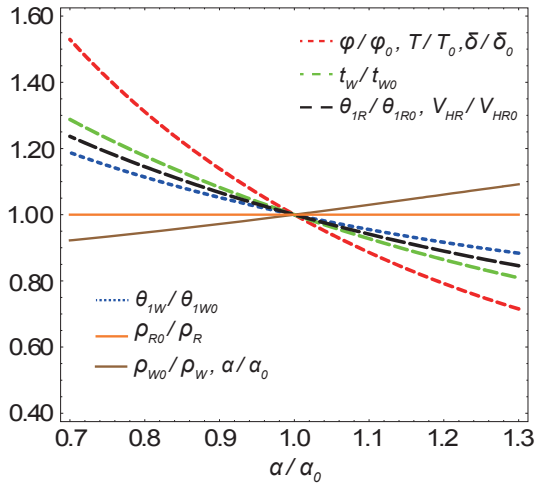


Figure 3.21 – Effect of the normalized supplementary angle of the cock angle α/α_0 .

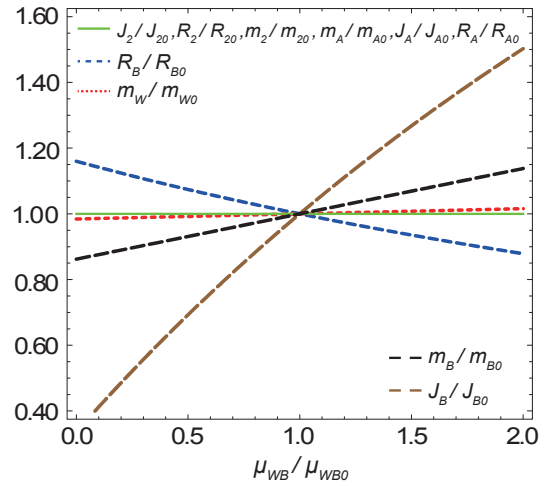


Figure 3.22 – Effect of the normalized mass of the grip.

elemental parameters of release point. With the decreasing of μ_S , the gravity center of golf club moves along with club head direction, R_2 is increasing. As shown in figure 3.16, with decreasing of μ_S , gravity center and equivalent length of club moves to the club head. In extreme condition $\mu_S = 0$, gravity center located at club head position.

With the decreasing of μ_S not only T and δ , but also angular acceleration α , angular velocity θ_{1W} , equivalent angular velocity θ_{1R} , and V_{HR} are increasing. Figure 3.17 shows that the effect of the normalized mass of the grip. ϕ and $1/\rho_W$ were counterbalanced, t_W does not vary. As

shown in figure 3.18, ϕ does not vary with increasing of μ_H . ϕ increases with decreasing of μ_S . With the increasing of m_H , ρ_R and ρ_W is obviously increasing. However, ρ_R and ρ_W increases in a small extent in the condition that m_S is certain and μ_H is varying.

Figure 3.19 shows the effect of the normalized club length γ/γ_0 . According to equation 3.27, γ varies directly with ϕ . T and δ are in proportion to γ , at the meantime. According to equation 3.28, ρ_W and ρ_R increase with increasing of γ . The variation extent of ρ_R is more obvious. Compared to ϕ , $1/\rho_W$ and $1/\rho_R$ varies to a small extent. According to this result, γ is also increased with θ_{1W} , θ_{1R} . Moreover, V_{HR} is increased and t_W is decreased with the change of γ . Motion power T , angular velocity θ_{1W} , equivalent angular velocity θ_{1R} , V_{HR} increases with the change of γ .

Figure 3.20 shows the effect of the normalized club length γ/γ_0 with balanced mass of the club. According to equation 3.27, α varies inversely with the γ . It means ϕ decreased with decreasing of cock angular χ . T and δ decreased at the meantime. According to equation 3.28, $1/\rho_W$ increases with increasing of α . $1/\rho_R$ does not vary. $\dot{\theta}_{1R}$ and V_{HR} vary inversely with α . α increases with increasing θ_{1W} . t_W also increased. On the contrary, T , θ_{1R} , θ_{1W} , V_{HR} increases with decreasing α .

3.4 Discussion

The simulation results indicated that the increasing acceleration pattern provided a slight advantage in club head speed at impact (44.7 vs. 44.0 m/s) when compared with a normal swing with decreasing and constant acceleration patterns, respectively, as shown in figure 3.9. However, to be effective, the increasing acceleration technique required that the wrist joint muscle torque generator had to be activated following the moment of release, and kept activated up until the point of impact with the ball. Without this active wrist torque following the increasing acceleration, the club head reached a maximum speed at impact of only 38.9 m/s (figure 3.9). The sensitivity of the simulation to the timing of the wrist torque has been previously reported. It was found that for decreasing acceleration pattern, activating the wrist torque 50 m/s prematurely reduced the club head speed at impact by approximately 2 percent, whereas activating the wrist torque late resulted in a 4.6 % reduction.

The length of time to complete the downswing was longer for decreasing acceleration when no delay was used, than for constant acceleration where a delayed release was used. These values are comparable with a value of 0.34 s measured from video for a professional golfer, whose club head speed at impact was approximately 5 m/s faster. As previously reported

[Sprigings and Neal(2000)], the sequence of segment positions during golfer's downswing were markedly similar to those produced during both decreasing and constant acceleration patterns. In the current study, the longer swing time required for the non-delayed release technique was a result of greater torso rotation being used during the downward swing by the optimization process in order to satisfy the penalty constraint that the club shaft be vertical at impact. For the increasing acceleration pattern, the maximum muscle energy 600 W generated during the downswing was produced by the muscles crossing the wrist joint as shown in Figure 3.10. The maximum instantaneous component of joint power recorded for any segment during the entire downward swing emanated from the joint forces created at the wrist joint as a result of the proximal to the double pendulum system. In increasing acceleration condition, a breakdown of the club's energy history into its sources by mathematically integrating the resultant joint force energy and resultant muscle energy history curves at the grip end of the club revealed that the primary energy source originated from the passive joint forces created at the wrist joint by the kinematics of the swing. However, one must be remembered that these seemingly passive joint forces are actually a consequence of the dynamic movements of the golf club and arm segments that are themselves dependent on muscle energy. The muscle energy, created by active wrist torque following the release, supplied an additional energy to the swing as shown in Figure 3.11. It is evident that the energy contribution from the wrist muscular torque began before the instant that wrist cock release was initiated. Because the relative wrist angle was being maintained during this pre-release phase, the muscles associated with providing wrist torque were actually transferring, rather than generating, energy through to the club from the arm segment during this pre-release stage.

Examining the energy flow from the arm, to the golf club, it was observed that initially energy entered the arm via its muscle torque generators which produce arm rotation. When the arm torque muscular generator was activated, energy began to leave the arm, as a result of the opposing wrist torque on the distal end of the arm segment, and flowed into the proximal end of the arm. Externally, this was observed as a slowing down of the arm's rotation as the arm picked up rotational speed as shown in Figure 3.12. In terms of energy flow, this corresponds to energy leaving the distal end of the arm segment via the wrist musculature and flowing into the club segment via the same muscle system [Winter(2009)].

According to equation 3.20, if $Q_{2W} = 0$, parameter $\lambda = 1$. λ decreases with increasing Q_{2W} . Based on equation 3.14~ 3.17, t_W , $\theta_1 W$ decreases in proportion to $\sqrt{\lambda}$ with increasing Q_{2W} . T , δ decreases in proportion to λ with increasing Q_{2W} . As shown in figure 3.13, Effect of the active wrist torque τ on the normalized parameter λ . It can be seen that λ becomes to be

smaller considerably as the normalized active torque τ becomes to be larger. $T, \delta, \theta_{1W}, \theta_{1R}, V_{HR}, t_W$ decreases with decreasing λ . Therefore, Q_2 is active torque exerted on wrists from top position to the release point. When reached to release point, $Q_2 = Q_{2W}$ become obstructed to late hitting.

Figure 3.22 shows Effect of the normalized mass of the grip μ_{WB} on the on the conventional model parameter and that on the proposed model parameter. According to traditional club model, parameters of link 2: the distance between grip and gravity center $R_2 = R_B$, inertia moment $J_2 = J_B$, mass $m_2 = m_B$; parameters of link 2: mass $m_1 = m_A$. These parameters are normalized and represented by R_B, J_B, m_B , and m_A . According to proposed model, corresponding parameters are R_2, J_2, m_2 , and m_{1W} .

According to figure 3.22, parameters of link 2: m_B, R_B , and J_B effected by ϕ varies in different direction. Calculate ϕ, ρ_W , and ρ_R , results are similar to these shown in figure 3.15. ϕ did not vary. ρ_W and ρ_R varied to a small extent. Because m_B and J_B increase at the meantime R_B decreases, it is difficult to investigate the changing trend of ρ_W and ρ_R with calculation of ϕ . On the contrary, based on proposed model, parameters of link 2 being equal, in the light of this, ϕ is equal. Moreover, because equivalent mass of link 1 m_W slightly increased, it is easy to sketch that ρ_W and ρ_R also increased correspondingly.

3.5 Summary

In this chapter, the purpose of the present research was to examine the theoretical benefit to club head speed that a natural release produced based on expressions of angular velocity and angular acceleration during downswing process. Initially, a 2-dimensional double pendulum was established to confirm that the assumptions for simulation were met. Then, expressions based on dynamic swing motion equations were deduced to demonstrate effects of the parameters of a golf club on the dynamic behavior at the release point. Following this, the main analysis was carried out with regards to the hypotheses presented in the section 3.2.

1. In this study, it was found that the increasing acceleration before release point, using a resistive wrist torque, provided a small benefit in terms of increasing club head speed at impact, but the percentage gain in club head speed was approximately half that previously reported by other researchers. Whether the additional gains in club head speed are worth the additional complexity introduced into the timing of the swing is left up to the golfer to decide.
2. The increasing acceleration pattern gives the maximum club head speed at impact.

Golfers who turn wrists freely or use a negative wrist torque can achieve the optimum ball position by the impact criterion, where the club shaft is vertical at impact when viewed face on.

3. A new golf club model was proposed instead of the traditional one. It can be seen that based on the new club model it is easy to sketch variation trends of club parameters and their effects on the cock angle and the active wrist torque at the release point.

4 Marker-based Tracking Method

4.1 Introduction

Human tracking can be performed using intrusive techniques, requiring the tracked subject to wear specific clothes, or markers. It requires actors to wear dark clothes with markers. The markers' 3D positions are then evaluated by multiple cameras across the activity volume often with sub-millimetre accuracy. As the markers are reflective spheres, this system is considered as passive. Further constraints based on the spatial relationship between the markers allow identifying precisely the body's elements. It should be mentioned that because the markers or sensors are usually placed on the subject's skin, issues due to soft tissue deformation can in fact introduce large errors [Archer and Castillo(2006)].

Different techniques to reduce the effect of these errors on the estimated joint kinematics have been proposed [Chiari and Della Croce(2005)]. [Spoor and Veldpaus(1980)] estimated the positions and orientations of each body segment separately using a segmental optimisation method (SOM). SOM minimises the marker displacement in the segmental reference frame between any two time instants. [Lu and O'Connor(1999)] used a multi-link model relating the marker positions to the generalized co-ordinates that describe the motion of the body segments along the degrees of freedom (DOFs). At each time instant, their global optimisation method (GOM) estimates all generalized co-ordinates at once from a weighted nonlinear least-squares fit between the measured marker positions and those predicted by the model. GOM outperformed SOM in simulation for a serial three-link model (pelvis, thigh, and shank) joined by two spherical joints (hip and knee), suggesting that imposed joint constraints reduce the effect of errors. [Cerveri and Rabuffetti(2003)] used a Kalman filter to estimate joint kinematics. Kalman filtering (KF) is based on a measurement model obtained from the biome-

chanical model and a process model, which includes prior knowledge about the smoothness of the motion. In addition, the generalized co-ordinates, velocities, and accelerations are estimated simultaneously. [Cerveri and Pedotti(2005)] proposed local marker estimation (LME), an extension of KF to estimate marker displacements in the segmental reference frames to account for STA. In their simulation study in which systematic, sinusoidal perturbations added to the three thigh markers modelled STA, LME estimates were at least 50% more accurate than SOM estimates. eliminates the need to differentiate generalized co-ordinates numerically, which can introduce large errors. As these accelerations, in addition to the measured ground reaction forces, are the input for inverse dynamics to calculate joint moments, more accurate joint acceleration estimates will improve the accuracy of joint kinetics. Since Cerveri did not compare LME with GOM, these advantages have not yet been confirmed.

As described in chapter 1, it is necessary to compare results (such as velocity, acceleration, and angular displacements) obtained with wearable sensor system with the results obtained using a laboratory bound camera system. Considering the propensity of marker-based tracking methods, the purpose of this chapter is to compare the accuracies of the generalized co-ordinates and accelerations using GOM, KF, LME, and KS using both simulated marker trajectories, with and without modelling errors. Furthermore, the results of the validation studies performed will be presented.

4.2 Optical Tracking Systems

Vicon Tracker - Vicon Motion Systems Ltd. provides high-end solutions for optical tracking. Vicon Tracker (figure 4.1) is a passive infrared marker tracking system that consists of multiple cameras equipped with IR LEDs and IR optical filters, and a set of retro-reflective markers positioned on the objects to be tracked. Retro-reflective markers are passive markers, which do not generate light themselves. They are normally coated with retro-reflective material that reflects the IR radiation from the IR LEDs into the direction of the incoming radiation. The IR-pass optical filter mounted on the camera lenses filters out other spectrum and only keeps the one reflected by the markers. As a result, markers will appear as bright spots in the image of the cameras which can easily be detected. The system calculates the center of each marker and reconstructs its 3D position in the tracking volume. At least 4 markers and 3 cameras are required to provide 6 DoF information. The Vicon cameras shown in Figure 1.5 are designed, developed and built specifically for motion tracking applications. The Vicon MX13 camera, for example, is equipped with a CMOS image sensor which works in infrared (875 nm wavelength) region. The frame rate with full resolution (1280×1024) is 482 fps. The on-board processing



Figure 4.1 – T-Series, Vicon MX camera (adapted from internet)

capability allows complex marker detection algorithms to be performed in real time.

The independently measured positional accuracy (average absolute error through a large 3D space) reported by the vendor is 0.1 mm and the angular accuracy is 0.15 degree. The overall tracking latency is limited within 10ms in general. The update rate ranges from 200Hz to 1000Hz depending on the resolution of the camera.

ARTTRACK System - Similar to Vicon Tracker, the ARTTRACK System (figure 4.2) developed by Advanced Realtime Tracking GmbH is an infrared-based marker tracking system. The system utilizes two or more cameras to obtain the tracking information. All tracking cameras are equipped with a low-noise CCD sensor and embedded processors to accelerate the analysis of the marker data. The cameras also have built-in infrared flashes (880 nm wavelength) to illuminate the tracked objects. Flashes are synchronized by an external sync signal, which is provided to each camera. One ARTTRACK system can contain maximally 16 cameras. Spherical retro-reflective markers are used in the system. To get the 6 DoF information, at least 4 markers must be attached to the object. The maximum update rate of the ARTTRACK System is 60 Hz.



Figure 4.2 – ARTTRACK System (adapted from internet)

According to the product information from the vendor, the accuracy results are 0.4 mm in position estimation and 0.12 degree in orientation estimation.

Chapter 4. Marker-based Tracking Method

Raptor-4 Digital Realtime system - the Raptor-4 Digital Realtime System from Motion Analysis Corporation is a passive optical tracking system based on retro-reflective markers.

The system consists of the Raptor-4 digital cameras and the Cortex software, which capture complex motion at high accuracy. The Raptor-4 Digital Camera has a CMOS image sensor with a large pixel array (2352×1728). Each camera is equipped with 323 LEDs around the lens. The powerful on-board processing capability allows the system to operate at 166Hz with full resolution and up to 10,000Hz with partial resolution. The accuracy data is not directly provided by the vendor. However, according to the technical specification, Raptor-4 is the only optical tracking system that satisfies the accuracy requirement of the broadcast tracking applications - $1/100^{th}$ of a degree



Figure 4.3 – Raptor-4 Digital Realtime system (adapted from internet)

Optotrak Certus Motion Capture System - The Optotrak certus motion capture system (figure 4.4) is a 6 DOF motion measurement system made by Northern Digital Inc. Unlike Vicon, ARTTRACK and Raptor-4 trackers Optotrak makes use of active marker

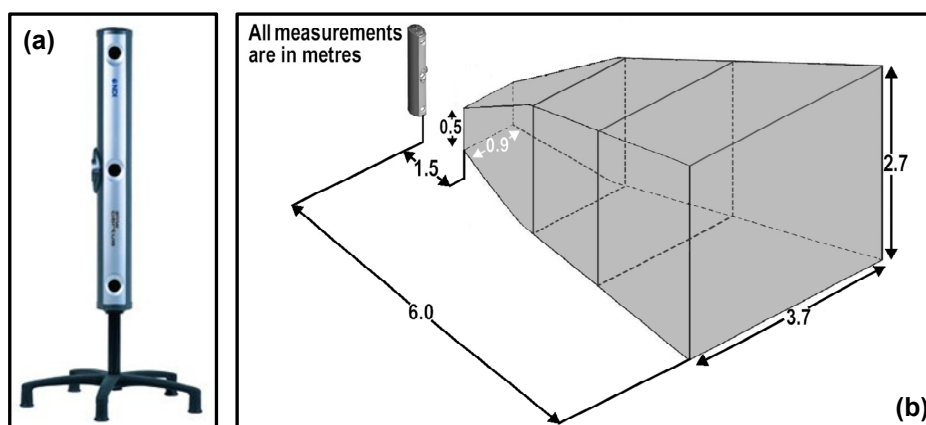


Figure 4.4 – Optotrak certus motion capture system (adapted from internet), (a)Optotrak Certus; (b)measurement volume.

technology. Active markers are infrared light emitting devices, mostly using LEDs. The disad-

vantage of active markers is that each marker requires wires and electronic circuits, making them less compact than passive markers. However, active markers usually appear as even brighter spots in the captured images than passive markers and are thus more easily detectable. In the Optotrak system, synchronized markers are placed on the moving objects which are tracked by three cameras mounted on a rigid base. Each camera is equipped with an infrared optical filter. The active markers (LEDs) are connected to a central control unit, which turns on and off the LEDs in sequence. In this way, the LED that has been activated can be identified by the system at any point in time. To get the 6 DOF information, at least one LED must be visible for the position estimation and at least three must be visible for the orientation estimation. Maximum number of markers supported by the system is 512. The maximum marker scanning frequency reaches 4600 *Hz*, which corresponds to about 1500 *Hz* of overall system frame rate. According to the technical specifications provided by the vendor, the 3-dimensional accuracy in position is 0.1 *mm*. There was no information available regarding the accuracy in orientation.

4.2.1 Feature extraction

Camera calibration is an essential part of optical tracking where the relationship between the 3D world defined by the physical tracking area and the 2D image plane defined by the image captured by each camera is determined.

The purpose of camera calibration is to determine the internal and external parameters used in the camera model discussed above. Since the distortion parameters do not change when moving a camera, they are usually regarded as internal parameters.

A wide range of different camera calibration methods have been reported in the literature. One widely used technique was developed by [Zhang(2000)]. Zhang's approach requires the camera to observe a planar pattern shown at a few (at least two) different orientations. At first, corners of the checkerboard pattern are extracted and located with sub-pixel precision. Then the algorithm computes the projective transformation between the corner points of n different images. Afterwards, the camera internal and external parameters are recovered using a closed-form solution, while the third-order and fifth-order radial distortion terms are recovered within a linear least-squares solution. A final nonlinear minimization of the re-projection error refines all the recovered parameters [Lu et al.(2004) Lu, Zhang, Wu, and Li].

4.2.2 Pinhole camera model

The pinhole camera model is the simplest and an ideal camera model that is suitable for many computer vision and computer graphics applications. It defines a geometric mapping between the 3D world and a 2D image.

As illustrated in figure 4.5, a pinhole camera is modeled by its optical center C and the image plane R . The line through C and orthogonal to R is called the optical axis. The point at which the optical axis intersects R is referred to as the principal point p_0 . f represents the focal length which is determined by the distance between C and R .

A point in 3D space M is mapped to an image point m where the line through C and M intersects with R . Using similar triangles shown in figure 4.6, we can derive that the point $M(X, Y, Z)^T$ is mapped to the point $m(fX/Z, fY/Z, f)$ on the image plane. Ignoring the final

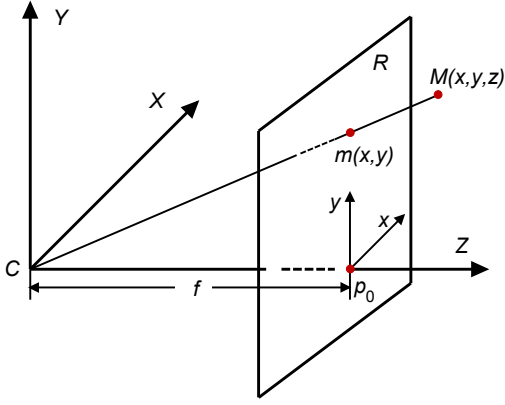


Figure 4.5 – Pinhole camera model

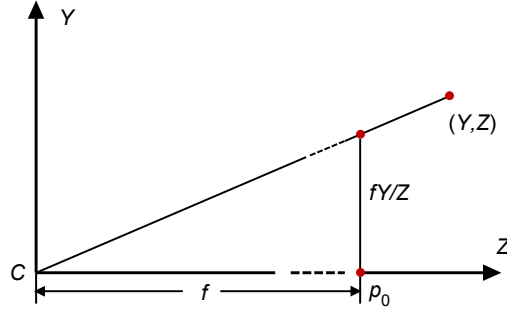


Figure 4.6 – Similar triangles of a pinhole camera model

image coordinate, mapping relationship can be described as:

$$(X, Y, Z)^T \rightarrow (fX/Z, fY/Z)^T \quad (4.1)$$

If homogeneous vectors are used to represent the world and image points, then equation (4.1) can be written in terms of matrix multiplication:

$$\begin{pmatrix} X \\ Y \\ Z \\ 1 \end{pmatrix} \rightarrow \begin{pmatrix} fX \\ fY \\ Z \end{pmatrix} = \begin{bmatrix} f & 0 \\ f & 0 \\ 1 & 0 \end{bmatrix} \begin{pmatrix} X \\ Y \\ Z \\ 1 \end{pmatrix} \quad (4.2)$$

Let M represent the homogeneous vector of a world point in 3D space $(X, Y, Z, 1)^T$ and m represent the homogeneous vector of an image point in 2D space, equation (4.2) can be compactly written as:

$$m = P \cdot M \quad (4.3)$$

where P is a 3×4 matrix called camera projection matrix. It can be expressed as:

$$P = \begin{bmatrix} f & & & \\ & f & & \\ & & 1 & \end{bmatrix} \begin{bmatrix} 1 & 0 & \\ & 1 & 0 \\ & & 0 \end{bmatrix} = K [I_3 | 0] \quad (4.4)$$

The 3×3 matrix K in equation (4.4) is called the camera calibration matrix. So far, it solely depends on the focal length f .

In equation (4.1), assumed that the origin in the image space is at the principal point. In practice, the origin of an image usually lies in the top-left corner of the image. Thus, equation (4.1) can be more generally written as:

$$(X, Y, Z)^T \rightarrow (fX/Z + u_0, fY/Z + v_0)^T \quad (4.5)$$

where $(u_0, v_0)^T$ are the coordinates of the principal point. Equation 2.5 can be expressed in homogeneous coordinates as:

$$M = \begin{pmatrix} X \\ Y \\ Z \\ 1 \end{pmatrix} \rightarrow m = \begin{pmatrix} fX + Zu_0 \\ fY + Zv_0 \\ Z \end{pmatrix} = \begin{bmatrix} f & u_0 & 0 \\ & f & v_0 & 0 \\ & & 1 & 0 \end{bmatrix} \begin{pmatrix} X \\ Y \\ Z \\ 1 \end{pmatrix} \quad (4.6)$$

Refine the camera calibration matrix K to:

$$K = \begin{bmatrix} f & & u_0 \\ & f & v_0 \\ & & 1 \end{bmatrix} \quad (4.7)$$

Then equation (4.6) can be rewritten as:

$$m = K [I | 0] M \quad (4.8)$$

In general, points in space will be expressed in terms of a world coordinate system. The

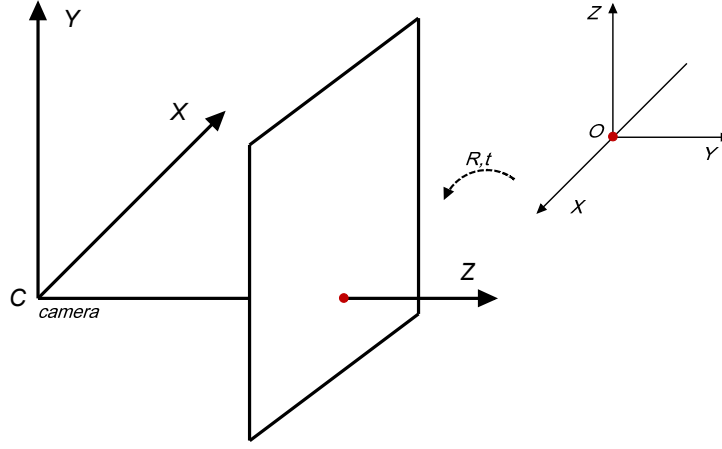


Figure 4.7 – Transformation between the camera and world coordinate frame

camera coordinate system and the world coordinate system are related via a rotation and a translation (figure 4.7). Now let M be a 3-vector representing the coordinates of a point in the world coordinate frame and M' be a 3-vector representing the same point in the camera coordinate frame. M' can be expressed by equation (4.20)

$$M' = R(M - C) \quad (4.9)$$

where R is a 3×3 rotation matrix that represents the orientation of the camera coordinate frame and C represents the coordinates of the camera center in the world coordinate frame. Using homogeneous coordinates, rewritten equation (4.20) as:

$$M' = \begin{bmatrix} R & -RC \\ 0 & 1 \end{bmatrix} \begin{pmatrix} X \\ Y \\ Z \\ 1 \end{pmatrix} = \begin{bmatrix} R & -RC \\ 0 & 1 \end{bmatrix} M \quad (4.10)$$

Combining equation (4.8) with equation (4.10):

$$m = KR[I - C]M \quad (4.11)$$

where, M is in a world coordinate system. Until now, it is assumed that the image coordinates are scaled by the same factor in both horizontal x and vertical y directions.

However considering the fact that pixels of a real CCD or CMOS camera are not squared, which means that there are unequal scale factors between x and y directions of the image

when measuring point coordinates in pixels. Let m_x and m_y be the number of pixels per unit distance in the x and y direction in image coordinates, then write the camera calibration matrix in the general form:

$$K = \begin{bmatrix} a_x & & u_0 \\ & a_y & v_0 \\ & & 1 \end{bmatrix} \quad (4.12)$$

where, $a_x = f m_x$ and $a_y = f m_y$ represent the focal length in the x and y direction in terms of pixel dimensions.

There is one more parameter need to be considered, which is referred to as the skew parameter s . For most normal cameras, s will be zero. However, it can take non zero values under unusual conditions, e.g., the image plane is not perpendicular to the optical axis. By adding the skew parameter s , the camera calibration matrix can be extended as:

$$K = \begin{bmatrix} a_x & s & u_0 \\ & a_y & v_0 \\ & & 1 \end{bmatrix} \quad (4.13)$$

Based on equation (4.11), generalize the projection matrix P to the form:

$$P = KR[I| -C] = K[R|t] \quad (4.14)$$

where, $t = -RC$. This is the general mapping given by a pinhole camera. In equation (4.14), the parameters contained in K are called the internal camera parameters, and the parameters determined by R and C are called external camera parameters.

4.2.3 3D reconstruction

The Epipolar geometry provides an alternative for finding the relationship between feature points in images captured by different cameras. When two cameras view a 3D scene from two distinct positions, there are a number of geometric relations between the 3D points and their projections onto the 2D images that lead to constraints between the image points. These relations are derived based on the assumption that the cameras can be approximated by the pinhole camera model (figure 4.1). Consider a stereo setup composed by two pinhole cameras whose principal axes are non-collinear, as illustrated in figure 4.8. Let C_l and C_r represent the optical centers of the left camera and the right camera respectively. A 3D point M is

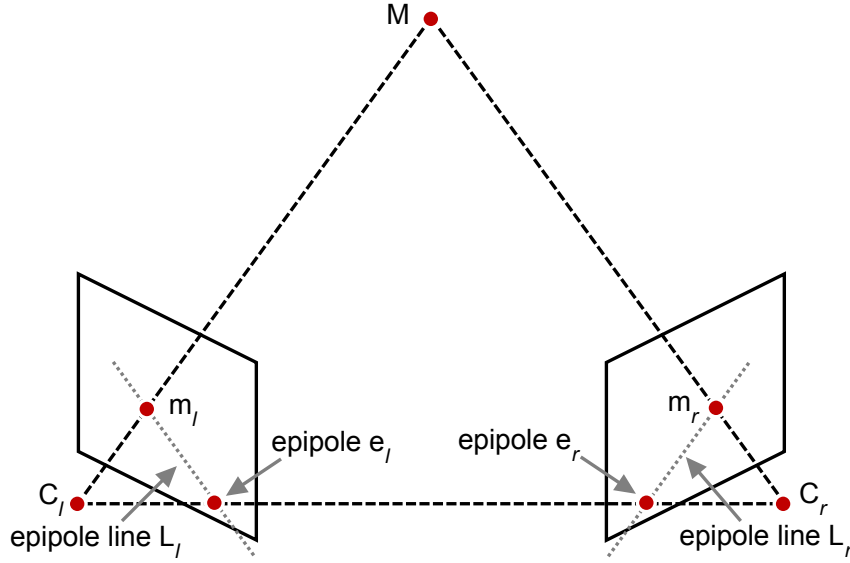


Figure 4.8 – Epipolar geometry

projected onto both image planes, resulting in the 2D point pair m_l and m_r . The epipolar plane is determined by the point M and the two camera optical centers C_l and C_r . Given m_l , its corresponding point in the right image is constrained to lie on a line called the epipolar line L_r , which is the intersection of the epipolar plane with the image plane of the right camera. The same is valid for m_r , whose corresponding point must lie in the epipolar line L_l in the image plane of the left camera.

Based on this observation, we can make use of the epipolar constraints to find the correspondence between two feature points. The epipolar constraints is that, for a given point p_1 in image 1, its possible matches in image 2 must lie on the epipolar line of p_1 . As a result, the search space for a correspondence finding is reduced to one dimension.

4.3 Materials and Methods

4.3.1 Kalman Smoothing Algorithm

A drawback of Kalman filtering is the asymmetrical use of data. At each time instant, estimates are based on the measured marker trajectories up to the considered time instant only. Therefore Kalman smoothing is proposed, a combination of two filters, to calculate the estimates at each time instant based on the complete marker trajectories. The proposed KS is an extension of the Kalman filter without LME.

The Kalman smoother combines prior knowledge, described by a process and measurement model, with the measured marker trajectories to produce an estimate of the joint kinematics while minimising the estimation error statistically. The generalized co-ordinates q and their derivatives up to the K th order, which describe the joint kinematics, are collected in a vector x :

$$x = \left[q_1 q_1^{(1)} \dots q_1^{(K)} q_2 q_2^{(1)} \dots q_2^{(K)} \dots q_J q_J^{(1)} \dots q_J^{(K)} \right]^T \quad (4.15)$$

where, $j = 1, \dots, J$ indicating the DOF and $q_j^{(K)}$ the k th time derivative of q_j .

The process model describes the expected time evolution of the joint kinematics x and is composed of J submodels describing the motion of each DOF. While the submodels are based on the assumption that the K th derivative of the generalized coordinate $q_j^{(K)}$ is constant, a noise term n_j takes into account the errors introduced by this assumption:

$$\begin{bmatrix} q_j(t_i + \Delta t) \\ q_j^{(1)}(t_i + \Delta t) \\ \vdots \\ q_j^{(K)}(t_i + \Delta t) \end{bmatrix} = \begin{bmatrix} 1 & \Delta t & \frac{\Delta t^2}{2} & \frac{\Delta t^K}{K!} \\ 0 & 1 & \Delta t & \frac{\Delta t^{K-1}}{(K-1)!} \\ 0 & & & 1 \end{bmatrix} \begin{bmatrix} q_j(t_i) \\ q_j^{(1)}(t_i) \\ \vdots \\ q_j^{(K)}(t_i) \end{bmatrix} + n_j(t_i) \quad (4.16)$$

where, t is the time, Δt is the sampling time. The $(K + 1)$ th derivative of the generalized coordinate is modelled as zero mean Gaussian noise with covariance $\sigma_{K+1,j}^2$. Therefore, the process noise is given by:

$$n_j^{(t)} = N(0, Q_j) \quad (4.17)$$

$$\text{where, } Q_j = \sigma_{K+1,j}^2 G^T G \quad (4.18)$$

$$G = \begin{bmatrix} \frac{\Delta t^{K-1}}{(K-1)!} & \frac{\Delta t^K}{K!} & \Delta t \end{bmatrix}$$

The measurement model relates the joint kinematics $x(t)$ to the measured marker positions, collected in $z(t)$. This model is composed of a noiseless measurement model $h(x(t))$ and measurement noise $v(t)$:

The noiseless measurement model $h(x(t))$ is based on a biomechanical model consisting of ten body segments including 21 DOFs. The measurement noise, $v(t)$ is drawn from a zero mean Gaussian distribution and expresses the uncertainty for the marker position measurements.

KS has two consecutive steps. First, a Kalman filter [Kalman(1960)] estimates the joint kinematics at t_i using only the measured marker trajectories up to t_i . Second, a backward recursion using the measured marker trajectories from the last instant down to t_i , follows the Kalman filter. The resulting Kalman smoother estimates the generalized co-ordinates and their derivatives based on all the information available: the complete marker trajectories, the process model, and the measurement model. An extended smoother [Bar-Shalom and Li(1993)] is used to cope with the nonlinearity of the measurement model.

Biomechanical model is adopted to calculate three sets of marker trajectories from the kinematics of a gait motion described by generalized coordinates q_{gt} (ground truth): (1) ideal marker trajectories without errors, consistent with q_{gt} and the biochemical model; (2) marker trajectories with instrumental errors, obtained by adding zero mean Gaussian noise with standard deviation of 1 *mm* to the ideal marker trajectories; (3) marker trajectories corrupted with STA calculated as explained below.

4.3.2 Simulation

STA are related to the angles of adjacent joints [Cappozzo and Catani(1996)]. Calculated such a relation from marker trajectories measured experimentally during gait. Inverse kinematics (SIMM, Motion Analysis Corporation) estimated the generalized coordinates $q_{exp}(t)$ corresponding to these trajectories. Using the biomechanical model, the measured marker positions were projected in the segmental reference frame. We considered the time dependent distances between the projected and modelled marker positions to be an approximation of the STA. For each marker, this distance, $d(t)$ was calculated along the X -, Y -, and Z -direction of the segmental reference frame and a linear relation between this distance and the adjacent joint angles $q_{exp,l}$ was calculated using least-squares:

$$\min_a \left[\sum_{i=1}^l \left(d(t_i) - \sum_{l=1}^L a_l q_{exp,l}(t_i) \right)^2 \right] \quad (4.19)$$

where, $l = 1, \dots, L$ indicating the adjacent joints. The resulting coefficients a_l were used to calculate the modelled STA as:

$$\sum_{l=1}^L a_l q_{gt,l}$$

The modelled STA, as shown in figure 4.9, had amplitudes between 5 *mm* and 25 *mm*. It should be noted that, in contrast to the observations of [Cappozzo and Catani(1996)], the X -

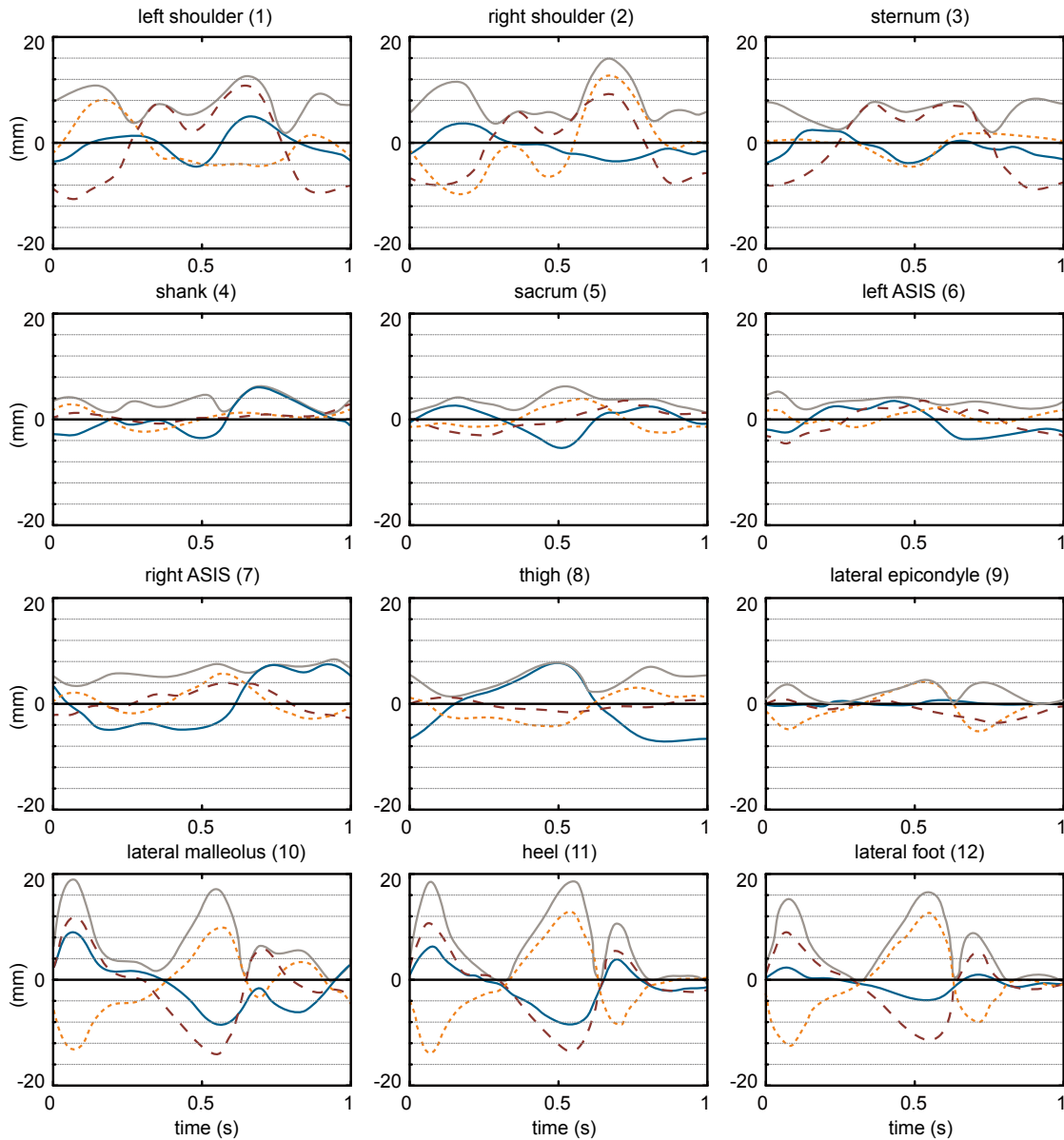


Figure 4.9 – Time trajectories of the simulated STA for the markers on the trunk, pelvis and right leg: X-component (dotted black), Y-component (solid black), Z-component (dashed black) in the segmental reference frame and magnitude (gray).

and Z-components of the STA trajectories in the shank and foot are correlated in the data set. Applied GOM, KF, LME, and KS to the simulated marker trajectories.

All methods were based on the biomechanical model of [Delp and Loan(1990)]. The algorithm for inverse kinematics implemented in SIMM [Delp and Loan(1990)] calculated the GOM estimates according to [Lu and O'Connor(1999)]. SIMM uses the Levenberg–Marquardt algorithm [Moré(1978)] to solve the underlying nonlinear least-squares problem with the estimated gen-

eralized coordinates at the previous time instant as initial values. KF used a third-order process model. LME was applied to all 30 markers. As recommended by [Cerveri and Pedotti(2005)], a second-order process model was used and the covariance associated with the local marker coordinates was two orders of magnitude smaller than those associated with the generalized coordinates. To investigate the influence of the order of the process model, we performed KS for $K = 2$, $K = 3$, and $K = 4$.

The effect of modelling errors was investigated by applying GOM, KF, and KS to the ideal marker trajectories using a biomechanical model that differed from the model used to simulate marker trajectories. The studied modelling errors were a thigh length increased by 10% and a dislocation of the joint centre of the hip of 16.8 *mm*.

For all estimates, we calculated the marker error, i.e. the root mean square (RMS) distance between the simulated marker trajectories and those predicted by the estimates and the biomechanical model averaged over all markers, \bar{d}_{RMS} . Thereafter we calculated the percentage error for the generalized coordinates averaged over the 21 DOFs, ε_{pos} :

$$\varepsilon_{pos} = \frac{1}{J} \sum_{j=1}^J 100 \frac{\sqrt{(1/I) \sum_{i=1}^I (q_j(t_i) - q_{gt,j}(t_i))^2}}{\max(q_{gt,j}) - \min(q_{gt,j})} \quad (4.20)$$

where q_j is the considered position estimate of coordinate j , $\min(q_{gt,j})$ and $\max(q_{gt,j})$ are, respectively, the extreme values of coordinate j during gait. Likewise, calculated the percentage errors for the generalized accelerations, ε_{acc} , for KF, LME, and KS.

Since GOM does not yield acceleration estimates, calculating generalized accelerations and joint moments requires double differentiation of the position estimates. To study the effect of numerical differentiation on the quality of the joint moment calculation, we calculated joint moments using SIMM dynamics pipeline and SD Fast (Motion Analysis Corporation, PTC Inc.) for three different joint kinematics: the ground truth, the estimates obtained with GOM, and those obtained with third-order KS. Ground reaction forces, consistent with q_{gt} , were input to the joint moment calculation. The calculation of the percentage errors for the joint moments, ε_T , is analogous to the calculation of ε_{pos} . We compared percentage errors for the extreme moments, $\varepsilon_{T \min,j}$ and $\varepsilon_{T \max,j}$, for GOM and KS:

$$\varepsilon_{T \min,j} = 100 \times \frac{|\min(T_j) - \min(T_{gt,j})|}{\max(T_{gt,j}) - \min(T_{gt,j})}$$

$$\varepsilon_{T \max,j} = 100 \times \frac{|\max(T_j) - \max(T_{gt,j})|}{\max(T_{gt,j}) - \min(T_{gt,j})}$$

where T_j and $T_{gt,j}$ are the moments of joint j , calculated based on the estimates and the ground truth, respectively.

4.3.3 Experiment

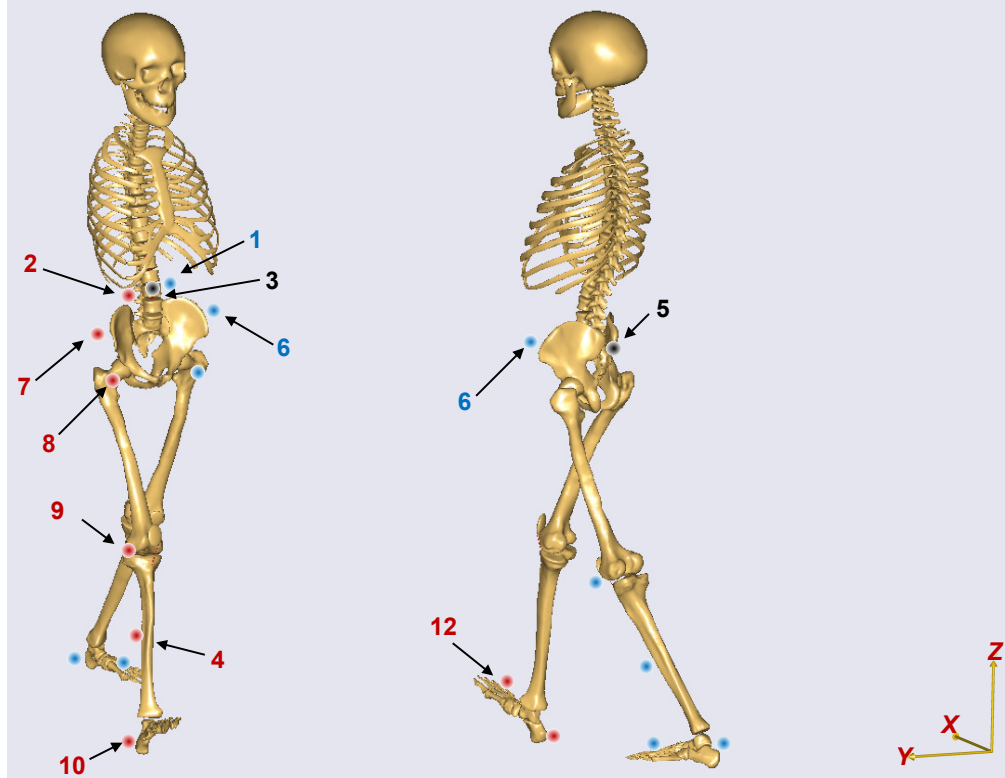


Figure 4.10 – Markers used to capture the motion.

Biomechanical model and marker placement protocol. The biomechanical model consists of ten body segments: a head–trunk segment, the pelvis, left and right thigh, shank, hindfoot and forefoot [Delp and Loan(1990)]. This model includes 21 DOFs. Spherical joints connect the head–trunk segment to the pelvis and the pelvis to the thighs. The ankle and subtalar joints are modelled as simple hinges, whereas the knee joints are modelled as sliding hinges. The remaining six DOFs correspond to the position and orientation of the pelvis. The generic biomechanical model was scaled to the subject's dimensions. A modified Cleveland marker placement protocol was used for the data collection. The marker set consisted of 30 markers, including five clusters of three markers. Three anatomical markers defined the trunk: a marker on the lateral aspects of the left (1) and right (2) shoulder and a marker on the sternum (3). The pelvis segment is defined by a cluster of three technical markers on the sacrum (4a–c) and two anatomical markers on the left (5) and right (6) anterior superior iliac spine (ASIS). The thigh

segment is defined by a cluster of three technical markers (7a–c). The shank segment is defined by a cluster of three technical markers (8a–c), an anatomical marker on the lateral epicondyle (9), and an anatomical marker on the lateral malleolus (10). The foot segment is defined by three anatomical markers on the heel (11), the lateral foot (12) and the first metatarsal head (13). During a static calibration trial, additional anatomical markers were added to the medial femoral condyles and the medial malleoli to define the knee and ankle joint axis

Applied GOM, KF, and KS to experimentally measured marker trajectories. Marker trajectories were measured during gait using a seven camera motion capture system (Qualisys Motion Capture systems). It is difficult to compare estimation errors in this part of the study because no ground truth for the joint kinematics was known. Therefore assumed that improved estimates of the generalized coordinates would better predict the trajectories of validation markers. The trajectories of validation markers are measured but are not used to estimate the generalized coordinates. To validate our method based on this assumption, estimates of the generalized coordinates were calculated from a subset of the measured markers including only one marker on the thigh, while the other two markers on the thigh were used as validation markers. The positions of the validation markers were calculated from the estimates of the generalized coordinates using the biochemical model. Then, the root RMS distance between the measured and calculated positions of the validation markers was used as a measure of the estimation quality.

4.4 Results

Table 4.1 – Marker error, \bar{d}_{RMS} .

\bar{d}_{RMS}	GOM	LME	Kalman filter	$K = 2$	$K = 3$	$K = 4$
without errors	10.27	0.01	0.04	0.01	0.03	0.08
instrumental errors	10.52	0.10	1.45	1.55	1.59	1.58
Soft tissue artefacts	9.57	0.01	3.46	3.46	3.46	3.46
increased thigh length	23.40	-	0.04	-	15.19	-
hip centre dislocation	12.82	-	3.60	-	3.60	-

The smallest marker errors, \bar{d}_{RMS} , were obtained with LME, the largest marker errors were obtained with GOM (table 4.1). KS resulted in a smaller estimation error for the generalized coordinates, ε_{pos} , than GOM, KF, and LME (table 4.2). Compared with GOM and KF respectively, KS ($K = 3$) reduced the estimation error by 97.8% and 59.3% (without errors), 88.1% and 53.0% (instrumental errors), 4.5% and 0.2% (STA), 6.5% and 0.9% (increased thigh length), and 10.8% and 0.1% (hip centre dislocation). Percentage reductions are calculated from the estimation

Table 4.2 – Percentage errors for the estimates of the generalized co-ordinates, ε_{pos}

\bar{d}_{RMS}	GOM	LME	Kalman filter	$K = 2$	$K = 3$	$K = 4$
without errors	4.05	204	0.21	0.03	0.09	0.22
instrumental errors	4.79	585	1.20	0.62	0.57	0.57
Soft tissue artefacts	7.12	541	6.81	6.80	6.80	6.80
increased thigh length	25.69	-	24.23	-	24.02	-
hip centre dislocation	13.01	-	11.61	-	11.60	-

Table 4.3 – Percentage errors for the estimates of the generalized accelerations, ε_{acc}

ε_{pos}	LME	Kalman filter	$K = 2$	$K = 3$	$K = 4$
without errors	25.93	16.10	1.77	2.68	4.01
instrumental errors	100.12	37.50	20.00	7.29	6.46
Soft tissue artefacts	53.21	20.53	9.42	9.57	9.95
increased thigh length	-	42.75	-	18.84	-
hip centre dislocation	-	17.85	-	4.85	-

errors (supplementary material). The errors for the LME position estimates were two to three orders of magnitude larger than the errors with the other techniques.

The effect of the order K of the process model of KS on the estimation errors depended on the errors of the input marker trajectories. A second-order process model outperformed third- and fourth-order process models for marker trajectories without errors. In the presence of instrumental errors, third- and even fourth-order process models produced better estimates than a second-order process model. In the presence of STA, the estimation errors were similar for all three orders (table 4.2).

KS resulted in a smaller estimation error for the generalized accelerations, ε_{acc} , than KF and LME (table 4.3). Compared with KF, KS ($K = 3$) reduced the estimation error by 83.3% (without errors), 80.6% (instrumental errors), 53.4% (STA), 55.9% (increased thigh length), and 72.8% (hip centre dislocation). The KF estimates showed a time lag with respect to the ground truth (figure 4.11). This time lag was larger for higher derivatives of the generalized coordinates and disappeared when smoothing was applied. Compared with LME, KS reduced estimation errors by one to two orders of magnitude. Compared with GOM, KS reduced the estimation error for the joint moments, ε_T , by 87.7% (without errors), 85.1% (instrumental errors), 45.6% (STA), 36.2% (increased thigh length) and 57.4% (hip centre dislocation) (table 4.4, figure 4.12, figure 4.13). KS estimated more accurate extreme joint moments than GOM (figure 4.14).

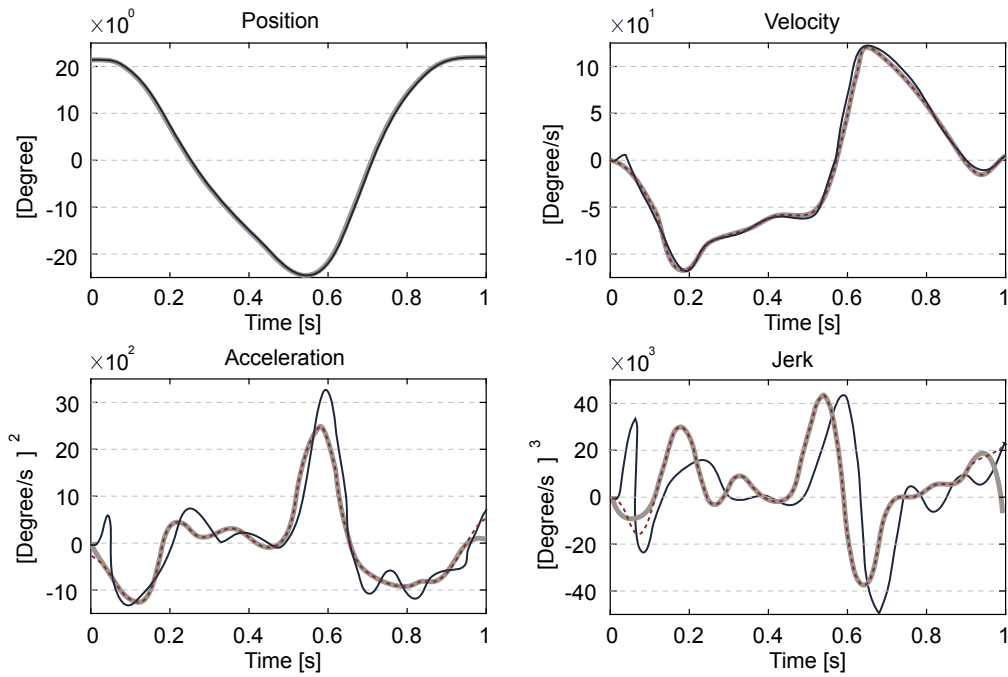


Figure 4.11 – Estimates of angular position, velocity, acceleration and jerk of the right hip flexion as a function of time obtained from the set of marker trajectories without errors with KF (solid black) and smoothing (dashed black). The ground truth (gray) serves as a reference. The filter estimate suffers from a time lag.

4.5 Discussion

Several methods to reduce the sensitivity of inverse kinematics to instrumental errors and STA, have been proposed in the literature: SOM, GOM, KF, and LME. A drawback of these methods is that they only use part of the marker trajectories to estimate the joint kinematics at a considered time instant. We therefore developed a KS algorithm to calculate the estimate at each time instant based on the complete marker trajectories. To assess whether KS improves estimates of joint kinematics and kinetics, we compared this technique with GOM, KF, and LME. We did not include SOM in our study, since GOM and LME have already been shown to

Table 4.4 – Percentage errors for the joint moments, ε_T .

ε_T	GOM	$K = 3$
without errors	12.17	1.50
instrumental errors	12.24	1.82
Soft tissue artefacts	12.23	6.65
increased thigh length	14.19	9.06
hip centre dislocation	13.43	5.72

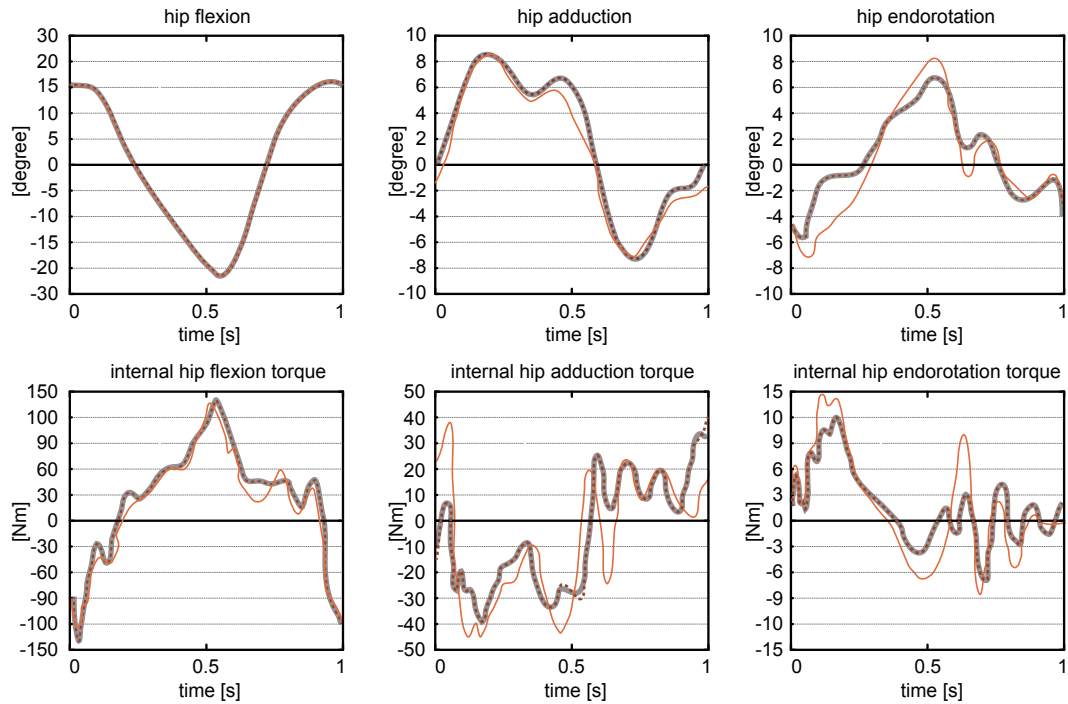


Figure 4.12 – Estimates of angular positions and internal joint moments with instrumental errors. GOM are represented by a solid line, estimates obtained with third-order KS are represented by a dashed line. The ground truth (gray) serves as a reference.

outperform SOM [Cerveri and Pedotti(2005)], [Lu and O'Connor(1999)].

KS resulted in better estimates of the generalized coordinates calculated from simulated marker trajectories than GOM, KF, and LME. Furthermore, KF outperformed GOM in terms of estimation errors (table 4.2 and table 4.3). The smaller estimation errors using KF and smoothing compared to GOM confirm our assumption that inverse kinematics benefits from integrating prior knowledge on motion smoothness.

Although GOM narrowly focuses on minimising marker error at a given time instant, KF and KS outperform GOM in the reduction of marker error (table 4.2). In the absence of measurement and modelling errors (validation in simulation with the marker trajectories without errors), a perfect fit between the measurements and the biomechanical model exists. Nevertheless, the obtained marker error for the GOM estimate is 10.27mm, showing that GOM does not return the global optimum. It is a wellknown problem that solvers for nonlinear optimisation problems find a locally optimal solution depending on the initial values of the optimisation variables. Since in this study the initial values at the first time instant were equal for all methods, this shows that KF and KS are more suitable to solve this problem.

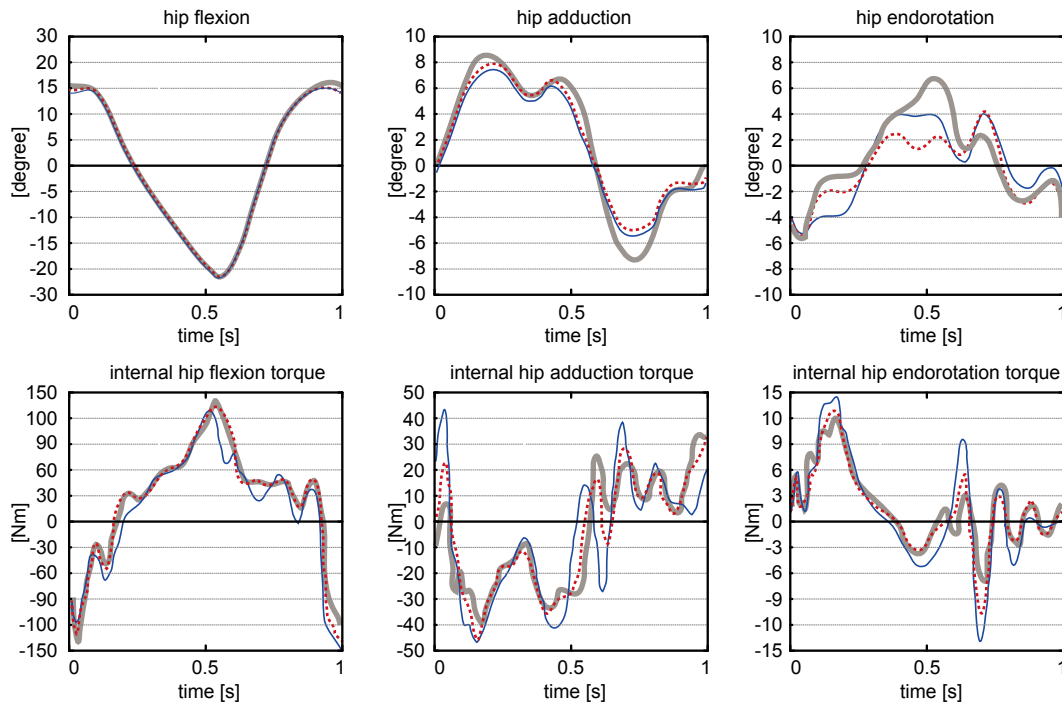


Figure 4.13 – Estimates of angular positions and internal joint moments with STA. GOM are represented by a solid line, estimates obtained with third-order KS are represented by a dashed line. The ground truth (gray) serves as a reference.

Results (table 4.2 and table 4.3) show that LME is not suitable to cope with STA of the full marker set during gait. Estimating all 15 local marker positions, velocities, and accelerations leads to a huge number of variables in the underlying Kalman filter. Compared to the simulation study of [Cerveri and Pedotti(2005)], the joint range of motion during gait and therefore the information contained in the marker positions is limited. Since this information is insufficient to correctly estimate all local marker positions, the estimated joint kinematics diverge from the ground truth, although LME outperforms all other methods in terms of marker error (table 4.1).

In the presence of instrumental errors, a third or fourth-order process model outperformed a second-order process model for the Kalman smoother.

4.6 Summary

1. This chapter addressed the effect of KF and KS on the accuracy of the estimated accelerations. While the Kalman smoother estimates of the generalized co-ordinates were twice as accurate (without errors, instrumental errors) or as accurate (STA, modelling errors)

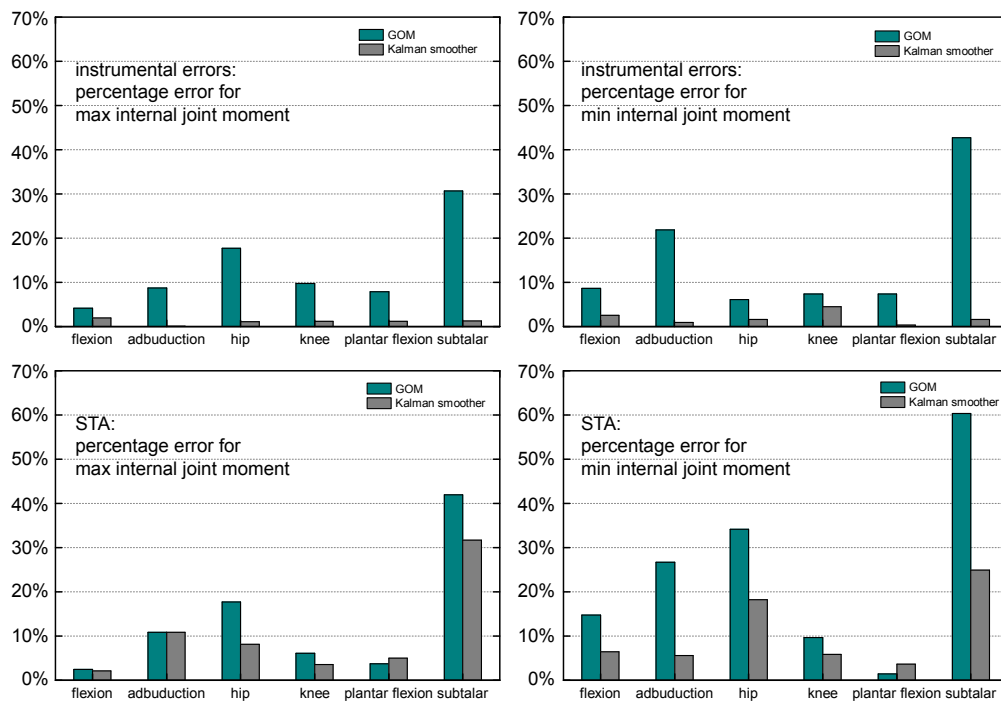


Figure 4.14 – Percentage errors for the minimum and maximum internal joint moments using the GOM and KS.

as the corresponding Kalman filter estimates, the Kalman smoother estimates of the generalized accelerations were respectively about five times (without errors, instrumental errors) and about two times (STA, modelling errors) better than the corresponding Kalman filter estimates.

2. The inferior acceleration estimates of KF were due to the filter lag caused by the asymmetrical use of data in time. The backward recursion added by the Kalman smoother not only improves the velocity and acceleration estimates but, through the process model, also consistently improves the position estimates.
3. Using KS instead of GOM greatly improved the estimation of joint moments and consequently the assessment of maximum joint loading from peak moments even when STA or modelling errors were present and the reduction of the estimation errors for the positions was rather limited. The inferior joint moment estimation of GOM results from the numerical differentiation of the nonsmooth positions.

5 A Golf Swing Robot to Simulate Natural Release

5.1 Introduction

Golf swing is a complicated motion assembled by moving many parts of human body. The dynamics of swing motion have been studied for many years in an effort to improve the performance of golf clubs and to optimize the performance of golf players. As mentioned in previous chapters, a double-link model is often used. Concerning the skill of motion control in human swing, many works have been done in the fields of biomechanics and sport. Among those works, the most popular explanation about the skill is given by [Jorgensen(1999)].

The study presented in the chapter 3 provided an insight into the mechanism of the release point of the golf swing and the effect of the acceleration patterns of the down swing on the dynamic behavior at the release point base on a double pendulum model. It was found that acceleration patterns which has positive gradient gives high angular velocity of the release point and later release point, and negative gradient pattern shows low angular velocity and earlier release point.

Usually, golf swing robots are used to test golf clubs and golf balls for conformity to standards instead of professional golfers because their ability to deliver quantitative and consistent swing. Furthermore, some golf swing robots are invented to perform specific dynamic motions by many researchers. [Ming and Kajitani(2003b)] developed a golf swing robotic to simulate motion control skill in high speed condition. [Suzuki and Inooka(1997)] investigated variation of swing velocity with different specific characteristics of golf clubs based on a similar golf swing robot. This robot had a passive wrist joint and could utilize the coupling force generated by its swing motion and shaft vibration like human being. With the consideration that a wrist release naturally delayed during down swing. [Suzuki and Haake(2006)] developed

a multiple modulation torque planning method for the robot to improve swing efficiency. [Hoshino et al.(2005)Hoshino, Kobayashi, and Yamada] utilized a state observer to suppress vibration of their optimal control golf swing robot. Additionally, [Chaochao and Yoshio(2007)] proposed an impedance control strategy for their golf swing robot to emulate different arm mass golfers. They also proved that a properly wrist action with consideration of the golf ball position could improve the horizontal club head speed at impact.

This chapter will extend Jorgensen's explanation on the light of the view how to realize golf swing from engineering, and defined the skill of motion control as multi-steps acceleration by dynamic coupling drive. Different to the several developed golf swing robots [Arai and Tachi(1991)], a new mechanism and control method of golf swing robot is proposed to simulate natural release of motion control and developed a small prototype of golf swing robot. The developed robot consists of one actuated joint and one passive joint with mechanical stopper.

5.2 Structure of the Prototype

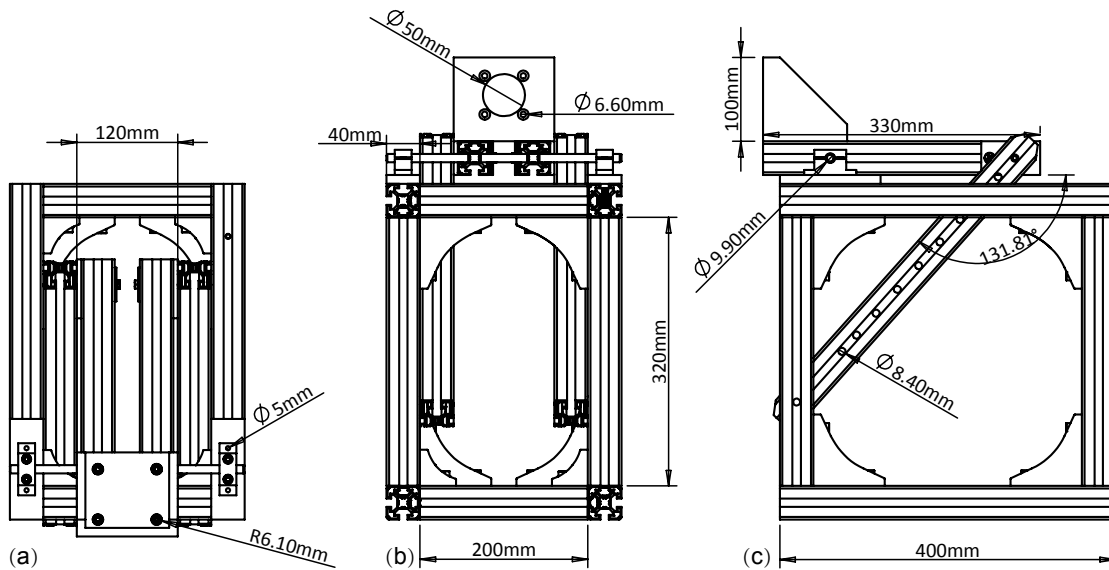


Figure 5.1 – Three view diagram of supporting frame. (a)top view; (b)front view; (c)lateral view. Swing plane $\phi = 90^\circ$

With regard to the above golf swing robots, most researchers took their interests in utilizing a robot to evaluate performance of golf clubs. Usually, they adopted predefined joint torque patterns in motion control. Despite such kinds of torque patterns simplify golf swing planning, they lead to low robot dynamic performance. Generally, there are differences between the

traditional golf swing robots and golf players. Human beings have a dexterous upper body structure: the wrist joint is lighter and less powerful than the elbow joint, which in turn is lighter and less powerful than the shoulder joint, and so on. However, when performing dynamic manipulation, human beings can transfer the power from a heavier and stronger part of the body, e.g. the torso, to the shoulder joint, then to the elbow joint and wrist joint so as to improve their dynamic performance.

To validate this inspiration, a new two link golf swing robot has been developed. The swing prototype consists two major parts: frame (figure 5.1) and two degree freedom manipulator. The frame is mainly used to support manipulator complete swing action at the bottom. Another effect of frame is to change swing plane, background to 10 degree for units, from 0 to 90 degree through changing different locating holes ($\phi = 8.40 \text{ mm}$), as shown in figure 5.1.c.

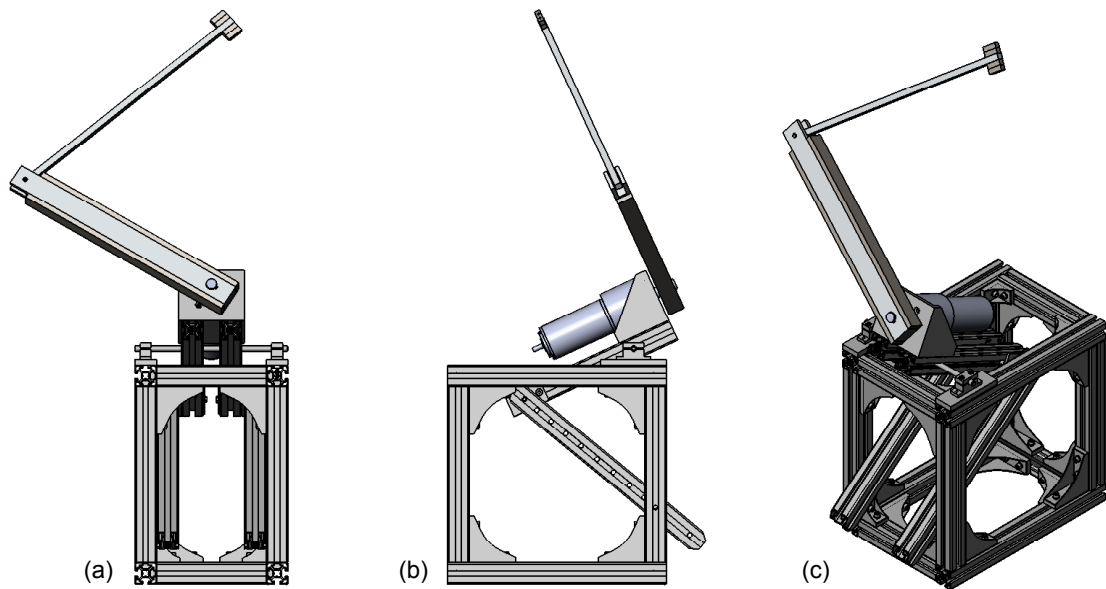


Figure 5.2 – Prototype of golf swing robot. (a)front view; (b)lateral view; (c)isometric view. Swing plane $\phi = 80^\circ$.

Table 5.1 – Parameters of the swing prototype.

Parameter	Symbol	Value
Mass of arm (kg)	m_1	1.50
Length of arm (m)	L_1	6.65
Location of centroid of arm (m)	R_1	9.06
Mass of club (kg)	m_2	5.72
Length of club (m)	L_2	1.0
Location of centroid of club (m)	R_2	1.0

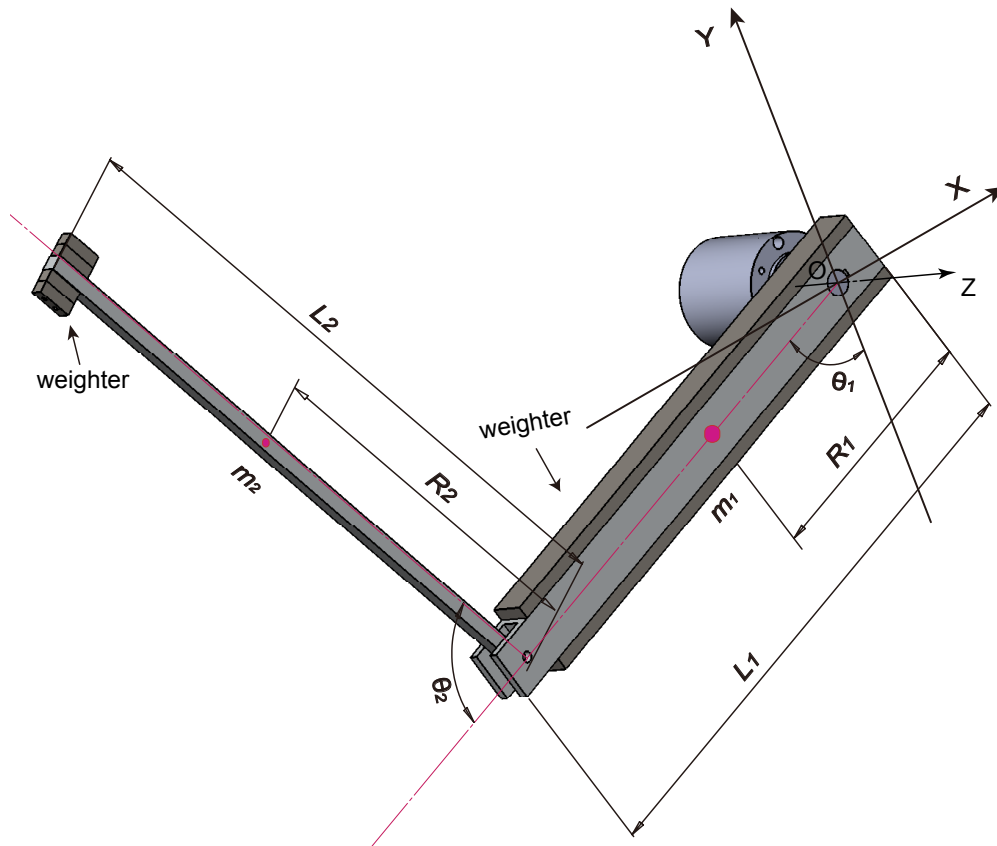


Figure 5.3 – Manipulator part of swing prototype.

Table 5.2 – Parameters of the DC motor and gear head.

DC motor	Value	Gear head	Value
Type	RE65	Type	GP81
Peak torque (mNm)	628	Reduction	51 : 1
Stop torque (mNm)	18000	Max. continuous torque (Nm)	120
Rated power (W)	250	Max. intermittent torque (Nm)	180
Maximum speed (rpm)	3850	Mass inertia (gcm^2)	88
Mass (g)	2100	Mass (g)	3700
Encoder	HEDS5540	Length (mm)	135.3

About manipulator, the first joint is a active joint with an DC motor, and the second joint is a passive joint that has a holding brake instead of an actuator. As shown in figure 5.3, the lengths of both link 1 and link 2 are 400 mm and 500 mm, respectively, and two red dots represent center of gravity. The mass distribution of both links are adjusted by adding weighter to both sides. The actuator of the link 1 (active joint) is a 250 W DC motor with a 51/1 harmonic drive motor gear. The torque of DC motor is controlled by motor current. The motion controller

then is required to perform the high-speed dynamic manipulation utilizing the torque/power transfer from the shoulder joint to the wrist joint, just like that in human beings. A PWM current amplifier is used. An optical encoder is used to detect the angle of link 1. The encoder of the active joint is $200000P/R$ which located at the input shaft of the DC motor. The angle of link 2 is determined by a reflective marker. Table 5.1 gives the link parameters of the robot and Table 5.2 gives the specifications of the DC motor and encoder.

5.3 Material and Methods

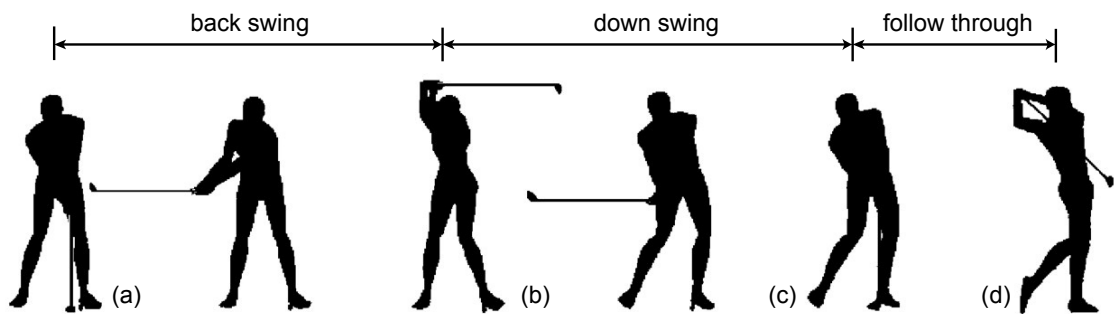


Figure 5.4 – Key moments and phases of the golf swing. (a)address; (b)top; (c)impact; (d)finish.

As definition of gait phase is widely used in gait research, swing movement is also used to be divided into several different phases which would be helpful to better understand what happened inside the body throughout the swing process [Keogh et al.(2005)Keogh, Reid, et al.]. During golfing, the most commonly used phases are the backswing, the downswing and the follow through. Moreover, a clear definition of the key points that separate these phases: the address, top, impact and finish. The phases and moments are visualized in figure 1.

5.3.1 Swing motion capture based on the optical system

As shown in figure 5.3, the joint between link 1 and link 2 represents wrists of human being. Compare to shoulder joint, it is much less powerful. In order to investigate natural release during downswing, we adopted a method which different to other golf swing robot when assembled the swing prototype. The link 2 is mated to the hinge block of link 1 by inserting a hinge pin at the wrist joint.

On the one side, it is helpful to realize natural uncocking, because with the rotation of should joint (250W DC motor), the wrist of swing prototype will begin to turn freely at the moment that the sum of the moments applied to the wrist joint becomes to zero. However, on the other side, it is difficult to measure motion parameters, such as angular velocity, angular acceleration

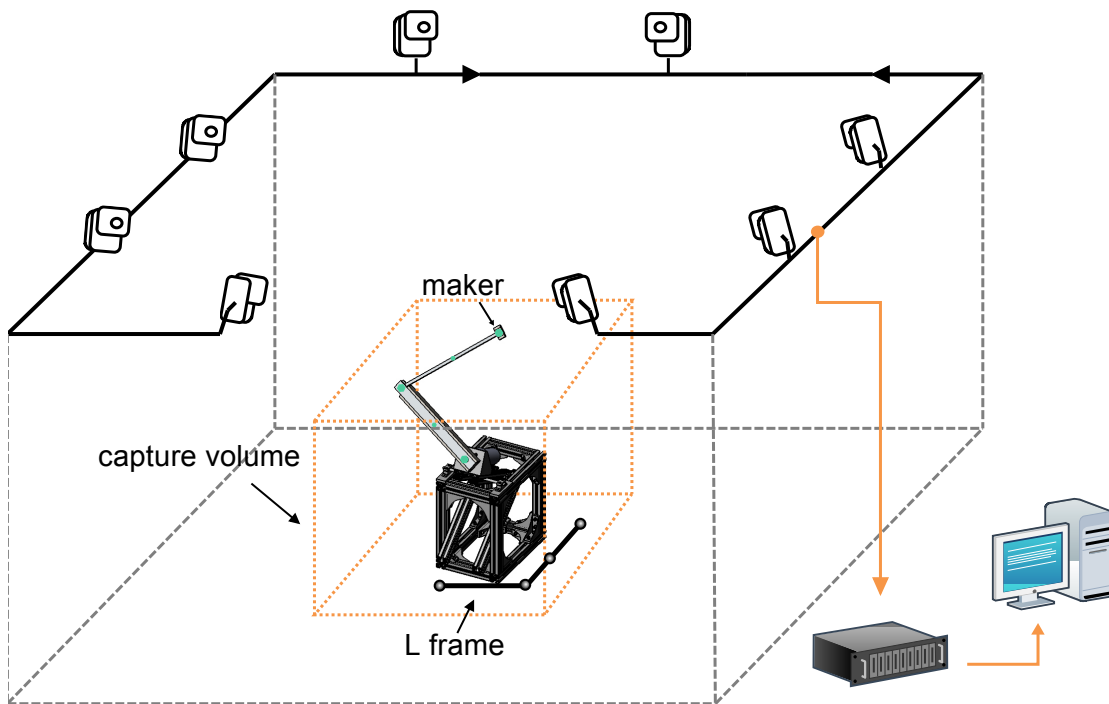


Figure 5.5 – Placing swing prototype in the capture volume

and angular displacement. Addressing this problem, a optical motion capture system is used to track swing trajectory from the beginning to the end of follow through. A set of markers (green dots) are attached to the joints and gravity centers of swing prototype, as shown in figure 5.5. Compare to human being, it is unnecessary to consider noise brought on by the soft tissue artefacts [Benoit and Ramsey(2006)] or missing marker visibility caused by a body part blocked marker from recording. Furthermore, optical motion capture system can be used as a reference system, of which results are compared to results derived by motor control system.

Table 5.3 – Parameters of the swing prototype.

	marker size (mm)	capture volume (m)
Max accuracy	<i>Raptor/Eagle</i> = 9	2.5×2.5
large volume	<i>Raptor/Eagle</i> = 12.5	3.5×3.5
extended volume	<i>Raptor/Eagle</i> = 19	5×5

It should be noticed that, system calibrating process is a necessary step before starting measurement, in order to extract metric information form swing process. The software we used is *Cortex* (Motion Analysis Corp.),

1. Set marker of the calibration L-frame at the desired origin of the capture volume.

2. The four-point square which determines the global axes and the orientation of the volume displayed in Cortex should be rotated so as many control points as possible can be seen by all cameras.
3. Adjust the position of L-frame until it is can be seen by at least half cameras to give a good calibration. The other half of the cameras can be calibrated using the wand. You may need to adjust the cameras at this point.
4. Listed in table 5.3 are optimal and highest accuracy, large volume, and extended volume capture areas for the 6 camera systems used in our experiment. At the extremes, volumes will vary with ceiling heights and can vary with optical conditions including external lighting.

5.3.2 Principle of motion control

The idea of a swing plane apparently originated when Ben Hogan introduced the idea of a plane of glass extending from the ball to his shoulders [Hogan(1985)] in the late 1950s. As shown in figure 5.6, the entire swing motion is assumed to be conducted in one plane. The assumption of the planar movement of the arm and golf club is well supported in the early research [Cochran and Stobbs(1968)] and [Jorgensen(1999)]. The swing plane is defined by Cartesian coordinates $O - XYZ$, refer to figure 5.2. The swing plane is inclined at an angle ϕ to $O - XZ$ plane.

dynamic equations of motion

Generally, a great deal of factor are to relevant angle ϕ , such as golf player's swing habit, type of club, and physique. The club, arm, and grip-holding fingers are regarded as independent rigid rods. The should joint, in this research, rotates around the origin O of the coordinate system fixed on swing plane $O - XY$. Therefore, the dynamic equations of swing prototype can be expressed as:

$$\tau = M\ddot{\theta} + N(\theta, \dot{\theta}) \quad (5.1)$$

where, $\tau = [\tau_1, \tau_2]^T$ represents the joint torque. More specific, the torque τ_1 is employed at the shoulder joint to drive the swing. the torque τ_2 is applied at wrist joint to grip the club. $\theta = [\theta_1, \theta_2]^T$ represents the generalized coordinate. M represents the inertia matrix, $N = [N_1, N_2]^T$ is the combination due to centripetal force, centrifugal force, and gravity.

In many studies which address nonlinear system control, assumption of input and output

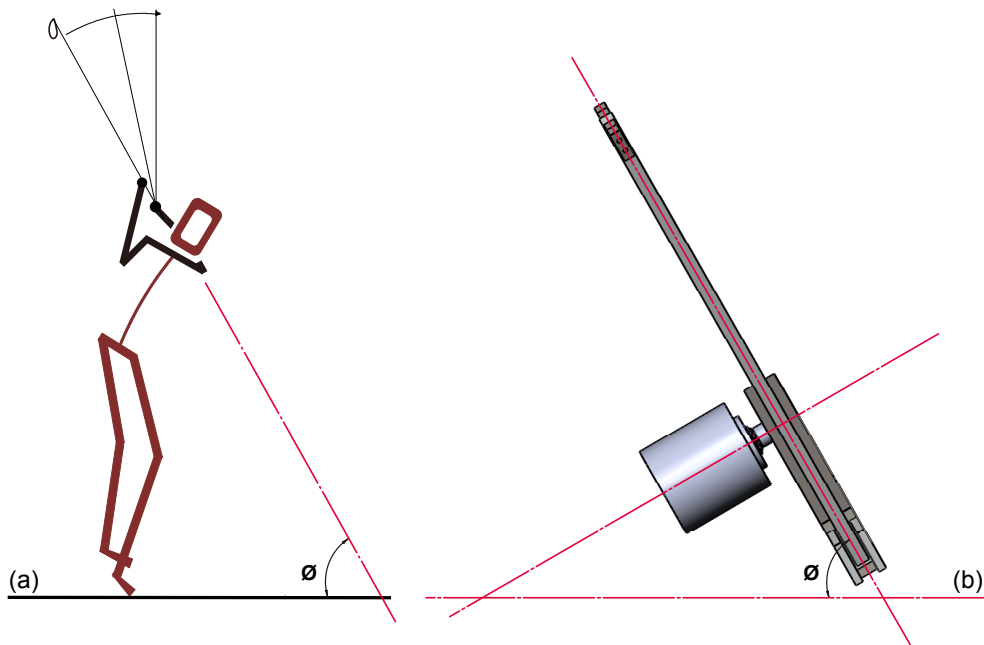


Figure 5.6 – Lateral view of the swing plane. (a)lateral view of a golf player; (b)lateral view of the swing manipulator.

of system are linearization is versatile adopted. It helps converting original system into a linear one by using nonlinear coordinates. After transformation, the system can be forced to possess the properties of a decided target dynamic system. Therefore, the control task is also transferred to control reference motion based on a suitable target dynamical system [Nakanishi et al.(2000)Nakanishi, Fukuda, and Koditschek].

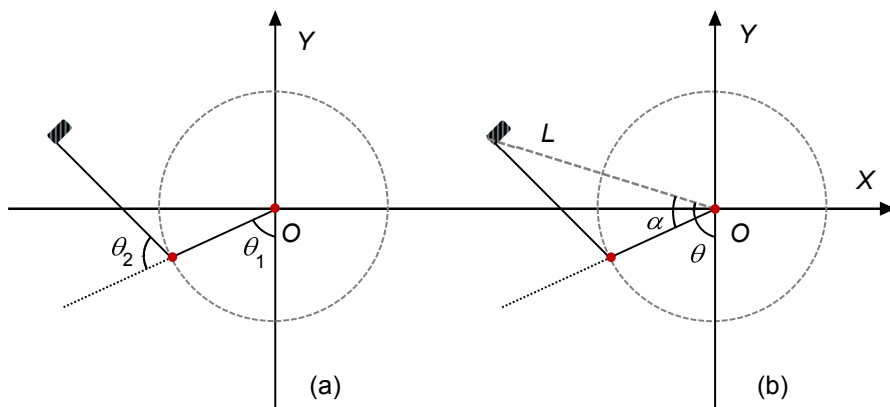


Figure 5.7 – Coordinates transformation.

According to figure 5.7, θ_1 and θ_2 are generalized coordinate of link1 and link2. L is the length of the pseudo link from shoulder joint to club head. α is the angular between pseudo link and

link1. θ is the angular between pseudo link and Y – axis. After coordinates transformation, angular θ and its derivative are served as output of control system. Therefore, rewrite dynamic equation 5.1 in state space to:

$$\dot{x} = F(x, \tau) = \begin{bmatrix} \dot{\theta}_1 \\ \dot{\theta}_2 \\ M^{-1}(-N(x) + \tau) \end{bmatrix} \quad (5.2)$$

where, $x = [\theta_1, \theta_2, \dot{\theta}_1, \dot{\theta}_2]^T$ is the state variable. The output function y of system is described as:

$$y = H(x) = \begin{bmatrix} \theta \\ \dot{\theta} \end{bmatrix} = \begin{bmatrix} \theta_1 + \alpha \\ \dot{\theta}_1 + \frac{L_1(L_2 + L_1 \cos \theta_2)}{L_1^2 + L_2^2 + 2L_1 L_2 \cos \theta_2} \dot{\theta}_2 \end{bmatrix} \quad (5.3)$$

Define a harmonic oscillator:

$$\dot{y} = \begin{bmatrix} \theta \\ \dot{\theta} \end{bmatrix}' = \begin{bmatrix} 0 & 1 \\ -\omega^2 & 0 \end{bmatrix} \begin{bmatrix} \theta \\ \dot{\theta} \end{bmatrix} \quad (5.4)$$

Define equation 5.4 as the target dynamical system of the prototype. The output (equation 5.3) will be driven by control law [Nakanishi et al.(2000)Nakanishi, Fukuda, and Koditschek] to track the trajectory of defined target system. However, considering that the target dynamical system (equation 5.4) is an energy conservation system. It means energy generated by shoulder joint should be big enough to force release condition discussed in chapter 2 be satisfied before club arrived at impact position. Therefore, rewrite equation 5.4 to a more specific expression:

$$\dot{y} = \begin{bmatrix} \theta \\ \dot{\theta} \end{bmatrix}' = \begin{bmatrix} 0 & 1 \\ -\omega^2 & -K_e(E - E^*) \end{bmatrix} \begin{bmatrix} \theta \\ \dot{\theta} \end{bmatrix} \quad (5.5)$$

where, K_e is a positive constant. E^* is the theoretical pseudo energy corresponding to the specific release condition. $E = (1/2)\dot{\theta}^2 + (1/2)\omega^2\theta^2$ is the pseudo energy of target system.

Simplified equation 5.5:

$$\ddot{\theta} + K_e(E - E^*)\dot{\theta} + \omega^2\theta = 0 \quad (5.6)$$

where, if $E^* > E$, the generated energy will accelerate oscillator (equation 5.4) to increase energy E . If $E^* < E$, the generated energy will accelerate oscillator (equation 5.4) to decrease

energy E . At last, E will eventually transfer to E^* and oscillator will finally reach to a equilibrium status defined by:

$$\ddot{\theta} + \omega^2 \theta = 0 \quad (5.7)$$

Because at the bottom of the swing the golf club (link2) is almost perfectly parallel to arms link1, therefore $\theta_1 = \theta_2 = 0$ at the impact position, the speed along with X -direction can be expressed as:

$$v_x = \dot{\theta}_1 L_1 + (\dot{\theta}_1 + \dot{\theta}_2) L_2 \quad (5.8)$$

According to equation 5.3, if $\theta_2 = 0$, then rewrite parameter $\dot{\theta}$:

$$\dot{\theta} = \dot{\theta}_1 + \frac{L_1}{L_1 + L_2} \dot{\theta}_2 \quad (5.9)$$

Use the identity, the equation 5.8 becomes:

$$\frac{v_x}{L_1 + L_2} = \frac{\dot{\theta}_1 L_1}{L_1 + L_2} + \frac{(\dot{\theta}_1 + \dot{\theta}_2) L_2}{L_1 + L_2} = \dot{\theta}_1 + \frac{L_1}{L_1 + L_2} \dot{\theta}_2$$

Therefore, the equation 5.9 becomes:

$$\dot{\theta} = \frac{v_x}{L_1 + L_2} \quad (5.10)$$

The desired pseudo energy level at the impact position, where angle $\theta = 0$ is rewrote as:

$$E^* = \frac{v_x^2}{2(L_1 + L_2)^2} \quad (5.11)$$

The above equation indicates that the pseudo energy is uniquely determined by the speed v_x at the impact position. Hence the specified v_x can be achieved by controlling the energy consumption of the swing prototype. Then substitute equation 5.2, equation 5.3, and equation 5.5 into control law:

$$a_1 \tau_1 + a_2 \tau_2 = -\omega^2 \theta - K_e (E - E^*) \dot{\theta} + a_1 N_1 + a_2 N_2 + a_3 \quad (5.12)$$

where,

$$a_1 = n_{11} + \frac{L_2 (L_2 + L_1 \cos \theta_2)}{L_1^2 + L_2^2 + 2L_1 L_2 \cos \theta_2} n_{21}$$

$$a_2 = n_{12} + \frac{L_2 (L_2 + L_1 \cos \theta_2)}{L_1^2 + L_2^2 + 2L_1 L_2 \cos \theta_2} n_{22}$$

$$a_3 = \frac{(L_1^2 - L_2^2) L_1 L_2 \sin \theta_2 \dot{\theta}_2^2}{(L_1^2 + L_2^2 + 2L_1 L_2 \cos \theta_2)^2}$$

The equation 5.12 describe the relationship between inputs (τ_1, τ_2) and energy level of system. Based on the Port-controlled Hamilton system [De Luca and Oriolo(2002)]. Rewrite torque τ_1 as:

$$\tau_1 = K_h (E - E^*) (\dot{\theta}_1 - \dot{\theta}_2) \quad (5.13)$$

where, K_h is the parameter need to be determined before manipulation.

Substitute equation 5.13 to equation 5.12, torque τ_2 can be expressed as:

$$\tau_2 = \frac{a_1 N_1 + a_2 N_2 + a_3}{a_2} - \frac{\omega^2 \theta + [K_e \dot{\theta} + a_1 K_h (\dot{\theta}_1 - \dot{\theta}_2)] (E - E^*)}{a_2} \quad (5.14)$$

motion control for stopping

Because the energy controller cannot stop the swing, it is necessary to adopt another control method to stop swing motion like follow through process of real golf swing. As shown in figure 5.7, angular displacement θ is used as a sign. If $\theta \leq 0$, the swing prototype is controlled by energy strategy. Otherwise, control method switch to proportional plus gravity and coupling torque compensation. After the swing passed through the impact position and entered the follow through phase, swing prototype should be smoothly slowed down then stopped.

Dynamic motion equation of swing prototype is described by equation 5.1, rewrite the form of τ_2 based on equation 5.1:

$$\tau_1 - \tau_2 + \tau_{1c} = I_{\eta 1} \ddot{\eta}_1 + M_{\eta 1} L_{g1} g_y \sin \eta_1 \quad (5.15)$$

$$\tau_2 + \tau_{1c} = I_{\eta 2} \ddot{\eta}_2 + M_{\eta 2} L_{g2} g_y \sin \eta_2$$

where, $\eta_1 = \theta_1$, $\eta_2 = \theta_1 + \theta_2$, τ_{1c} represents the coupling torque exerted on the shoulder joint, τ_{2c} represents the coupling torque exerted on the wrist joint.

Equation 5.15 is the motion of link1 and link2 with moment of inertia I_{η_1} and I_{η_2} and both mass M_{η_1} and M_{η_2} driven by the joint torques $\tau_1 - \tau_2$, τ_2 and the coupling torque τ_{1c} , τ_{2c} , respectively. According to this, the double-link golf swing prototype can be regarded as a dynamic system consisting of two single rods connected to each other. The motion of system is equivalent to the compound motion of the two single rods. Based on this perception, it is only need to consider the how to brake the single pendulum. A normalized single pendulum can be expressed as:

$$\ddot{\theta} + \sin\theta + K_d\dot{\theta} = u \quad (5.16)$$

where, K_d is a positive damping constant, u is the control input. As discussed in some research works [Åström and Furuta(2000)], the proportional plus gravity compensation can stabilize the pendulum at the equilibrium position. Apply the compensation algorithm to inputs of system:

$$\begin{aligned} \tau_1 = & -\tau_{2c} + M_{\eta_2}L_{g2}g_y \sin\eta_2 - K_{d2}\dot{\eta}_2 - K_{p2}(\eta_2 - \eta_{2f}) \\ & -\tau_{1c} + M_{\eta_1}L_{g1}g_y \sin\eta_1 - K_{d1}\dot{\eta}_1 - K_{p1}(\eta_1 - \eta_{1f}) \end{aligned} \quad (5.17)$$

$$\tau_2 = -\tau_{2c} + M_{\eta_2}L_{g2}g_y \sin\eta_2 - K_{d2}\dot{\eta}_2 - K_{p2}(\eta_2 - \eta_{2f})$$

where, η_{1f} and η_{2f} are desired finish positions, K_{p1} , K_{p2} , K_{d1} , K_{d2} , are relevant parameters.

5.3.3 Realization of motion control

The swing prototype is controlled by an note PC which is connected with an servo controller (*ESCON70/10* by Maxon Motor Co. refer to table 5.4) and an encoder (*HEDS-5540* by Maxon Motor Co.).

As shown in figure 5.8, the control program first reads the motor encoder information from the servo controller to calculate the angles, angular velocities, and angular accelerations of shoulder joint. Then it computes the joint torques according to the control law, converts the torque values into control voltage values, and sends them to the motor driver via the servo controller. Finally the driver output the voltage to drive the DC motor.

Table 5.4 – Parameters of servo controller.

Controller	Value
$+V_{CC\ min}/+V_{CC\ max}$ (VDC)	8 ~ 76
I_{cont}/I_{max} (A)	10/30
PWM frequency (kHz)	53.6
Encoder signals	A, A\, B, B\
Dimensions ($L \times W \times H$ mm)	125×78.5×27

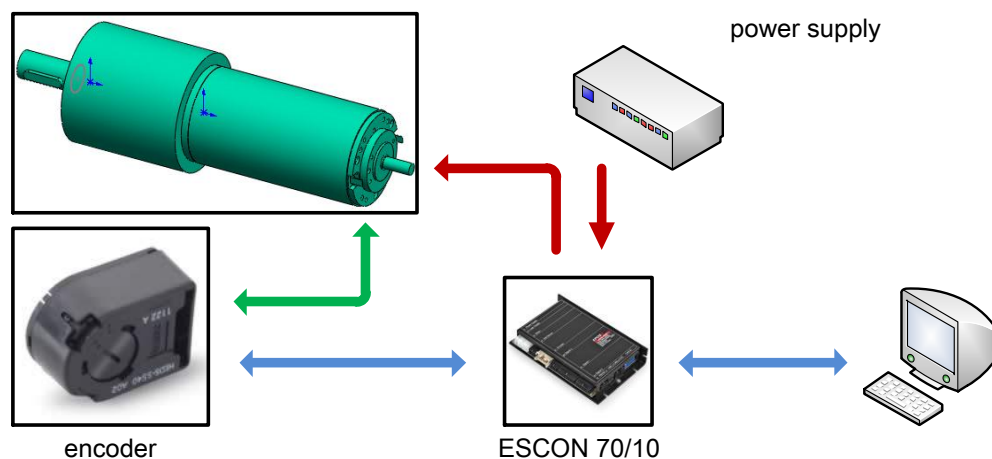


Figure 5.8 – Control architecture. Red arrow represents the direction of current-flow;

5.4 Results

5.4.1 Simulation

Figure 5.10 shows the resulting movement of the robot. Figure 5.9.(a) shows the postures during the downswing phase and figure 5.9.(b) shows the postures during the follow-through phase. From the figure, it demonstrates the prototype passed through the impact position precisely.

By adopting equation 5.13 and equation 5.14 as the controller before impact. Equation 5.16 served as the controller after passing through impact position, respectively. Swing motion can be implemented on this prototype. For example, simulation results with a head speed of 25 m/s at impact position are studied here.

The desired energy level corresponding to the hitting speed of 25 m/s is $E^* = 240$ J, the finish positions are $\theta_{1f} = 215^\circ$ ($\eta_{1f} = 215^\circ$) and $\theta_{2f} = 125^\circ$ ($\eta_{2f} = \theta_{1f} + \theta_{2f} = 340^\circ$), the simulation period is $t_f = 2.5$ s, and the parameters of the two controllers are: $\omega = 4.6862$ rad/s, $K_e =$

0.04275, $K_h = 0.44152$, $K_{p1} = 11.8511$, $K_{d1} = 3.148$, $K_{p2} = 1.146$, $K_{d2} = 4.8353$. In addition, the initial angular velocity of the wrist joint used to break balance is $\dot{\theta}_{2initial} = -0.01 \text{ rad/s}$. Figure 5.10 shows the simulation results.

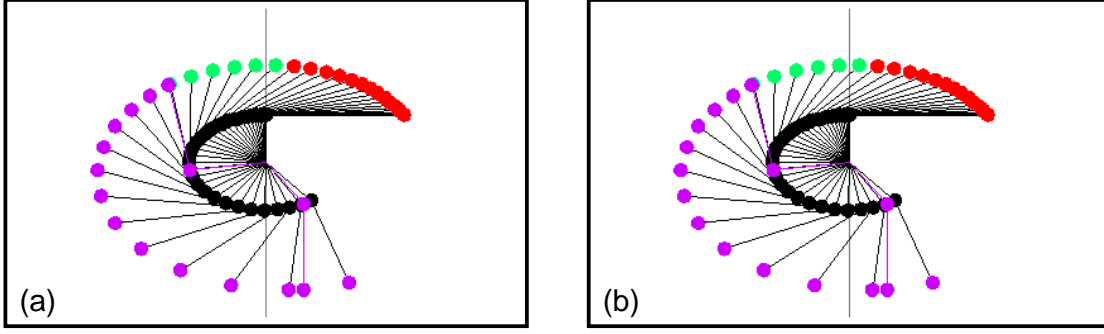


Figure 5.9 – Swing phase of prototype.

Figure 5.10.(a) shows the angle trajectories of the shoulder joint and the wrist joint. As shown in the figure, it can be found that the prototype successfully arrived at specified finish position.

Figure 5.10.(b) shows the drive power history. It can be seen that the power level achieved at the impact position ($t_m = 0.423 \text{ s}$) is about 237.24 J . This value is very close to the drive power level.

Figure 5.10.(c) shows the input torques. It can be found from the figure that the peak value of τ_2 achieved maximum value 11 Nm during the downswing, because the torque of the shoulder joint is transferred to the wrist joint according to equation 5.13 and equation 5.14, which resulted in a high peak reaching approximately 74 Nm in the control input of the shoulder joint.

The relationship of angular velocities (the shoulder joint and the wrist joint) and time are as shown in figure 5.10.(d). It can be found that after passing through impact position, arm link and club link were slowed down and gradually braked. During downswing, an obvious phenomenon was found that firstly, the arm link was accelerated, then club link was accelerated at the starting position of the downswing. However, before impacting, the arm link was decelerated and the club link kept accelerating until achieved maximum speed. The reason is because the employment of dynamic coupling in the high speed swing.

Figure 5.10.(f) shows the club head speed along with X - and Y -axis directions (refer to figure 5.3). The obtained impact speed at the impact position is about 24.78 m/s , which proves the efficiency of the energy control method.

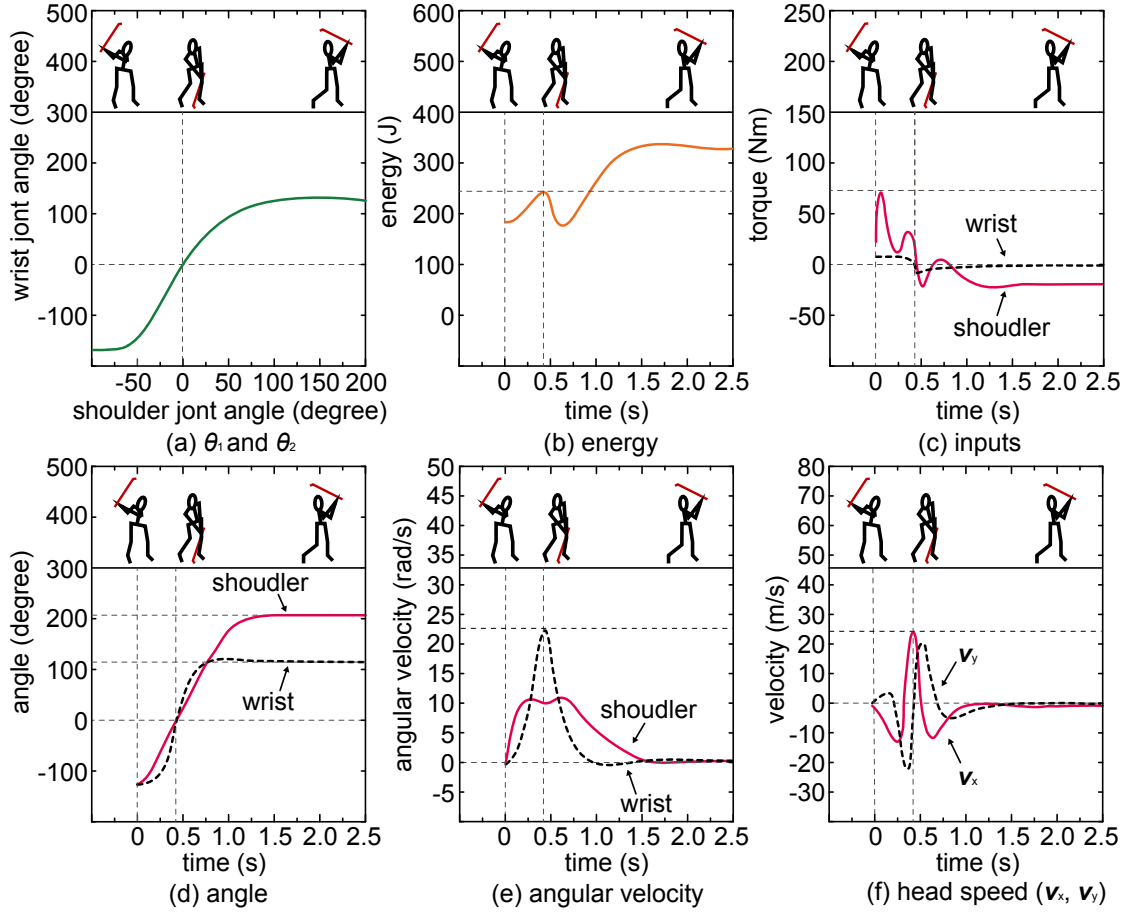


Figure 5.10 – Simulation results of the golf swing with a impacting speed of 24.78 m/s.

The relation between θ_1 and θ_2 is shown in figure 5.10 f. The solid line represents the backswing phase, the dashed line represents the backswing phase, and the dashdot line represents the follow-through phase. From the figure, we can know the robot passed through the impact position accurately because $\theta_1 = \theta_2 = 0.02^\circ$ at the same time.

5.4.2 Experiment

To validate the aforementioned simulation results, experiments are carried out with the golf swing robot and the results are shown in figure 5.11 and figure 5.12. The finish positions of the shoulder joint and the wrist joint are $\theta_1(t_f) = 213.2^\circ$ and $\theta_2(t_f) = 116.61^\circ$, the impact positions are $\theta_1(t_m) = -1.17^\circ$ and $\theta_2(t_m) = 0.64^\circ$, the hitting speed at the impact position is $v_x(t_m) = 22.47$ m/s, and the hitting time is $t_m = 0.43$ s.

As shown in figure 5.12.(b), it found that some spikes occurred in the angular velocity of the

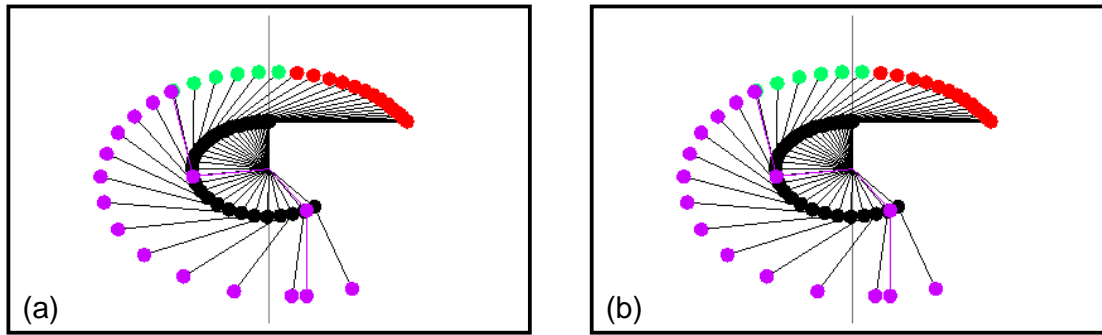


Figure 5.11 – Swing phase of prototype.

wrist joint. It because of vibration of the club link during swing. Especially, at the impact position there is a larger minus transient variation in the angular velocity trajectories of both the shoulder joint and the wrist joint. This is because the controller switched from driving to braking, in the experiment resulting in an instantaneous decrease of the angular velocities. Such angular velocity variation also leads to a joint torque spike as shown in figure 5.12.(c). Likewise, in figure 5.12.(f), the head speed along with X -axis direction has a obvious decrease at the impact position. Figure 5.12.(c) described the input torques. The torque of the shoulder joint looks noisy. And the angular velocity of the shoulder joint is also slightly noisy, the reason is that the noise generated because of some nonlinear properties in the shoulder joint.

The impact position shown in figure 5.11 is slightly different from that shown in figure 5.9. Though the wrist joint delayed behind the shoulder joint about 30° when the arm link arrived at impact position ($\theta_1 = 0$), the accuracy of impact position control is acceptable to the golf swing.

Figure 5.12.(d) and (e) shows the angle trajectory error between simulation and experiment. It is found that there was about 30° constant error in the second half after impact position, which might indicated there was unmodeled static frictional force in the shoulder joint. Moreover, the largest derivation was found after double links passed through impact position. This derivation seems to be due to the vibration of the golf club resulting from controller switching. Besides, because the amplitude of the club vibration.

5.5 Discussion

We have given our simulation and empirical study results in the above. Unfortunately, the difficulty of deriving a linearized model for the energy controller with high precision forbids us to further investigate the performance of the controller analytically using classical control

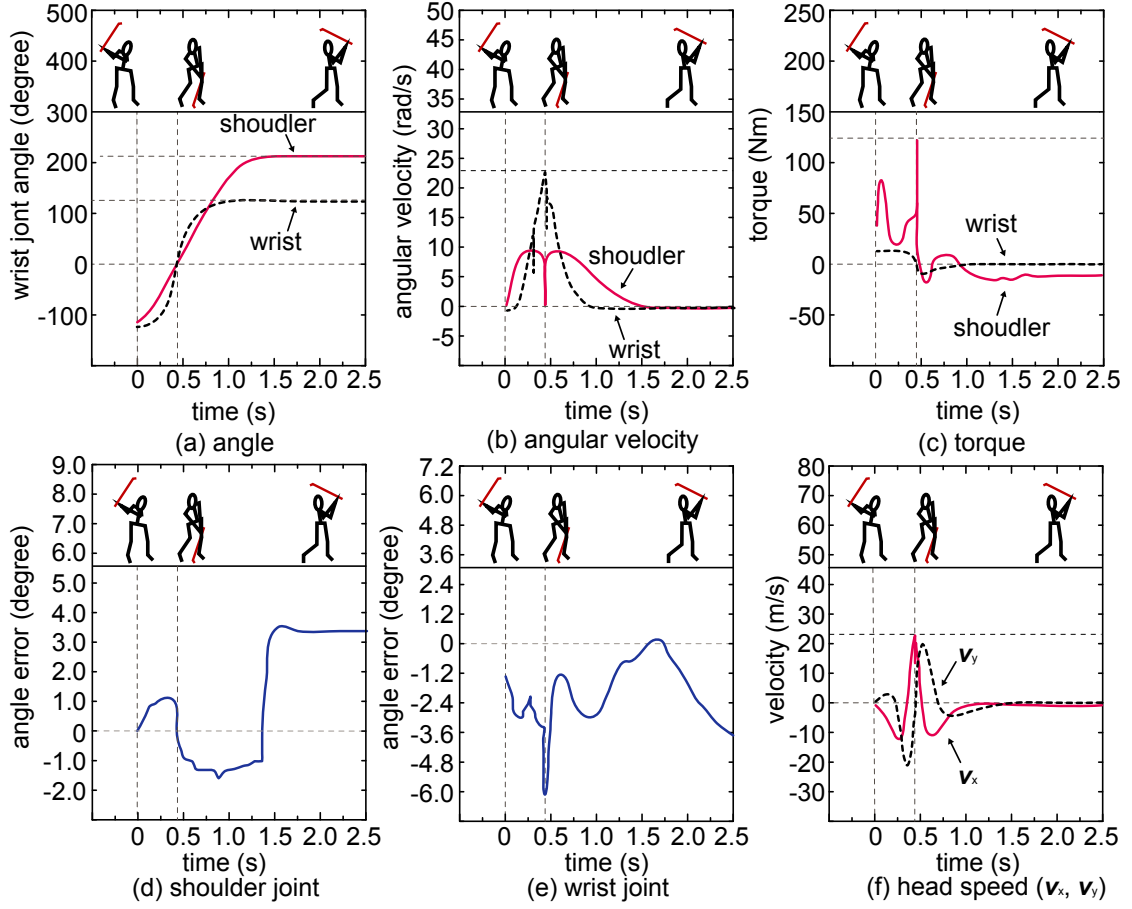


Figure 5.12 – Experiment results of the golf swing with a hitting speed of 25 m/s .

theory. Hereafter we give some preliminary analysis on the proposed controllers.

We proceed the qualitative stability analysis of the energy controller in the target subspace. Differentiating energy E and taking into account equation 5.6, we get the following closed-loop equation of the robot in the target sub-space:

$$\dot{E} - (\ddot{\theta} + \omega^2 \theta) \dot{\theta} = \dot{E} + K_e \dot{\theta}^2 (E - E^*) = 0 \quad (5.18)$$

Equation 5.18 is a highly nonlinear differential equation and is difficult to be linearized with high precision in a large varying range of E^* . Qualitatively, because $E_e > 0$ and $\dot{\theta}_2 \geq 0$, the solution to equation 5.18 asymptotically converges to E^* . This fact implies the

$$E^* = \frac{1}{2} \dot{\theta}^2 + \frac{1}{2} \omega^2 \theta^2 \quad (5.19)$$

Therefore, the closed-loop system can be regarded as stable.

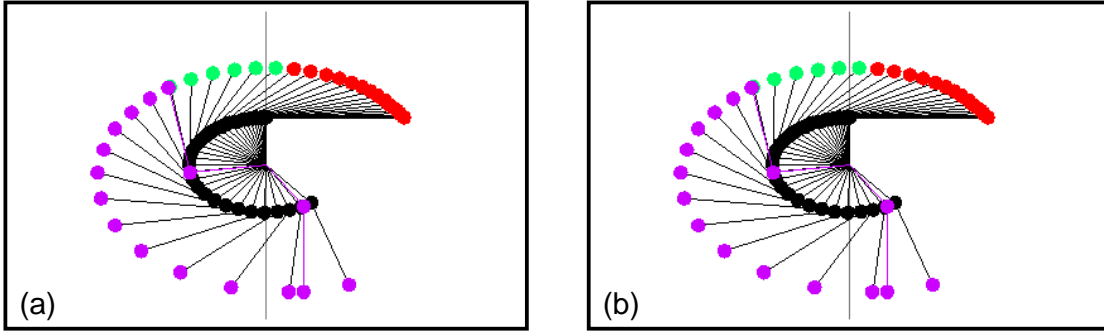


Figure 5.13 – Swing phase of prototype.

we have pointed out the robot controlled by the proposed energy controller does not always pass through the impact position exactly. This is because there are infinite pairs of θ_1 and θ_2 when the pseudo angle θ_0 according to the first equation of equation 5.1. So we use an optimization to find appropriate parameter set of the energy controller satisfying the condition of $\theta(t_m) = \theta_1(t_m) = \theta_2(t_m) = 0$ simultaneously. Unfortunately, such parameter set is required pseudo energy level/hitting speed-dependent, different hitting speed requires different parameter set. The following figures show the simulation results of the golf swing with a hitting speed of 24 m/s using the same controller parameters with those used in the previous simulation. The required energy level $E^* = 221.60$ J.

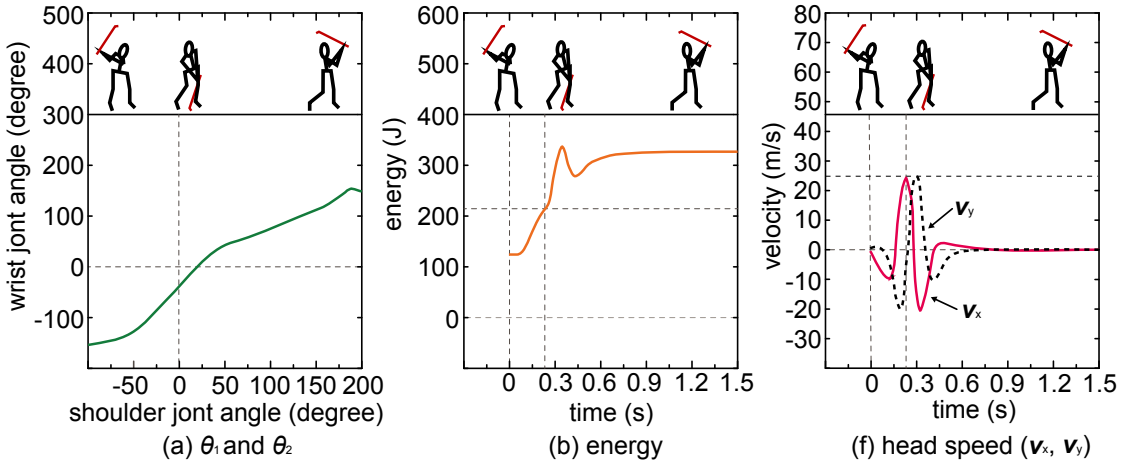


Figure 5.14 – Simulation results of the golf swing with a hitting speed of 24 m/s.

According to the simulation results, the energy level at the impact position ($\theta = 0$) is only 210.89 J (figure 5.14a), 10.71 J less than the required energy level. This means more time is needed for the energy controller to achieve the required energy level before the impact time. Figure 5.14b shows the hitting speed at the impact position is 23.34 m/s while the head speed in Y-direction is -0.54 m/s. This speed in Y-direction is generated because the arm and the

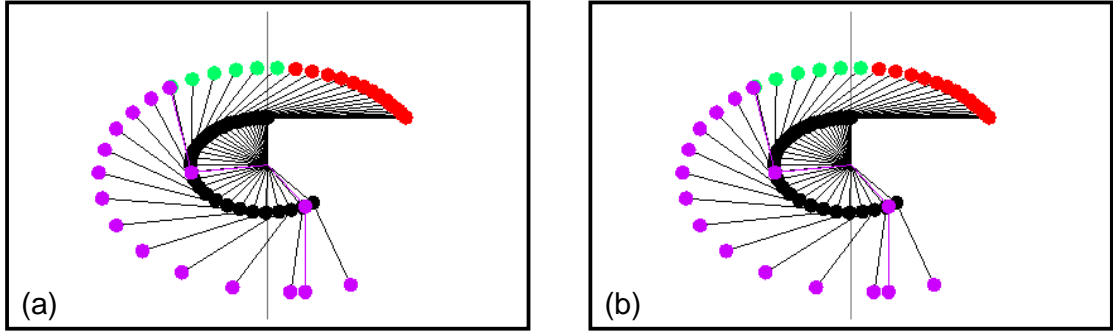


Figure 5.15 – Swing phase of prototype.

club are not downward vertically simultaneously at the impact position, which is indicated clearly in figure 5.14c. In fact, at the impact position, $\theta_1(t_m) = 7.30^\circ$ and $\theta_2(t_m) = -10.04^\circ$.

These facts turn out different hitting speeds require different parameter sets of the energy controller to achieve accurate impact position control. Though no analytical method is known to us to calculate such parameter set, optimization method described in Section 5.3.3 can solve this problem and find appropriate controller parameter sets for various hitting speeds easily.

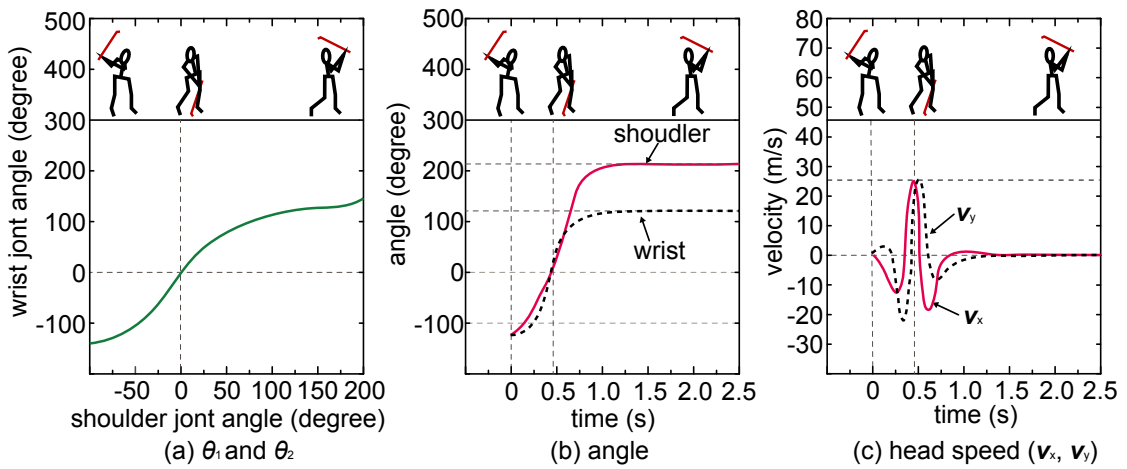


Figure 5.16 – Simulation results of the golf swing with initial angular velocity of the wrist (-0.05 m/s).

It has been pointed out an initial angular velocity of the wrist joint is required to break equilibrium, start swings in the desired direction, and then turn on the energy controller. In practice, impulse like initial torque is usually used to generate such initial angular velocity. However, such torque results in the uncertainty of the initial angular velocity. Preliminary simulation study indicates the energy controller is robust with respect to the uncertainty of the initial angular velocity. Figure 5.13 and figure 5.18 show the results of two cases. The

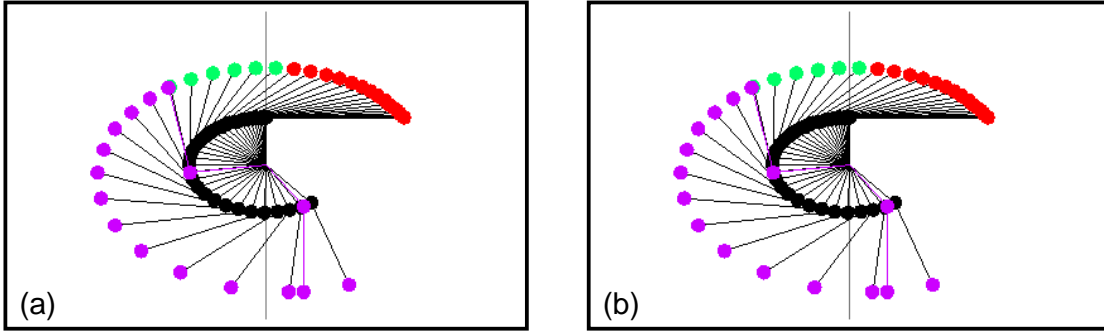


Figure 5.17 – Swing phase of prototype.

parameters of the controllers are the same with those used in section 5.1.

It is obvious though the initial angular velocity of the wrist is about 10 times the one used in section 5.1, the golf swing is still successfully realized. In the simulation with $\dot{\theta}_{2initial} = -0.05 \text{ rad/s}$, the impact positions are $\theta_1(t_m) = -1.01^\circ$ and $\theta_2(t_m) = 1.25^\circ$.

The impact speed is $v_x(t_m) = 24.831 \text{ m/s}$. In the simulation with $\dot{\theta}_{2initial} = -0.1 \text{ rad/s}$, the impact positions are $\theta_1(t_m) = -1.65^\circ$ and $\theta_2(t_m) = 1.53^\circ$, and the hitting speed is $v_x(t_m) = 24.834 \text{ m/s}$. One interesting point is the impact time is brought forward from $t_m = 0.430 \text{ s}$ to 0.420 s , and then to $t_m = 0.458 \text{ s}$ with the increase of the initial angular velocity from -0.01 rad/s to -0.05 rad/s , and then to -0.01 rad/s .

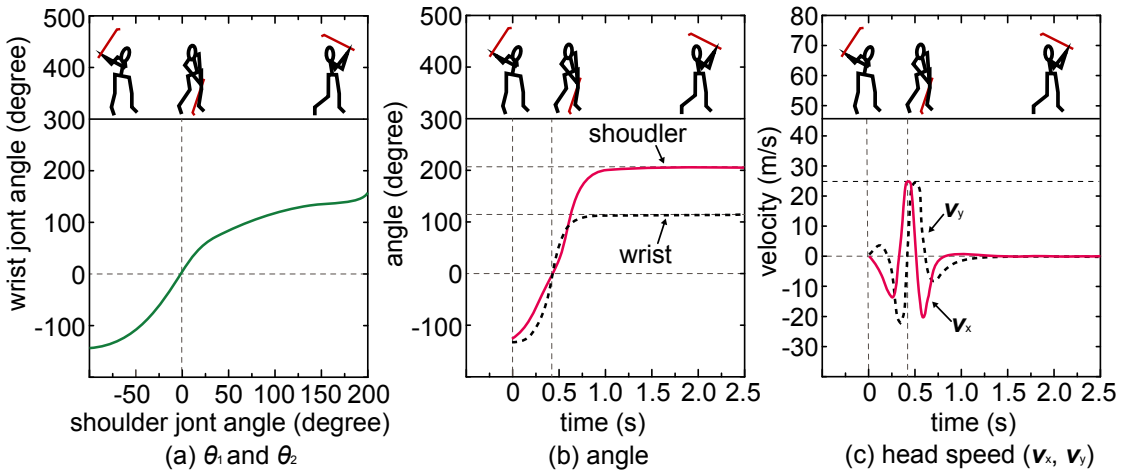


Figure 5.18 – Simulation results of the golf swing with initial angular velocity of the wrist of (-0.1 m/s) .

5.6 Summary

In this chapter, a double-link swing robot was established to investigate human swing motion. An energy controller for backswing and downswing phases and a proportional plus gravity compensation controller for follow-through phase have been proposed. Based on theoretical simulation and empirical study results, it can be found that:

1. The energy controller maps the two-dimension golf swing to a one-dimension harmonic oscillation using the target dynamics method and realizes a golf swing with a specified hitting speed at a specified impact position. Then the proportional plus gravity compensation controller smoothly slows down and stops the swing.
2. Using the proposed energy controller, torque compensation had been realized from the high-power shoulder joint to the low-power wrist joint to avoid instability resulting from torque saturation.

However, though the simulation and experimental results bear out the validity of the proposed controllers, some questions with them still remain open. Most importantly, the energy controller requires fine tuning of its parameters to achieve accurate impact position control. This fact brings trouble on realizing golf swings with various hitting speeds using the same controller. Additionally, how the initial swing state affects the accuracy of the achieved impact position is not clear from the theoretical point of view. Hence a complete mathematical analysis is required.

6 Kinematical Analysis of Golf Swing using Wearable Sensor System

6.1 Introduction

Body movements in human's daily life such as walking, running, walking-up and down the stairs, carrying heavy items, or even sports have the certain patterns; therefore, making a wrong movement pattern can lead to injury. Recently, golfing is one of the most popular sports as anyone at any age or sex can play. Thus, the possibility of golfing in the wrong movement, which causes sudden or chronic injury of low waist muscle or spine in the waist area, is high [Gluck et al.(2008)Gluck, Bendo, and Spivak]. Actually, there are some methods for safety, such as to keep the waist area firm, to make the body adjustable, to keep the back straight while golfing, and to warm-up the body before golfing. Apparently, these methods are not easily be judged by eye-observation without real movement data. Thus, many research topics have been proposed to investigate the proper measuring equipments of movement data or create suitable algorithm to classify and differentiate body movements in daily life.

Since 1980s, the research topics related to human motion tracking for rehabilitation have gradually been concerned [Zhou and Hu(2008)]. Many researchers proposed the methods to classify human motions. For instance, a novel memory-based motion simulation was presented as a general framework to simulate natural human motions [Park and Chaffin(2008)]. In 2010, [Chen and Hung(2010)] introduced the use of acceleration data for movement training in tennis and baseball with a decision tree. In this research, 3 Wiimotes were attached to the limb: grip, upper and lower arm, and then sent the acceleration information of each part of limb: X, Y, and Z-axes back to the computer using wireless link. Later, the acquired information was classified by *ID3* algorithm. This method is suitable for muscle training in some sports such as tennis and baseball. However, the weakness is its large size. [James and Burkett(2011)] pro-

posed the wearable sensor technology with a framework that allowed near real time data analysis of swimming monitoring system. In 2012, the method to recognize human activities and track full-body pose using wearable inertial sensors was proposed by [Schwarz and Mateus(2012)].

Relating to golf swing, measurement methods can be classified into contact and noncontact types, depending upon the sensing device used. A well-known example of the noncontact type is the direct linear transformation (DLT) method, which employs images captured by high-speed cameras. In 2012, [Fedorcik and Queen(2012)] investigated the differences in the wrist kinematics between high and low handicap golfers by using 8-camera motion capture system. This method measures the translations and rotations in the form and estimates force and torque from the motion data, and mass and stiffness coefficients of areas on the player's body and golf club in the captured images. However, in the DLT method, marking points may be hidden behind the body from the camera position by rotation. Resolution of the marking point in the rotation of narrow joints, such as the wrist and the ankle, is too low for accurate measurement.

The contact method uses devices such as force plates, accelerometers, and gripping-force sensors, which are connected to the human body, to generate the data. By combining force plates with the link kinematics model of the human body, the transfer of the center of gravity can be estimated; by introducing these to the kinetics, force and torque can be calculated. The method based on accelerometers calculates rotation from acceleration measured with the kinematics link model, and also calculates torque by applying kinetics to the model. [King et al.(2008)King, Yoon, Perkins, and Najafi] proposed the theory, design, and evaluation of miniature, wireless six degree-of-freedom IMU to compute the dynamics of golf swing. In 2011, [Lai et al.(2011)Lai, Hetchl, Wei, Ball, and Mclaughlin] introduced the use of micro-electromechanical systems (MEMs) inertial sensors to measure the differences between skilled golfers and non-golfers. In order to analyze the movement patterns in each part of the body while golfing, the key technical parameters in the golf swing that affected the analysis must be concerned.

In the previous chapters, kinematical analysis of swing motion was conducted based on a double pendulum model. Also in order to gain insight of natural release, a golf swing robot was established to investigate the relationship between angular velocity and angular acceleration, torques exerted on shoulder and wrist joint, and input energy which used to drive golf swing throughout the whole swing phases. Related simulation and experiment were all carried on in a restrained condition that the model were assumed to be rigid segments and motion happened in a perfect swing plane. Correspondingly, a 6-camera motion capture system served as the

reference system without considering influence of main errors caused by mankind subjects. In this chapter, we proposed a novel measurement method and system using inertia sensors. A Kalman filter that fuses triaxial accelerometer and triaxial gyroscope signals for ambulatory recording of human body segment orientation. Body segment orientation data obtained with the wearable sensor system was compared with the data obtained using a 6-camera motion capture system. Before comparison, the data using DTL method would be processed by the Kalman smoothing method which was proposed in chapter 4. Details are provided on how to measure rotation, including angle, angular velocity, and acceleration, and calculate the translation in 3-D space from the measured angles, as well as to the quantitative evaluation of golf skill.

6.2 Coordinate Systems and Transformation

6.2.1 Translation in three-dimensional space

In the analysis of experimental joint mechanics data, the transformation of point coordinates from one coordinate system to another is a frequent task [Williamson and Andrews(2001)]. A typical application of such a transformation would be gait analysis data recorded in a laboratory fixed coordinate system that must be converted to a reference system fixed to the skeleton of the test subject.

The laboratory fixed coordinate system may be designated by xyz and the body reference system by $(u_1 u_2 u_3)$ (figure 6.2.a). The location of a point S in the body reference system is defined by the radius vector:

$$S = a \cdot e_a + b \cdot e_b + c \cdot e_c$$

Consider the reference system to be embedded into the laboratory system. Then the radius vector describes the origin of the reference system in the laboratory system is expressed as:

$$r_m = x_m \cdot e_x + y_m \cdot e_y + z_m \cdot e_z$$

Then the location S is now expressed by the coordinates a, b, c . The vector equation $r = r_m + s$ gives the radius vector for point S in the laboratory system. Employing the full notation:

$$r = (x \cdot e_x + y \cdot e_y + z \cdot e_z) = (a \cdot e_a + b \cdot e_b + c \cdot e_c) + (x_m \cdot e_x + y_m \cdot e_y + z_m \cdot e_z)$$

A set of transformation equations results after some intermediate matrix algebra to describe the coordinates. The scalar products of the unit vectors in the xyz and abc systems produce a set of nine coefficients C_{ij} . The cosine of the angle between the coordinate axes of the two systems corresponds to the value of the scalar products. Three “direction cosines” define the orientation of each unit vector in one system with respect to the three unit vectors of the other system. Due to the inherent properties of orthogonality and unit length of the unit vectors, there are six constraints on the nine direction cosines, which leave only three independent parameters describing the transformation. Employing the matrix notation of the transformation equation:

$$\begin{bmatrix} x \\ y \\ z \end{bmatrix} = \begin{bmatrix} x_m \\ y_m \\ z_m \end{bmatrix} + \begin{bmatrix} c_{11} & c_{12} & c_{13} \\ c_{21} & c_{22} & c_{23} \\ c_{31} & c_{32} & c_{33} \end{bmatrix}$$

In coordinate transformations the objects remain unchanged and only their location and orientation are described in a rotated and possibly translated coordinate system. If a measurement provides the relative spatial location and orientation of two coordinate systems the relative translation of the two systems and the nine coefficients C_{ij} can be calculated. The coefficients are adequate to describe the relative rotation between the two coordinate systems.

6.2.2 Rotations about the coordinate axes

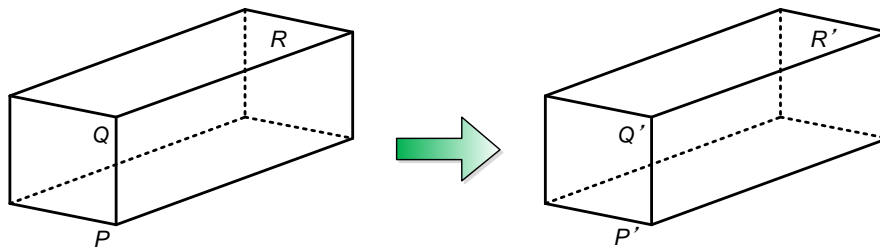


Figure 6.1 – Transformation of a rigid body.

Translation in 3-dimensional space, a rigid body as show in figure 6.1 moves parallel to itself. Pure translation in 3-dimensional space leaves the orientation of the body unchanged as in the condition of 2-dimensional translation.

In translation in 3D space the rigid object moves parallel to itself. Pure translation in 3D space leaves the orientation of the body unchanged as in the case of pure 2D translation. A rotation in three-dimensional space is defined by specifying an axis and an angle of rotation (figure 6.2.b).

The axis can be described by its 3D orientation and location [Woltring(1980)].

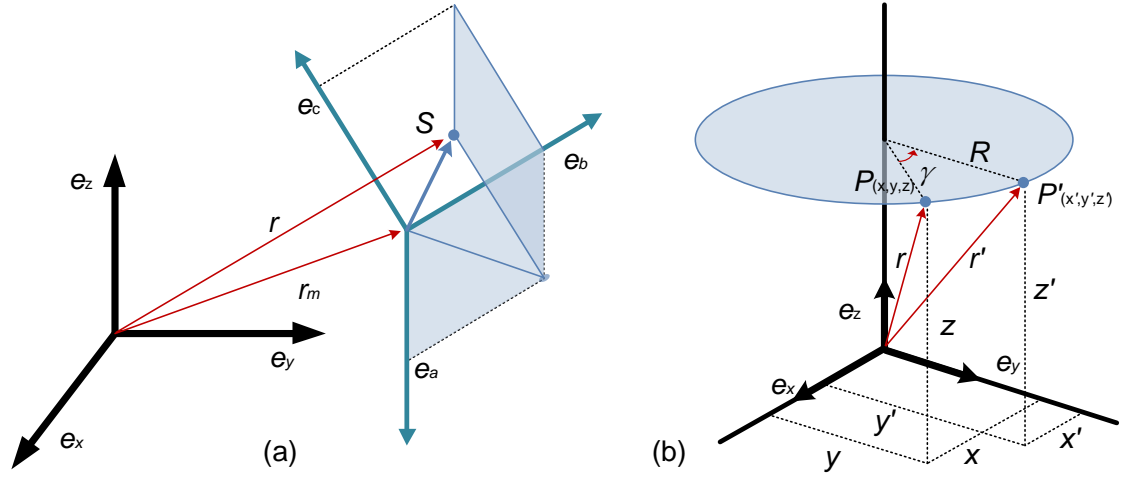


Figure 6.2 – Transformation of coordinate systems. (a) transformation of point coordinates from one coordinate system to another; (b) rotation about the Z-axis of the coordinate system.

A rotation, as does the translation explained earlier, leaves all the points on the axis unchanged; all other points move along circular arcs in planes oriented perpendicular to the axis.

This rotation moves an arbitrary point P to location P' with constant distance Z from the XY -plane ($Z = Z'$). This produces the following matrix notation for the respective equations for the rotation that changes x and y -coordinates but leaves the Z -coordinate unchanged.

$$r = \begin{bmatrix} x' \\ y' \\ z' \end{bmatrix} = \begin{bmatrix} \cos \gamma & -\sin \gamma & 0 \\ \sin \gamma & \cos \gamma & 0 \\ 0 & 0 & 1 \end{bmatrix} \begin{bmatrix} x \\ y \\ z \end{bmatrix} = D_z(\gamma) \cdot r$$

The matrix describing a rotation about the Z -axis is designated $D_z(\gamma)$. The matrices describing a rotation about the Y -axis through angle β and about X -axis through angle α are similar.

$$r = \begin{bmatrix} x' \\ y' \\ z' \end{bmatrix} = \begin{bmatrix} \cos \beta & 0 & \sin \beta \\ 0 & 1 & 0 \\ -\sin \beta & 0 & \cos \beta \end{bmatrix} \begin{bmatrix} x \\ y \\ z \end{bmatrix} = D_z(\beta) \cdot r$$

$$r = \begin{bmatrix} x' \\ y' \\ z' \end{bmatrix} = \begin{bmatrix} 1 & 0 & 0 \\ 0 & \cos \alpha & -\sin \alpha \\ 0 & \sin \alpha & \cos \alpha \end{bmatrix} \begin{bmatrix} x \\ y \\ z \end{bmatrix} = D_z(\alpha) \cdot r$$

Assume that the first rotation of a rigid body occurs about the z -axis of a coordinate system. The second rotation occurs supposedly about the X' -axis, i.e., about a body-fixed axis on the body (previously rotated about its Z -axis). Matrix intermediate calculation here gives: $r'' = D_{z'} * D_{x'} * r$. In this calculation the sequence of the matrices is very important especially as this sequence differs from what one might expect. First, the matrix of the second partial rotation acts on the vector r and then, in a second step on the matrix of the first partial rotation. If the sequence of the two partial rotations is interchanged, the combined rotation is described by: $r'' = D_x * D_z * r$.

6.3 Material and Methods

In many biomechanical applications, it is critical to detect loads and motions of certain segments of human body, such as hand-gesture analysis, gait analysis, and muscle tension analysis, which is the first step in implementation of biomechanical analysis system. Some sensory systems consisting of multi-camera motion capture system and force platform (figure 6.3.a) have been successfully applied to tracking motions of human body segments and measuring ground-reaction forces and moments prepared for performing human dynamics analysis [Aminian et al.(2004)Aminian, Trevisan, and Najafi]. However, the camera system needs large space and high speed graphic signal processing devices, and the size of force platform restrict the extension of reaction force measurement. Moreover, cost of such system is high, and the system is more appropriate to be used in laboratory.

On contrary, advancements in microelectronics and wireless communication have enabled the design of light-weight embedded sensory devices [Benini and Farella(2006)]. Wearable motion sensory system with high reliability and high precision is a cost saving solution, and has a great perspective for applications of biomechanical measurement (figure 6.3.b). Ability of wireless sensor platforms to perform computations, store necessary data, and communicate within a short range make them attractive for the development of wearable systems. We chose to focus our research on golf because golf is a sport of delicate angles and forces. Consider the precision necessary to deliver a 4.3 *cm* diameter ball to an 11 *cm* diameter target about 225 *m* away in just 3 strokes or hits. This popular game requires a complicated sequence of motions to swing the golf club properly with the primary goal of propelling the golf ball a certain distance in a desired direction. A proper golf swing can make the difference between a long straight ball flight and a shorter hook or slice as a result of an improper swing. A repeatable and consistent golf swing can also dramatically improve a golfer's score. However, this single movement which has such a major impact on the player's overall game is difficult to master

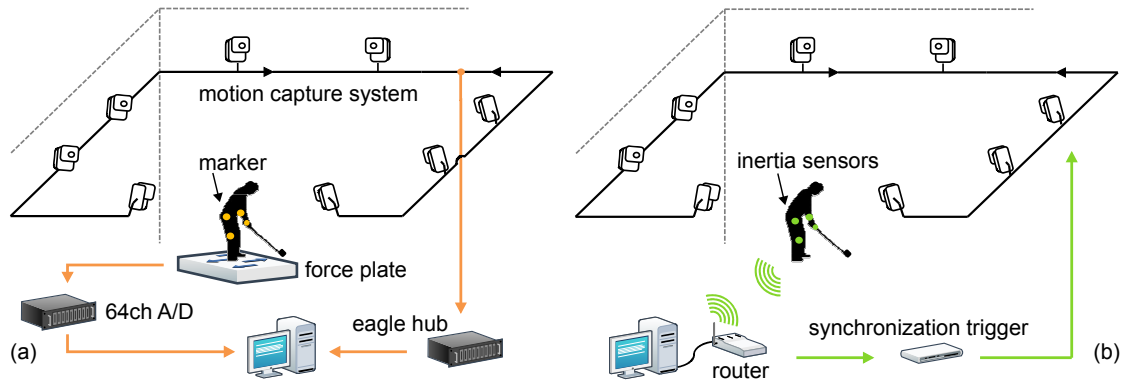


Figure 6.3 – Motion capture system. (a) traditional motion capture system; (b) wearable motion capture system.

and execute consistently for players who are new to the sport or have little experience.

Use of sensors to aid the game of golf has been explored in the past. Some systems have sensors built into the club. [King and Yoon(2008)] used accelerometers and gyroscopes that are built into the club handle. [Ghasemzadeh and Loseu(2009)] presented methods where multiple sensors are attached to the golfer's body and various parameters are computed. In contrast, our system is a stand alone system that can be attached to any device with consideration of angle variance between wrist and thumb. Moreover, a fairly involved filtering method was employed to remove bias and errors inherent in the sensors.

6.3.1 Wearable sensor system for upper limbs

As shown in figure 6.4.a, embedded with custom-designed sensor board, the measurement system is a nine degrees of freedom (9-dimension) motion MEMS-sensor, which mainly consists of a triaxial accelerometer, a triaxial gyroscope, a triaxial magnetic sensor, and microcontroller.



Figure 6.4 – Motion sensor for golf swing. (a) motion sensor; (b) definition of coordinate system.

Chapter 6. Kinematical Analysis of Golf Swing using Wearable Sensor System

The sensor system are mounted on the upper limbs to capture significant motions during the swing. The movements of the golf player are recorded by the two separated parts (wrist and thumb part). This configuration avoids putting any extra weight on the clubs shafts. Save time, unnecessary to detach, reattach the sensor when switching clubs. It ensures that inertial information was captured associated with the major parts of the upper limb involved during swing. Wrist part located on the left wrist of golf player with the direction of sensitivity oriented along the axis of the shaft. Thumb part was connected with a cable, whose direction oriented along the axis of the left thumb.

Table 6.1 – Technical specifications of sensor system.

Parameter	Value
interface	1 macro USB port
frequency	2.4 – 2.4835 <i>GHz</i>
signal rate	150 <i>Mbps</i>
working radius	15 <i>Meters</i>
battery	2.5 <i>hour</i> in a full charged cycle

Nine channels sensor signals are digitized and wirelessly broadcast to a PC, enabling data storage and signal analysis. While this under samples the higher-pass-filter built into the output stage of the system, this update rate is fast enough for the time scales appropriate to all phases of swing process, except perhaps in the few milliseconds near impact position. Interpretation of this data is based on the double pendulum model of the golf swing discussed in chapter 2. The sensor system are powered by a Li-Ion battery integrated with each functional part. Technical specifications of sensor system are shown in table 6.1

The sensor system measures triaxial accelerations and angular velocities which are used to estimate 3D orientation transformation matrix. Then, so implement the ambulatory 3-dimensional orientation. As defined in figure 6.4.b, the whole system refers to the right-handed coordinate, the x -axis was defined vertical to the surface of wrist part of sensor system, the z -axis of the sensor system was defined to represent the anterior-posterior direction along with golf club, and the y -axis was vertical to the plane determined by x and z -axis. The transformation matrix can be expressed by:

$$R = \begin{bmatrix} q_0^2 + q_1^2 - q_2^2 - q_3^2 & 2(q_1 q_2 - q_0 q_3) & 2(q_1 q_3 + q_0 q_2) \\ 2(q_0 q_3 + q_1 q_2) & q_0^2 - q_1^2 + q_2^2 - q_3^2 & 2(q_2 q_3 - q_0 q_1) \\ 2(q_1 q_3 - q_0 q_2) & 2(q_0 q_1 + q_2 q_3) & q_0^2 - q_1^2 - q_2^2 + q_3^2 \end{bmatrix} \quad (6.1)$$

where, q_0 , q_1 , q_2 and q_3 are quaternion. Then after the coordinate transform, the triaxial

accelerations are described as:

$$\begin{bmatrix} A_X \\ A_Y \\ A_Z \end{bmatrix} = \begin{bmatrix} q_0^2 + q_1^2 - q_2^2 - q_3^2 & 2(q_1 q_2 - q_0 q_3) & 2(q_1 q_3 + q_0 q_2) \\ 2(q_0 q_3 + q_1 q_2) & q_0^2 - q_1^2 + q_2^2 - q_3^2 & 2(q_2 q_3 - q_0 q_1) \\ 2(q_1 q_3 - q_0 q_2) & 2(q_0 q_1 + q_2 q_3) & q_0^2 - q_1^2 - q_2^2 + q_3^2 \end{bmatrix} \cdot \begin{bmatrix} A_X \\ A_Y \\ A_Z \end{bmatrix} \quad (6.2)$$

where, $[A]$ represents the acceleration vector. Because zero-drift problem, it is necessary to conduct signal processing to remove the noise including in the data. The higher-pass-filter can be described as:

$$\begin{bmatrix} A_X(k) \\ A_Y(k) \\ A_Z(k) \end{bmatrix} = \begin{bmatrix} A_X(k) \\ A_Y(k) \\ A_Z(k) \end{bmatrix} - \left(\begin{bmatrix} A_X(k) \\ A_Y(k) \\ A_Z(k) \end{bmatrix} + \begin{bmatrix} A_X(k-1) \\ A_Y(k-1) \\ A_Z(k-1) \end{bmatrix} \right) / 2 \quad (6.3)$$

where, $[G_X + G_Y + G_Z]^T = [0 \ 0 \ 1]^T$. Because the sensor system utilizes the earth's magnetic field as reference, the accuracy of 3-dimensional orientation is influenced by the magnetic field distortion. Therefore, A simplified magnetometer calibration method was adopted to calibrate the accuracy of 3-dimensional orientation measurement of the sensor system [Liu and Wang(2011)]. Based on the triaxial accelerations, triaxial velocities can be described as:

$$\begin{bmatrix} A_X(k) \\ A_Y(k) \\ A_Z(k) \end{bmatrix} = \begin{bmatrix} A_X(k) \\ A_Y(k) \\ A_Z(k) \end{bmatrix} - \begin{bmatrix} G_X \\ G_Y \\ G_Z \end{bmatrix} \quad (6.4)$$

where, V represents the velocity vector. The initial value of A is zero. $T = 0.01 \text{ s}$ is the sampling interval.

$$\begin{bmatrix} V_X(k) \\ V_Y(k) \\ V_Z(k) \end{bmatrix} = \begin{bmatrix} A_X(k-1) \\ A_Y(k-1) \\ A_Z(k-1) \end{bmatrix} + \begin{bmatrix} A_X(k) \\ A_Y(k) \\ A_Z(k) \end{bmatrix} T \quad (6.5)$$

According to the triaxial velocities, the real-time bio-feedback can be realized simply. The triaxial displacements can be described as:

$$\begin{bmatrix} S_X(k) \\ S_Y(k) \\ S_Z(k) \end{bmatrix} = \begin{bmatrix} V_X(k-1) \\ V_Y(k-1) \\ V_Z(k-1) \end{bmatrix} + \begin{bmatrix} V_X(k) \\ V_Y(k) \\ V_Z(k) \end{bmatrix} T \quad (6.6)$$

where, S represents displacement vector and V was initialized to 0.

6.3.2 Wearable sensor system for upper limbs

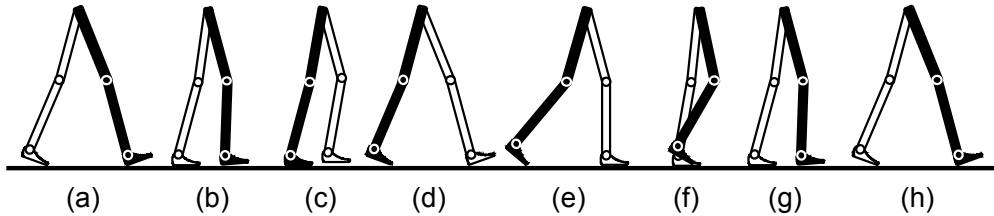


Figure 6.5 – Definition of gait phases. (a) initial contact; (b) loading response; (c) mid stance; (d) terminal stance; (e) pre-swing; (f) initial swing; (g) mid swing; (h) terminal swing.

The purpose of lower limb motion analysis system is to capture the whole leg (thigh, shank, and foot) motion variation during movement in 3-dimensional space. Ordinarily, a normal walking gait cycle is divided into 8 different gait phases [Liu et al.(2010b)Liu, Inoue, and Shibata], including eight different gait phases: initial contact, loading response, mid stance, terminal stance, pre swing, initial swing, mid swing and terminal swing (figure 6.5). Each of the eight gait phases has a functional objective and a critical pattern of selective synergistic motion to accomplish this goal. The sequential combination of the phases also enables the limb to accomplish three basic tasks, which include weight acceptance, single limb support and limb advancement. Weight acceptance begins the stance period and uses phases of initial contact and loading response. Single limb support continues stance with phases of mid stance and terminal stance. Limb advancement begins in phase of pre-swing and then continues through the three phases of initial swing, mid swing and terminal swing.

As shown in figure 6.6, the sensor system detects gait phases by using two types of inertial sensors. More specific, three gyroscopes are used to measure angular velocities of leg segments of foot, shank and thigh. The sensing axis is vertical to the medial-lateral plane so that the angular velocity in the sagittal plane can be detected. In local coordinates of three segments, sensing axis of the gyroscopes is along with Y -axis, and the Z -axis is along with leg bone. A 2-axis accelerometer is mounted on the side of shank to measure accelerations along with tangent direction of Z -axis and sagittal direction of Z -axis. The principle operation of the gyroscope is the measurement of the Coriolis acceleration, which is generated when a rotational angular velocity is applied to the oscillating piezoelectric bimorph. The inertial sensor can work under low energy consumption, and are appropriate for ambulatory measurements.

A microcontroller is used to develop the pocketed data, and sampling data from the inertial

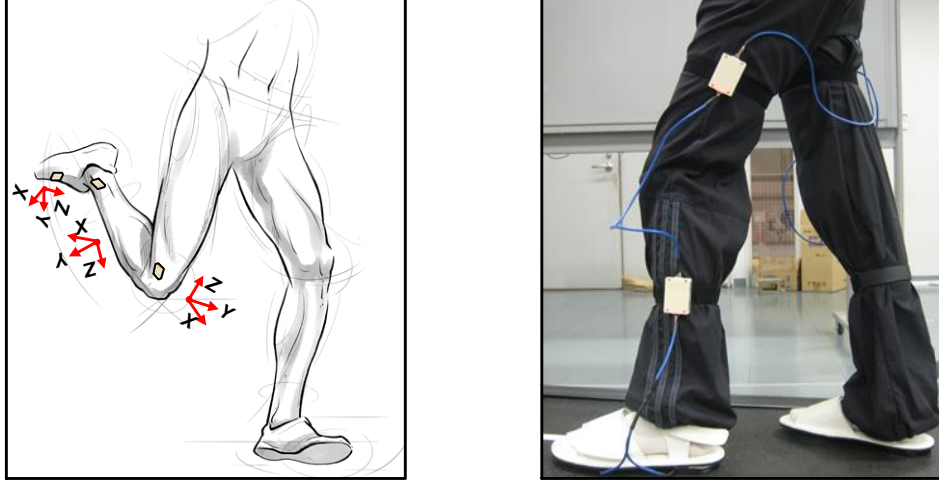


Figure 6.6 – Position and coordinates of the sensor units. (a) thigh part, 1-axis gyroscope sensitive to y -pitch velocity; (b) shank part, 1-axis gyroscope and 2-axis accelerometer; (c) foot part, 1-axis gyroscope sensitive to y -pitch velocity.

sensors. Sensor signals are sampled at a frequency of 100 Hz with a resolution of 14 *bits* through A/D card, then wirelessly broadcast to a computer, enabling data storage and signal analysis. Assuming that the subject is viewed from the right lateral side and considering that anticlockwise rotation is positive. θ_f , θ_s , and θ_t are inclination angles of the foot, shank and thigh in the lateral plane. θ_{f0} , θ_{s0} , θ_{t0} are defined as initial quantities of the orientation angle. ω_f , ω_s , and ω_t represent the angular velocities of the foot, shank and thigh in the lateral plane. Finally, ε_ω , ε_α , and ε_θ are defined as threshold values for angular velocities, accelerations, and displacement, which near to 0 *degree*. A completed gait cycle is expressed as following:

Step 1 following the terminal swing, start initial contact. The hip is flexed, the knee is extended ($\theta_s - \theta_t = \theta_{s0} - \theta_{t0}$), and the ankle is neutral ($\theta_f - \theta_s = \theta_{f0} - \theta_{s0}$). The inclinations of the leg segments are obtained by integrating the gyroscopes signal. Sensor condition: $\omega_f = \omega_s = \omega_t = \varepsilon_\omega$.

Step 2 following the initial contact, start loading response. Heel served as a rocker, the knee is flexed for shock absorption ($\theta_s - \theta_t < \theta_{s0} - \theta_{t0}$). Sensor condition: $\omega_f < 0$, $\omega_s < 0$, and $\omega_t < 0$.

Step 3 following the loading response, start of mid stance. The limb advances over the stationary foot by ankle rocker when the knee and hip extend ($\theta_s - \theta_t = \varepsilon_\theta$). Sensor condition: $\omega_f = \varepsilon_\omega$, $\omega_s < 0$, and $\omega_t < 0$.

Step 4 following the mid stance, start terminal stance. Begin with heel rise and continue until the other foot strikes the ground, in which the heel rise and the limb advance over the forefoot rocker ($\theta_s - \theta_t = \theta_{s0} - \theta_{t0}$, $\theta_f < 0$, $\theta_s < 0$, and $\theta_t < 0$). Sensor condition: $\omega_f < 0$,

$\omega_s < 0$, and $\omega_t < 0$.

Step 5 following the terminal stance, start of pre-swing. The limb responds with increased ankle plantar flexion ($\theta_s < 0$), greater knee flexion ($\theta_s - \theta_t < 0$) and loss of hip extension. Sensor condition: $\omega_f < 0$, $\omega_s < 0$, and $\omega_t < 0$.

Step 6 following the pre-swing, start initial swing. The foot is lifted and limb advanced by hip flexion and increased knee flexion ($\theta_s - \theta_t < 0$). Sensor condition: $\omega_f > 0$, $\omega_s > 0$, and $\omega_t > 0$.

Step 7 following the initial swing, start mid swing. The knee extended in response to gravity affection when the ankle continues to neural ($\theta_s - \theta_t < 0$, $\theta_t > 0$, and $\theta_s < \varepsilon_\theta$). Sensor condition: $\omega_f > 0$, $\omega_s > 0$, and $\omega_t > 0$.

Step 8 following the mid swing, start terminal swing. Limb advancement is completed as the shank moves ahead of the thigh. The limb advancement is completed by knee extension, and the hip maintains its earlier flexion ($\theta_f - \theta_s = \theta_{f0} - \theta_{s0}$) and the ankle remains to neural. Sensor condition: $\omega_f - \omega_s = \varepsilon_\omega$, and $\omega_t > 0$.

6.3.3 Signal fusion method for wearable sensor system

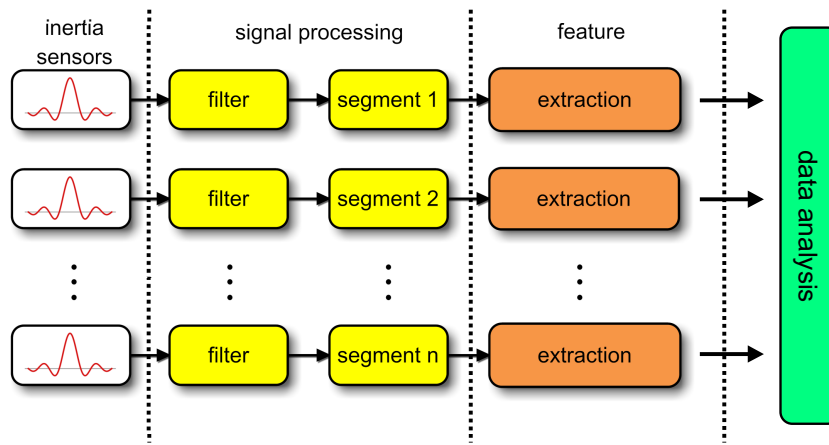


Figure 6.7 – Signal processing blocks for motion analysis.

The wearable sensor system based on inertial sensors processes a great perspective for applications in biomechanical research. However, error accumulation during measurement because of offset drift generated by the gyroscope is a critical problem exists in wearable sensor system. Addressing to this problem, high-pass filtering and low-pass filtering were applied to output signals [Liu et al.(2009b)Liu, Inoue, and Shibata]. Considering the diversity of human gait and low frequency property of joint angle variation, this method was inapplicable to clinical application. The Kalman filter was effectively to solve error accumulation during

wearable sensor measurement. Our previous work illustrated effectiveness of measurement on ground reaction forces and human lower limb motion analysis based on Kalman filter [Liu et al.(2010a)Liu, Inoue, and Shibata]. However, in previous researches, measurement of joint angle variation was not tested in considering that subjects finish gait cycle at different speeds. What the impact on human lower limb including hip, knees, and ankle joint angles.

The wearable system is designed for assessing quality of golf swings aims to utilize processing capability of each sensor. The process consists of several steps as illustrated in figure 6.7. In this section, a Kalman filter was designed for fusing output signals of a wearable sensor system considering reduce the error accumulation impact of inertial sensors at different gait speeds during cycle. The lower limb joint angles obtained with this wearable system were compared with the reference joint angles obtained with a camera motion capture system.

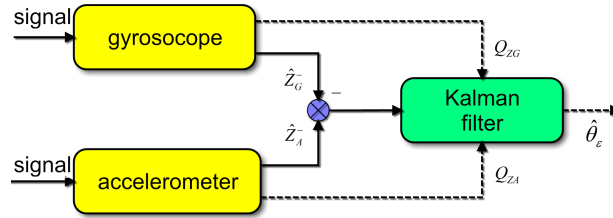


Figure 6.8 – Structure of Kalman filter.

In order to reduce error accumulation, a Kalman filter was designed to estimate orientation by combining signals of accelerometer and gyroscope based on a model of the inertial measurement unit (*IMU*) system and relevant signals. The structure of the estimation procedure is shown in figure 6.8. Based on the model describing the sensor signals, both the 3D gyroscope and 3D accelerometer systems yield a measure of inclination (\hat{Z}_G^- and \hat{Z}_A^- , respectively), each with different accuracies and error sources. The inclination difference ($\hat{Z}_A^- - \hat{Z}_G^-$) is a function of errors in the two measurement systems, particularly an orientation error and an offset error generated by gyroscope sensors. This formula is the description of error model. Based on the inclination difference calculated by error model, Kalman filter estimates the orientation errors and offset drift errors in a statistical method. Then, both calculated errors are used as references to correct the wearable sensor system at each time step.

Wearable sensor system is designed to mount on the human lower limb. Make an assumption that sensor system rotates and translates with subject body segment in the global coordinate. Based on this assumption, an error model of output signals is established in state space format. With considering measurement noise, the error model described relationship between orientation errors and offset.

According to this error model, Kalman filter fuses output signals of wearable sensor system. Based on the assumption we have made, error model was conducted. During experiment, every tiny change of parameters of the filter caused by body segments movement will be divided and classified by frequencies of property.

As shown in figure 6.6, in the global coordination, orientation of the subject was defined as Y -axis direction. Z -axis direction is vertical to the ground. During experiment, measurement result \vec{A}_s is defined by combination of gravity acceleration \vec{A}_g , motion acceleration \vec{A}_m and measurement noise \vec{A}_e . The Kalman filter uses a state space representation to model the relationship between errors in estimated model variables and the error in the inclination predicted by the equation 6.7.

$$A_s = A_g + A_m + A_e \quad (6.7)$$

Equation 6.7 describes the variation of angle joints at each time step and defined the motion of each degree of freedom. While equation is based on the assumption that model state is uncertainty. With triaxial angular velocity, condition equation of A_g can be defined as:

$$\begin{bmatrix} A_g^X \\ A_g^Y \\ A_g^Z \end{bmatrix} = \begin{bmatrix} 0 & -\omega^Z & \omega^Y \\ -\omega^Z & 0 & -\omega^X \\ \omega^Y & -\omega^X & 0 \end{bmatrix} \begin{bmatrix} A_g^X \\ A_g^Y \\ A_g^Z \end{bmatrix} \quad (6.8)$$

Defined state observer equation as:

$$\begin{bmatrix} y^X \\ y^Y \\ y^Z \end{bmatrix} = \begin{bmatrix} y^{X-} \\ y^{Y-} \\ y^{Z-} \end{bmatrix} + \begin{bmatrix} Q^X \\ Q^Y \\ Q^Z \end{bmatrix} \quad (6.9)$$

According to equation 6.7, 6.8, and 6.9, signals of gyroscope sensor were processed by Kalman filter based on conversion of coordinates.

$$\begin{bmatrix} M^X \\ M^Y \\ M^Z \end{bmatrix} = \begin{bmatrix} 1 & 0 & 0 \\ 0 & \cos(C_x) & -\sin(C_x) \\ 0 & \sin(C_x) & \cos(C_x) \end{bmatrix} \begin{bmatrix} \cos(C_y) & 0 & \sin(C_y) \\ 0 & 1 & 0 \\ -\sin(C_y) & 0 & \cos(C_y) \end{bmatrix} \begin{bmatrix} M_g^X \\ M_g^Y \\ M_g^Z \end{bmatrix} \quad (6.10)$$

where, $[M_g^X, M_g^Y, M_g^Z]^T$ is the output of Kalman filter. With the variation of. With the variation

of $[M^X, M^Y, M^Z]^T$, Euler angular of Z-axis direction can be found using equation 6.11.

$$C_Z = \begin{cases} -\tan^{-1}\left(\frac{M^X}{M^Y}\right), & \text{if } (M^Y \geq 0) \\ \frac{\pi}{2}, & \text{if } (M^X > 0 \& M^Y == 0) \\ -\frac{\pi}{2}, & \text{if } (M^X < 0 \& M^Y == 0) \\ \pi + \tan^{-1}\left(\frac{M^X}{M^Y}\right), & \text{if } (M^X > 0 \& M^Y < 0) \\ -\pi + \tan^{-1}\left(\frac{M^X}{M^Y}\right), & \text{if } (M^X < 0 \& M^Y > 0) \end{cases} \quad (6.11)$$

Figure 6.9 shows the loop scheme of gait cycle. From the initial contact to toe off stage, we defined start point and end point of subjects in one cycle. The error generated by accelerometer sensors influenced by the error evaluated acceleration described in the glob coordinate and the measurement noise. The predicted error of acceleration was calculated by comparing the recorded acceleration by sensor system with the evaluated acceleration.

In the globe coordinate, in order to calculated acceleration error, equation 6.12 was adopted by using evaluation of the acceleration error estimate and evaluation of the body segment orientation. The resulting error is caused by both an orientation error and an error in the global acceleration estimate.

$$\begin{aligned} \begin{bmatrix} \Psi \\ \theta \\ \varphi \end{bmatrix} &= \begin{bmatrix} 1 & 0 & 0 \\ 0 & 1 & 0 \\ 0 & 0 & 1 \end{bmatrix} \begin{bmatrix} \Psi^- \\ \theta^- \\ \varphi^- \end{bmatrix} + \begin{bmatrix} R^X \\ R^Y \\ R^Z \end{bmatrix} \\ &+ \begin{bmatrix} 0 & \frac{\sin(\varphi^-)}{\cos(\theta^-)} & \frac{\cos(\varphi^-)}{\cos(\theta^-)} \\ 0 & \cos \varphi^- & -\sin \varphi^- \\ 1 & \sin \varphi^- \tan \theta^- & \cos \varphi^- \tan \theta^- \end{bmatrix} \begin{bmatrix} \omega_x^- \\ \omega_y^- \\ \omega_z^- \end{bmatrix} Ts \end{aligned} \quad (6.12)$$

Defined state observer equation as:

$$\begin{bmatrix} \Psi_M \\ \theta_a \\ \varphi_a \end{bmatrix} = \begin{bmatrix} \Psi^- \\ \theta^- \\ \varphi^- \end{bmatrix} + \begin{bmatrix} Q^X \\ Q^Y \\ Q^Z \end{bmatrix} \quad (6.13)$$

With the compensation of state observer equation 6.13, signal of gyroscope sensor was processed by Kalman filter based on conversion of coordinates.

$$\begin{bmatrix} \dot{M}^X \\ \dot{M}^Y \\ \dot{M}^Z \end{bmatrix} = \begin{bmatrix} \cos(\theta) & \sin(\varphi) \sin(\theta) & \cos(\varphi) \sin(\theta) \\ 0 & \cos(C_x) & -\sin(\varphi) \\ -\sin(\theta) & \sin(\varphi) \cos(\theta) & \cos(\varphi) \cos(\theta) \end{bmatrix} \begin{bmatrix} M^X \\ M^Y \\ M^Z \end{bmatrix} \quad (6.14)$$

The equation 6.14 was found by assuming that the gyroscope noise variance is equal in the x , y and z -directions. In this case, the noise covariance matrix does not change when the noise is expressed in a different reference system.

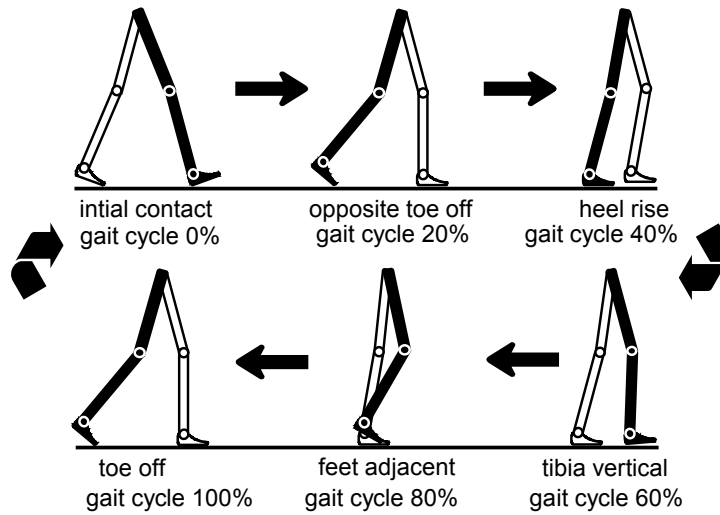


Figure 6.9 – Definition of gait cycle.

6.3.4 Experiments

validation of Kalman filter for lower limb measurement



Figure 6.10 – The lower limb model. Markers were attached to each body segment (18 markers in total).

In previous study, a motion analysis sensor unit ($35 \times 50 \times 15 \text{ mm}^3$, 20 g) were designed

to measure 3 dimensional orientations of lower limbs (figure 6.10), as shown in figure 6.6. Based on the Kalman filter algorithm, signal processing was conducted. Signal outputs of accelerometers and magnetic sensors were incorporated with dynamics of the gyroscope. During experiment, sensor units are attached to lower limb segments (table 6.2), after signal processing, orientation and position of body segments can be provided.

Table 6.2 – Anatomical coordinate system definitions for the lower limb model.

lower limb part	description
pelvis	midpoint between right and left anterior superior iliac spine.
thigh	midpoint between lateral and medial thigh bone.
knee	medial femoral wpicondyle and lateral femoral wpicondyle.
shank	midpoint between tibia; sural region
angle	malleolus medialis and external Malleolus

Joint angles measurement of low limb was examined with two adult subjects without disabilities or injuries. the proposed method was used to implement human kinematic and kinetic analysis on posture variation from sitting on a chair to standing up. The wearable sensors mounted on shanks, thighs and lumbar are fixed by magic tapes. Before experiment, both subjects were asked to walk on a treadmill for about 5 minutes, to ensure that hey do not feel uncomfortable, then subject start to walk with right side step at three different speeds (0.6 m/s , 0.8 m/s , and 1.3 m/s). Totally, five trials were performed for each waling cycle, as shown in figure 6.9. The human lower limb was represented as an articulated multi-segment system with 9 rigid segments (pelvis, thighs, knees, shanks, and angles). The signals from the sensor systems were sampled at a rate of 100 samples/s , and transferred to PC by the wireless LAN module in the data logger.

Kinematical analysis and measurement for swing motion

Two subject golfers were used, a primary player who has little experience of golf and a mid-level player. Wearable sensor system is placed on the upper body and arms to capture significant motions during the swing. Experiment was conducted on a mid-level player with respect to the wrist rotation and movement of the right leg during swing motion. The sensor was attached to the body by an adjustable holder that prevented slippage, as show in figure 6.11. In addition, two sensor parts were placed on the player's left wrist and thumb. The subjects were asked to perform the golf swing ten times.



Figure 6.11 – Experimental subject and wearable sensor system.

The subject performed swings after first addressing the ball and counter-clockwise rotation of the wrists. also performed a nearly perfect golf swing that has no wrist rotation or out-of-plane movements. For each movement, he were asked to keep his wrist natural throughout the movements. This allows the system to record the motion while achieving consistent angles in different segments of the swing. All of the swings were performed with hitting a practice golf ball made in plastic. The subjects were also asked to perform the swings at a normal speed he used to for experimental consistency.

An extra sensor system was connected to a laptop via wifi module to collect data from lower limb. The data was collected using our tool developed in MATLAB. We followed the procedure for data collection, preprocessing, feature extraction, model generation as described previously. Then collected data was processed offline.

6.4 Results

6.4.1 Validation of Kalman filter for lower limb measurement

In the condition of experiments with and without the Kalman filter, the effectiveness of designed Kalman filter for joint angle compensation was tested. The measured orientation by wearable sensor system was compared with results which were obtained with an optical reference system.

An example of the filter performance is shown in figure 6.12, figure 6.13, and figure 6.14. In these figures, the error represents the magnitude of orientation vector. Difference between the reference angles and the same output of inertial sensors without kalman filtering increased with time.

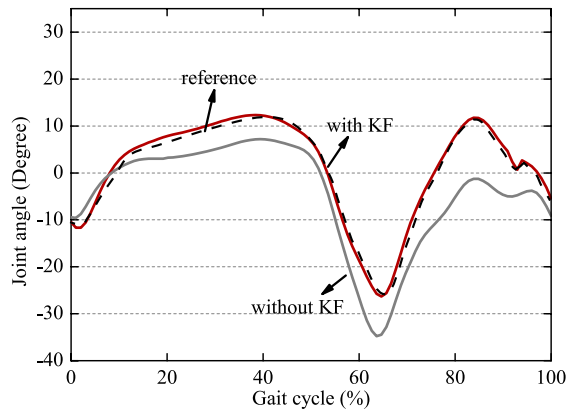


Figure 6.12 – Comparison of the ankle joint angle.

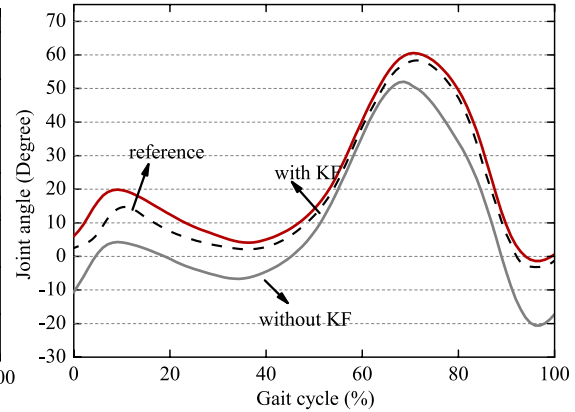


Figure 6.13 – Comparison of the knee joint angle

The magnitude of the orientation drift was defined as the time derivatives of the orientation error. The heading drift was defined likewise as the time derivative of the change in heading error. The average orientation and heading drift over several trials is given in figure 6.15, figure 6.16, and figure 6.17. Joint angle changes as walking speed change in 1 minute walking measurement. Positive values show ankle dorsiflexion angle and flexion angles of the knee and hip.

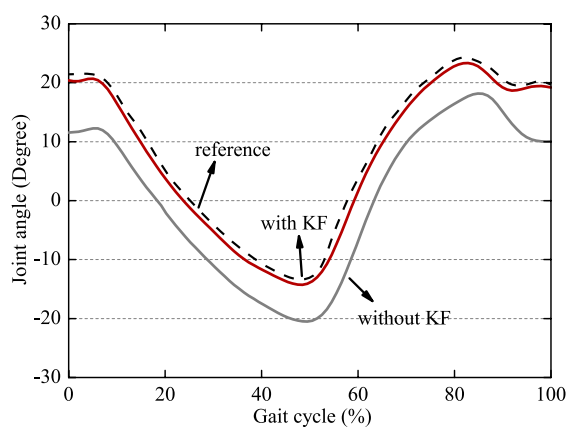


Figure 6.14 – Comparison of the ankle hip angle.

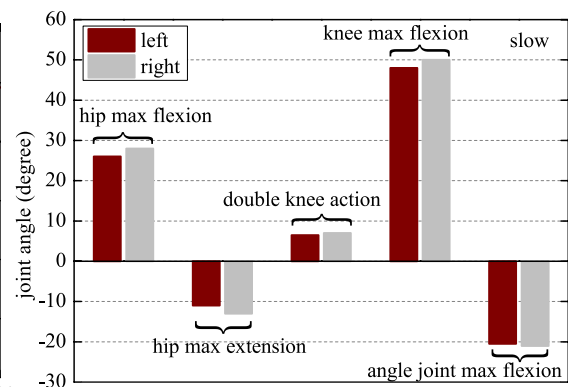


Figure 6.15 – Joint angle measurement at slow walking speed.

The selected joint angles with three kinds of waling speed (0.6 m/s , 0.8 m/s , and 1.3 m/s) were the maximum hip flexion and extension angles, the knee flexion angle in the swing phase.

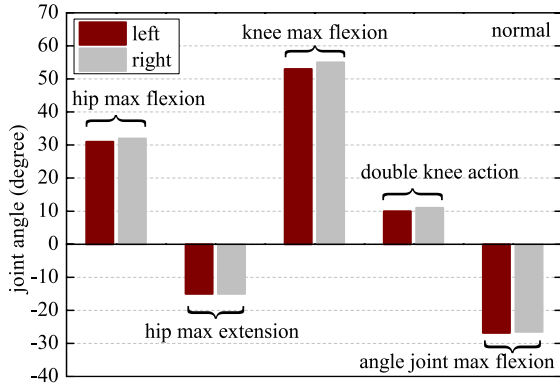


Figure 6.16 – Joint angle measurement at normal walking speed.

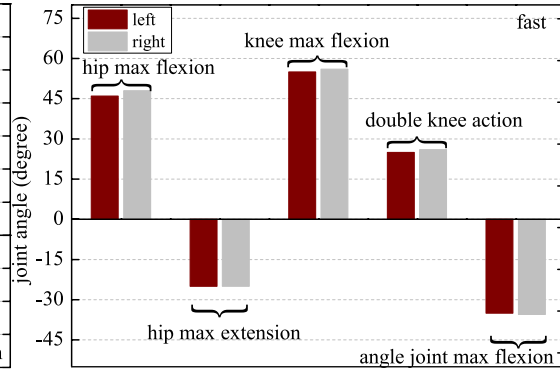


Figure 6.17 – Joint angle measurement at fast walking speed.

6.4.2 Kinematical analysis and measurement for swing motion

The system is applied to the evaluation of golf swing from the rotational measurements and translation estimations. The criteria of golf form were derived from the driver-swing form outlined in golf training textbooks by accomplished world-class golfers [Hogan(1985)] and [Nicklaus(2007)]. Although these criteria were not scientifically established, this system was able to verify the criteria scientifically by quantification of data collected during the golf swing.

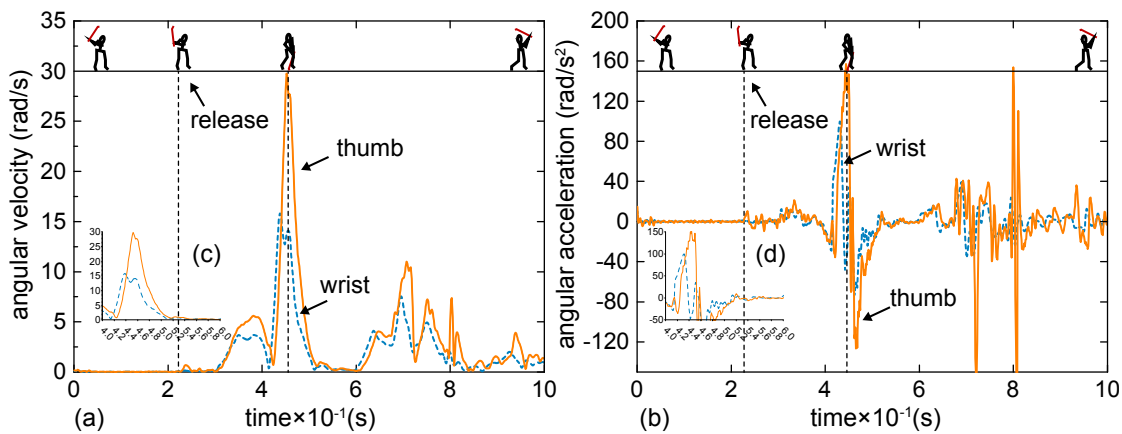


Figure 6.18 – Data from upper sensor system.

As shown in figure 6.18, graph (a) and graph (b) are angular velocity data and angular accel-

eration data averaged over 10 swing of a mid-level golfer for a single golf swing, respectively. Graph (c) and (d) are identical data sets. The x -axis is zoomed from 0.4 s to 0.6 s so that one can see the details at impact position after wrist release. The data was taken while swing a club, with hitting a practice ball. This is done so as to give the subject a comfort feedback like a real swing, and not to complicate this descriptive analysis with the shock of impact. The zero of the time axis is arbitrary and corresponds to a point between the beginning of the downswing and impact.

Figure 6.18 offers an idea of the approximate angular speed of movement of different parts during the downswing. It can be seen that arms move first, and wrists second, and that each sequentially-moving body part moves faster and faster. Before impact, note that thumb are moving much faster than arms and this is an essential feature of a successful swing.

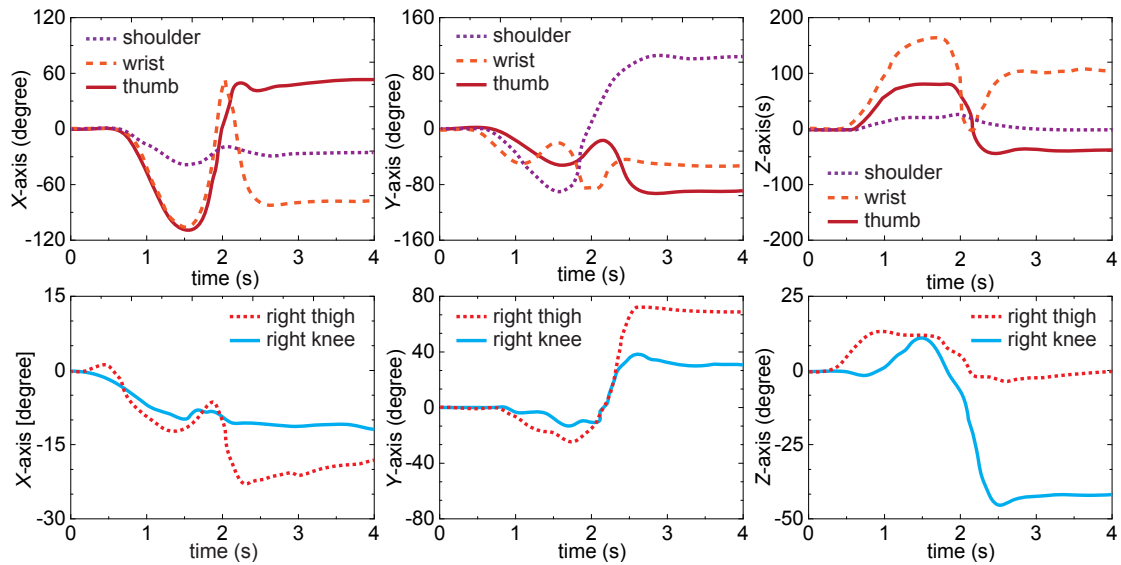


Figure 6.19 – Measurement angles of golf swing in the local coordinate system.

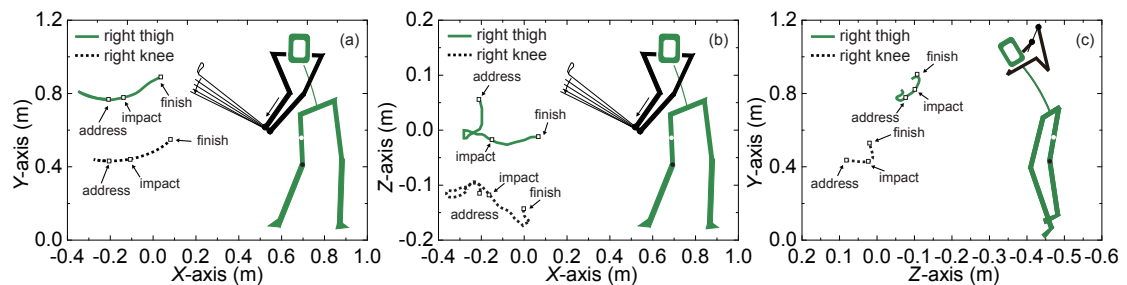


Figure 6.20 – Measurement displacement of golf swing with camera motion capture system. (a) the direction of front; (b) the direction of vertical; (c) the direction of horizon.

According to figure 6.11, lower limb sensor system was attached to the right knee and right thigh by adjustable holder that prevented slippage. Figure 6.19 shows the rotational angle of each part in the local coordinate system, in which curves represents shoulder were measured by camera motion capture system. Figure 6.20 shows the loci of the motion of the right leg and right thigh.

The results appear to be reasonable values. During a golf swing, the position of wrist and upper left arm is higher than that of the left shoulder at the finish. However, this situation did not occur in the model due to an error introduced from the vibration at impact. Before the impact, all motions were accurately measured.

6.5 Discussion

Based on integration of the gyroscope signal, it is clearly shown that the estimation error of Kalman filter is smaller than the orientation results. Measured joint angle patterns were similar to those such as seen commonly in other literatures. As shown in table 6.3 average values of the *RMSE* and γ were improved in the condition of experiment. It was found that

Table 6.3 – Comparison of evaluation results between with and without Kalman filter (*KF*)

		<i>RMSE</i>		γ	
		without <i>KF</i>	with <i>KF</i>	without <i>KF</i>	with <i>KF</i>
hip	subject 1	4.30 ± 0.51	3.67 ± 0.96	0.964 ± 0.009	0.982 ± 0.008
	subject 2	5.75 ± 1.53	3.43 ± 0.78	0.981 ± 0.012	0.990 ± 0.003
	Mean	5.03 ± 1.02	3.55 ± 0.87	0.973 ± 0.011	0.986 ± 0.006
knee	subject 1	4.72 ± 1.37	2.82 ± 0.53	0.981 ± 0.011	0.991 ± 0.002
	subject 2	4.17 ± 1.39	2.70 ± 0.77	0.972 ± 0.007	0.984 ± 0.003
	Mean	4.45 ± 1.38	2.76 ± 0.65	0.977 ± 0.009	0.988 ± 0.003
ankle	subject 1	6.86 ± 1.30	4.30 ± 0.66	0.674 ± 0.092	0.796 ± 0.052
	subject 2	7.04 ± 1.82	4.49 ± 0.54	0.716 ± 0.090	0.789 ± 0.047
	Mean	6.95 ± 1.56	4.40 ± 0.66	0.695 ± 0.092	0.793 ± 0.052

although experiments conducted at different walking speeds, variations of average statistical values were small. Orientation errors obtained without angle compensation are significantly greater than the orientation errors derived from Kalman filter. As shown in figure 6.15, figure 6.16, and figure 6.17, the joint angles increased as walking speed increased. There were no clear differences in other extreme values between walking speed condition.

In figure 6.18, because the signal is a direct measure of the motion of the upper limb, there

are several points in the swing which are easily identified. They include the starting of the backswing, time of maximum speed in the downswing, beginning of release, and impact phase. Note that impact results in a large shock to the system, which helps to identify the exact location of impact. This impact appears as the anomaly seen just to the right of the dash line. As was stated above, during the downswing the upper limb sensor system measures the acceleration of the hands. Thus, the peak near the release point corresponds to a region of rapid acceleration of the hands, and the negative valued minimum near the impact position corresponds to deceleration of the hands.

According to textbooks written by [Hogan(1985)] and [Nicklaus(2007)], an simple criteria associated with the motions of the shoulder, wrists, and thigh part. At the top of the swing, the twisting angle of the shoulder must be 90° and that of the thigh must be 45° . From address position to finish position, translations of thigh, wrists, and shoulder must be minimized. For the quantitative evaluation, motion elements measured must include the angles of the thigh part and the shoulder. Moreover, 3 dimensional translations of every part should be measured.

From the angle around the Y -axis, angles of shoulder and thigh at the top of the swing, as shown in figure 6.19, the ratio of the thigh angle to the shoulder angle was $36^\circ / 83^\circ = 43\%$ for the mid-level golfer, whereas that of the primary golfer was $71^\circ / 89^\circ = 80\%$, meaning the body axis of the novice player did not twist enough. This measurement provides quantification of the expression and criteria for the simple example. Based on figure 6.19 and figure 6.20 the translation motions are given quantitatively. The maximum displacements from the address position for 3 directional motion are compared for two subjects. All of the maximum displacement by the primary player was bigger than those by the mid-level player.

6.6 Summary

In this chapter, the purpose of the present research was to examine the effect of Kalman filter on signal fusion of the wearable sensor system. After that we focus on golf swing, which is hard to be measured. A method for the measurement of golf swing with designed wearable sensor system was described. Based on theoretical simulation and empirical study results, it can be found that:

1. A Kalman filtering based joint angle measurement method with the wearable sensor system was developed. This method successfully reduced joint angle error caused by offset drift of gyroscope. As an alternative method instead of traditional gait analysis system, the results of quantitative human motion analysis based on wearable sensor

system could be helpful to quantitatively evaluate effectiveness of different exercising programs and rehabilitation devices in rehabilitation training.

2. The wearable sensor system accurately measures the golf swing motion of two subjects. The data obtained by this system can be related quantitatively to skill criteria as expressed in respected golf textbooks. Quantitative data for criteria geared toward a primary golfer and a mid-level player are equally useful.

7 Conclusion

7.1 Overview

The aims of this thesis as outlined in Chapter 1 were to investigate the dynamics of the swing of a golf club. The research conducted to address these aims included a comprehensive literature review; the mathematical study on a double pendulum model with respect of release point during downswing phase; the development and validation of the joint kinematics estimation based on a camera motion analysis system; simulation and experimental studies involving a golf swing robot; Kinematical measurement and analysis for golf swing based on developed wearable sensor system were carried out. The purpose of the final chapter is to summarise and to compare the findings of the experimental studies.

7.2 Summary

7.2.1 Dynamic analysis for the release point of the golf swing

The Lagrangian method is used to obtain two coupled differential equations describing the motion of a double pendulum model of golf swing. These equations are simplified by a special treatment of the gravitational torques and are put in a form such that different constant torques applied by the golfer. The equations are solved numerically for various suitable boundary conditions. It is shown that a delayed release technique, using increasing acceleration pattern not to be confused with the natural delay in club shaft release that is introduced into the system by the rotational accelerations of the trunk arm system itself. It was found that the increasing acceleration before release point, using a resistive wrist torque, provided a small benefit in terms of increasing club head speed at impact, but the percentage gain in club head speed was

approximately half that previously reported by other researchers. The increasing acceleration pattern gives the maximum club head speed at impact. Golfers who turn wrists freely or use a negative wrist torque can achieve the optimum ball position by the impact criterion, where the club shaft is vertical at impact when viewed face on. Through the discussion, it can be seen that the derived simple approximate equations give us physical insight of the phenomena at the release point and help us to understand the effect of the club parameters on the dynamic behavior of the double pendulum at the release point.

7.2.2 Motion plan of a golf swing robot

Based on theoretical study on a double pendulum model, related validation research mainly including motion plan has been conducted and solved. Because the number of degrees of freedom of a model is usually equal to the number of the joint actuators. A double degree of freedom golf swing prototype was established to simulate natural release of golfer. The first axis is an active joint, and the second axis is a passive one. The designed control algorithm was realizing by achieving precise impact position and control of impact speed in planning the prototype swing motion. The whole approach builds upon a basic fact that each link of a multi-revolute-joint planar manipulator can be regarded as a pendulum driven by both the active joint torque and the coupling torque in the noninertial translational reference frame attached to itself.

7.2.3 Measurement and analysis of golf swing with wearable sensor system

We have described a wearable sensor system that attaches on golfer's body. Then combined motion of upper limb and lower limb during swing together. It is shown that this relatively simple measurement system (compare to camera motion analysis system) can be interpreted within the context of the double pendulum model of the golf swing. The measurement yields sufficient to calculate the displacement, angle velocities, and angular accelerations along to X , Y , Z -axis, which characterize the orientation of the arms of the double pendulum in the plane ϕ throughout the entire swing. At last, a simple experimental study was conducted to demonstrate how to measure and analysis swing motion with developed wearable sensor system.

Bibliography

- [Aicardi(2007)] M. Aicardi. A triple pendulum robotic model and a set of simple parametric functions for the analysis of the golf swing. *International Journal of Sports Science and Engineering*, 1(2):75–86, 2007.
- [Aminian et al.(2004)Aminian, Trevisan, and Najafi] K Aminian, C Trevisan, and B Najafi. Evaluation of an ambulatory system for gait analysis in hip osteoarthritis and after total hip replacement. *Gait & posture*, 20(1):102–107, 2004.
- [Arai and Tachi(1991)] Hirohiko Arai and Susumu Tachi. Position control system of a two degree of freedom manipulator with a passive joint. *Industrial Electronics, IEEE Transactions on*, 38(1):15–20, 1991.
- [Archer and Castillo(2006)] K.R. Archer and R.C. Castillo. Gait symmetry and walking speed analysis following lower-extremity trauma. *Physical Therapy*, 86(12):1630–1640, 2006.
- [Åström and Furuta(2000)] Karl Johan Åström and Katsuhisa Furuta. Swinging up a pendulum by energy control. *Automatica*, 36(2):287–295, 2000.
- [Awad and Jiang(2007)] M Awad and X Jiang. Incremental support vector machine framework for visual sensor networks. *EURASIP Journal on Applied Signal Processing*, pages 222–222, 2007.
- [Bar-Shalom and Li(1993)] Yaakov Bar-Shalom and Xiao-Rong Li. Estimation and tracking-principles, techniques, and software. *Norwood, MA: Artech House, Inc, 1993.*, 1993.
- [Benini and Farella(2006)] Luca Benini and Elisabetta Farella. Wireless sensor networks: Enabling technology for ambient intelligence. *Microelectronics journal*, 37(12):1639–1649, 2006.
- [Benoit and Ramsey(2006)] Daniel L Benoit and Dan K Ramsey. Effect of skin movement artifact on knee kinematics during gait and cutting motions measured in vivo. *Gait & posture*, 24(2):152–164, 2006.

Bibliography

- [Betzler et al.(2008)Betzler, Shan, and Witte] N. Betzler, G. Shan, and K. Witte. The influence of different golf club designs on swing performance in skilled golfers. pages 253–258, 2008.
- [Budney and Bellow(1982)] D. R. Budney and D. G Bellow. On the swing mechanics of a matched set of golf clubs. *Research Quartely for Exercise and Sport*, pages 185–192, 1982.
- [Cappozzo and Catani(1996)] A. Cappozzo and F. Catani. Position and orientation in space of bones during movement: Experimental artefacts. *Clinical Biomechanics*, 11(2):90–100, 1996.
- [Cerveri and Pedotti(2005)] P. Cerveri and A. Pedotti. Kinematical models to reduce the effect of skin artifacts on marker-based human motion estimation. *Journal of Biomechanics*, 38(11):2228–2236, 2005.
- [Cerveri and Rabuffetti(2003)] P. Cerveri and M. Rabuffetti. Real-time human motion estimation using biomechanical models and non-linear state-space filters. *Medical and Biological Engineering and Computing*, 41(2):109–123, 2003.
- [Chaochao and Yoshio(2007)] Chen Chaochao and Inoue Yoshio. Numerical study on the wrist action during the golf swing. *Sports Engineering*, 10:23–31, 2007.
- [Chen and Hung(2010)] Yin-Jun Chen and Yen-Chu Hung. Using real-time acceleration data for exercise movement training with a decision tree approach. *Expert Systems with Applications*, 37(12):7552–7556, 2010.
- [Chiari and Della Croce(2005)] L. Chiari and U. Della Croce. Human movement analysis using stereophotogrammetry. part 2: Instrumental errors. *Gait and Posture*, 21(2):197–211, 2005.
- [Cochran and Stobbs(1968)] Cochran and Stobbs. The search for the perfect swing. *Heinemann: London*, 1968.
- [Dao and Tho(2014)] Tien Tuan Dao and Marie Christine Ho Ba Tho. Biomechanics of the musculoskeletal system. *John Wiley & Sons*, 2014.
- [De Luca and Oriolo(2002)] Alessandro De Luca and Giuseppe Oriolo. Trajectory planning and control for planar robots with passive last joint. *The International Journal of Robotics Research*, 21(5-6):575–590, 2002.
- [Delp and Loan(1990)] S.L. Delp and J.P. Loan. An interactive graphics-based model of the lower extremity to study orthopaedic surgical procedures. *IEEE Transactions on Biomedical Engineering*, 37(8):757–767, 1990.

- [Dillman(1994)] C. J. Dillman. How has biomechanics contributed to the understanding of the golf swing? science and golfII: proceedings of the 1994 world scientific congress of golf. 1994.
- [E(2006)] Harper T E. Robotic simulation of golfers' swings. 2006.
- [Farrally(1999)] M. R. Farrally. Science and golf III: proceedings of the 1998 world scientific congress of golf. 1999.
- [Farrally and Cochran(2003)] M.R. Farrally and A.J. Cochran. Golf science research at the beginning of the twenty-first century. *Journal of Sports Sciences*, 21(9):753–765, 2003.
- [Fedorcik and Queen(2012)] Gregory G Fedorcik and Robin M Queen. Differences in wrist mechanics during the golf swing based on golf handicap. *Journal of Science and Medicine in Sport*, 15(3):250–254, 2012.
- [Ghasemzadeh et al.(2009)Ghasemzadeh, Loseu, and Jafari] H. Ghasemzadeh, V. Loseu, and R. Jafari. Wearable coach for sport training: A quantitative model to evaluate wrist-rotation in golf. *Journal of Ambient Intelligence and Smart Environments*, 1(2):173–184, 2009.
- [Ghasemzadeh and Loseu(2009)] Hassan Ghasemzadeh and Vitali Loseu. Wearable coach for sport training: A quantitative model to evaluate wrist-rotation in golf. *Journal of Ambient Intelligence and Smart Environments*, 1(2):173–184, 2009.
- [Gluck et al.(2008)Gluck, Bendo, and Spivak] George S Gluck, John A Bendo, and Jeffrey M Spivak. The lumbar spine and low back pain in golf: a literature review of swing biomechanics and injury prevention. *The Spine Journal*, 8(5):778–788, 2008.
- [Heldoorn and Vlasblom(2010)] Thijs Heldoorn and Erik Vlasblom. Analysis of the golf swing. pages 1–5, 2010.
- [Hogan(1985)] Ben Hogan. *Ben Hogan's five lessons: The modern fundamentals of golf*. Simon and Schuster, 1985.
- [Hoshino et al.(2005)Hoshino, Kobayashi, and Yamada] Yohei Hoshino, Yukinori Kobayashi, and Gen Yamada. Vibration control using a state observer that considers disturbances of a golf swing robot. *JSME International Journal Series C*, 48(1):60–69, 2005.
- [Howell(1992)] D. D Howell. The design of filament wound graphite/epoxy golf shafts. *37th International SAMPE symposium*, pages 1392–1405, 1992.
- [Hume et al.(2005)Hume, Keogh, and Reid] P.A. Hume, J. Keogh, and D. Reid. The role of biomechanics in maximising distance and accuracy of golf shots. *Sports Medicine*, 35(5):429–449, 2005.

Bibliography

- [Huntley et al.(2006)Huntley, Davis, Strangwood, and Otto] M.P. Huntley, C.L. Davis, M. Strangwood, and S.R. Otto. Comparison of the static and dynamic behaviour of carbon fibre composite golf club shafts. *Proceedings of the Institution of Mechanical Engineers, Part L: Journal of Materials: Design and Applications*, 220(4):229–236, 2006.
- [Inoue et al.(2003)Inoue, Matusda, and Shibata] Y. Inoue, T. Matusda, and K. Shibata. Estimation of vertical reaction force and ankle joint moment by using plantar pressure sensor. *JSME, Symposium on Human Dynamics (in Japanese)*, pages 57–62, 2003.
- [Iwatsubo et al.(2002)Iwatsubo, Adachi, and Kitagawa] T Iwatsubo, K Adachi, and T Kitagawa. A study of link models for dynamic analysis of golf swing motion. *The Engineering of Sport*, pages 701–707, 2002.
- [J Pansiotand R(2006)] King J Pansiotand R. Towards imagebased modeling for ambient sensing. *In IEEE proceedings of the 5th International Workshop on Wearable and Implantable Body Sensor*, pages 195–198, 2006.
- [James and Burkett(2011)] Daniel A James and Brendan Burkett. An unobtrusive swimming monitoring system for recreational and elite performance monitoring. *Procedia Engineering*, 13:113–119, 2011.
- [Jorgensen(1999)] Theodore P. Jorgensen. The physics of golf. *Springer: New York*, 1999.
- [JR(2002)] Jones JR. A spatial model of the rigid-body club swing. pages 3–17, 2002.
- [Kalman(1960)] Rudolph Emil Kalman. A new approach to linear filtering and prediction problems. *Journal of Fluids Engineering*, 82(1):35–45, 1960.
- [Kaneko and Sato(2000)] Y Kaneko and F Sato. The adaptation of golf swing to inertia property of golf club. *The Engineering of Sport*, pages 469–476, 2000.
- [Keogh et al.(2005)Keogh, Reid, et al.] Justin Keogh, Duncan Reid, et al. The role of biomechanics in maximising distance and accuracy of golf shots. *Sports Medicine*, 35(5):429–449, 2005.
- [King and Yoon(2008)] Kevin King and SW Yoon. Wireless mems inertial sensor system for golf swing dynamics. *Sensors and Actuators A: Physical*, 141(2):619–630, 2008.
- [King et al.(2008)King, Yoon, Perkins, and Najafi] Kevin King, SW Yoon, NC Perkins, and K Najafi. Wireless mems inertial sensor system for golf swing dynamics. *Sensors and Actuators A: Physical*, 141(2):619–630, 2008.
- [King and Atallah(2009)] R.C. King and L. Atallah. Development of a wireless sensor glove for surgical skills assessment. *IEEE Transactions on Information Technology in Biomedicine*, 13(5):673–679, 2009.

- [KR and RE(1985)] Campbell KR and Reid RE. The application of optimal control theory to simplified models of complex human motions: the golf swing. *Biomechanics*, pages 527–538, 1985.
- [Lai et al.(2011)Lai, Hetchl, Wei, Ball, and Mclaughlin] Daniel TH Lai, Mirco Hetchl, XiaoChen Wei, Kevin Ball, and Patrick Mclaughlin. On the difference in swing arm kinematics between low handicap golfers and non-golfers using wireless inertial sensors. *Procedia Engineering*, 13:219–225, 2011.
- [Lampsa(1975)] MA Lampsa. Maximizing distance of the golf drive: an optimal control study. *Journal of Dynamic Systems, Measurement, and Control*, 97(4):362–367, 1975.
- [Lee and Kim(2006)] M. Lee and C. Kim. *Optimum design and validation of a graphite golf shaft based on dynamics of swing*, volume 3. 2006.
- [Li and Tsubokura(2014)] Jing Li and Makoto Tsubokura. Numerical study on the aerodynamics of a golf ball and its comparison with a smooth sphere. *67th Annual Meeting of the APS Division of Fluid Dynamics*, 59(20), 2014.
- [Liu et al.(2011)Liu, Inoue, and Shibata] T. Liu, Y. Inoue, and K. Shibata. Three-dimensional lower limb kinematic and kinetic analysis based on a wireless sensor system. *2011 IEEE International Conference on Robotics and Automation*, pages 842–847, 2011.
- [Liu and Wang(2011)] Tao Liu and Boxiong Wang. Study of magnetic ranging technology in horizontal directional drilling. *Sensors and Actuators A: Physical*, 171(2):186–190, 2011.
- [Liu et al.(2009a)Liu, Inoue, and Shibata] Tao Liu, Yoshio Inoue, and Kyoko Shibata. Development of a wearable sensor system for quantitative gait analysis. *Measurement*, 42(7): 978–988, 2009a.
- [Liu et al.(2009b)Liu, Inoue, and Shibata] Tao Liu, Yoshio Inoue, and Kyoko Shibata. Development of a wearable sensor system for quantitative gait analysis. *Measurement*, 42(7): 978–988, 2009b.
- [Liu et al.(2010a)Liu, Inoue, and Shibata] Tao Liu, Yoshio Inoue, and Kyoko Shibata. A wearable force plate system for the continuous measurement of triaxial ground reaction force in biomechanical applications. *Measurement Science and Technology*, 21(8):085804, 2010a.
- [Liu et al.(2010b)Liu, Inoue, and Shibata] Tao Liu, Yoshio Inoue, and Kyoto Shibata. A wearable ground reaction force sensor system and its application to measurement of extrinsic gait variability. *Sensors*, 10:10240–10255, 2010b.

Bibliography

- [Liu and J(2000)] Y Liu and Williams J. Optical bend sensor based on measurement of resonance mode splitting of long-period fiber grating. *Photonics technology letters, IEEE*, (5): 531–533, 2000.
- [Lu and O'Connor(1999)] T.-W. Lu and J.J. O'Connor. Bone position estimation from skin marker co-ordinates using global optimisation with joint constraints. *Journal of Biomechanics*, 32(2):129–134, 1999.
- [Lu et al.(2004) Lu, Zhang, Wu, and Li] Y. Lu, J.Z. Zhang, Q.M.J. Wu, and Z.-N. Li. A survey of motion-parallax-based 3-d reconstruction algorithms. *IEEE Transactions on Systems, Man and Cybernetics Part C: Applications and Reviews*, 34(4):532–548, 2004.
- [MacKenzie(2005)] SJ MacKenzie. Understanding the role of shaft stiffness in the golf swing (dissertation). 2005.
- [Maltby(1995)] R. D. Maltby. Golf club design, fitting, alteration, and repair: the principles and procedures. *Maltby Enterprises.*, 1995.
- [McHardy and Pollard(2005)] A. McHardy and H. Pollard. Muscle activity during the golf swing. *British Journal of Sports Medicine*, 39(11):799–804, 2005.
- [McHardy and Pollard(2006)] A. McHardy and H. Pollard. Golf injuries: A review of the literature. *Sports Medicine*, 36(2):171–187, 2006.
- [Milne and Davis(1992a)] R.D. Milne and J.P. Davis. The role of the shaft in the golf swing. *Journal of Biomechanics*, 25(9):975–983, 1992a.
- [Milne and Davis(1992b)] R.D. Milne and J.P. Davis. The role of the shaft in the golf swing. *Journal of Biomechanics*, 25(9):975–983, 1992b.
- [Ming and Kajitani(2003a)] A. Ming and M. Kajitani. A new golf swing robot to simulate human skill - accuracy improvement of swing motion by learning control. *Mechatronics*, 13(8-9 SPEC.):809–823, 2003a.
- [Ming et al.(2006) Ming, Furukawa, Teshima, Shimojo, and Kajitani] A. Ming, S. Furukawa, T. Teshima, M. Shimojo, and M. Kajitani. A new golf swing robot to simulate human skill-learning control based on direct dynamics model using recurrent ann. *Mechatronics*, 16(7):443–449, 2006.
- [Ming and Kajitani(2003b)] Aiguo Ming and Makoto Kajitani. A new golf swing robot to simulate human skill—accuracy improvement of swing motion by learning control. *Mechatronics*, 13(8):809–823, 2003b.
- [Miura(2001)] K. Miura. Parametric acceleration – the effect of inward pull of the golf club at impact stage. *Sports Engineering*, 4(2):75–86, 2001.

- [Moré(1978)] Jorge J Moré. The levenberg-marquardt algorithm: implementation and theory. In *Numerical analysis*, pages 105–116. Springer, 1978.
- [Mulla et al.(2011)] Mulla, Sepulveda, and Colley] Mohamed R. AL Mulla, Francisco Sepulveda, and Martin Colley. An autonomous wearable system for predicting and detecting localised muscle fatigue. *Sensors*, 11:1542–1557, 2011.
- [Nakanishi et al.(2000)] Nakanishi, Fukuda, and Koditschek] Jun Nakanishi, Toshio Fukuda, and Daniel E Koditschek. A brachiating robot controller. *Robotics and Automation, IEEE Transactions on*, 16(2):109–123, 2000.
- [Nesbit(2005)] S.M. Nesbit. A three dimensional kinematic and kinetic study of the golf swing. *Journal of Sports Science and Medicine*, 4(4):499–519, 2005.
- [Nesbit(2007)] S.M. Nesbit. Development of a full-body biomechanical model of the golf swing. *International Journal of Modelling and Simulation*, 27(4):392–404, 2007.
- [Nesbit and Serrano(2005)] S.M. Nesbit and M. Serrano. Work and power analysis of the golf swing. *Journal of Sports Science and Medicine*, 4(4):520–533, 2005.
- [Nicklaus(2007)] Jack Nicklaus. *Golf my way*. Simon and Schuster, 2007.
- [Park and Chaffin(2008)] Woojin Park and Don B Chaffin. Memory-based human motion simulation for computer-aided ergonomic design. *Systems, Man and Cybernetics, Part A: Systems and Humans, IEEE Transactions on*, 38(3):513–527, 2008.
- [Penner(2003)] A.R. Penner. The physics of golf. *Reports on Progress in Physics*, 66(2):131–171, 2003.
- [Pickering and Vickers(1999)] Pickering and Vickers. On the double pendulum model of the golf swing. *Sports Engineering*, 2(3):161–172, 1999.
- [RJ and BD.(1981)] Neal RJ and Wilson BD. 3d kinematics and kinetics of the golf swing. *Biomechanics*, pages 325–331, 1981.
- [S(1996)] McGuan S. Exploring human adaptation using optimized, dynamic human models. 1996.
- [Schwarz and Mateus(2012)] Loren Arthur Schwarz and Diana Mateus. Recognizing multiple human activities and tracking full-body pose in unconstrained environments. *Pattern Recognition*, 45(1):11–23, 2012.
- [Spoor and Veldpaus(1980)] C.W. Spoor and F.E. Veldpaus. Rigid body motion calculated from spatial co-ordinates of markers. *Journal of Biomechanics*, 13(4):391–393, 1980.
- [Sprigings and Mackenzie(2002)] Eric J. Sprigings and S. J. Mackenzie. Examining the delayed release in the golf swing using computer simulation. *Sports Engineering*, 5(1):23–32, 2002.

Bibliography

- [Sprigings and Neal(2001)] Eric J. Sprigings and Robert J. Neal. Shifting a portion of the clubshaft's mass distally: does it improve performance? *Sports Engineering*, 4(1):15–21, 2001.
- [Sprigings and Neal(2000)] Eric.J. Sprigings and Robert J. Neal. An insight into the importance of wrist torque in driving the golfball: A simulation study. *Journal of Applied Biomechanics*, 16(4):356–366, 2000.
- [Suzuki and Haake(2006)] S Suzuki and SJ Haake. Multiple modulation torque planning for a new golf-swing robot with a skilful wrist turn. *Sports Engineering*, 9(4):201–208, 2006.
- [Suzuki and Inooka(1997)] Soichiro Suzuki and Hikaru Inooka. Golf-swing robot emulating a human motion. In *Robot and Human Communication, 1997. RO-MAN'97. Proceedings., 6th IEEE International Workshop on*, pages 28–33, 1997.
- [Tsujiuchi and Koizumi(2002)] N. Tsujiuchi and T. Koizumi. Analysis of the influence of golf club design on the golf swing. *The Engineering of Sport*, pages 537–544, 2002.
- [Turner and Hills(1998)] A. B. Turner and N. J. Hills. A three-link mathematical model of the golf swing. *Science and Golf*, pages 3–12, 1998.
- [Vaughan(1981)] Christopher L. Vaughan. Three-dimensional analysis of the forces and torques applied by a golfer during the downswing. 1981.
- [White(2006)] R. White. On the efficiency of the golf swing. *American Journal of Physics*, 74(12):1088–1094, 2006.
- [Williams(1967)] D Williams. The dynamics of the golf swing (with conclusions of practical interest). *The Quarterly Journal of Mechanics and Applied Mathematics*, 20(2):247–264, 1967.
- [Williamson and Andrews(2001)] R Williamson and BJ Andrews. Detecting absolute human knee angle and angular velocity using accelerometers and rate gyroscopes. *Medical and Biological Engineering and Computing*, 39(3):294–302, 2001.
- [Winfield and Tan(1996)] D.C. Winfield and T.E. Tan. Optimization of the clubface shape of a golf driver to minimize dispersion of off-center shots. *Computers and Structures*, 58(6):1217–1224, 1996.
- [Winter(2009)] David A Winter. *Biomechanics and motor control of human movement*. John Wiley & Sons, 2009.
- [Woltring(1980)] Herman J Woltring. Planar control in multi-camera calibration for 3-d gait studies. *Journal of Biomechanics*, 13(1):39–48, 1980.
- [Zhang(2000)] Zhengyou Zhang. A flexible new technique for camera calibration. *Pattern Analysis and Machine Intelligence, IEEE Transactions on*, 22(11):1330–1334, 2000.

- [Zhou and Hu(2008)] Huiyu Zhou and Huosheng Hu. Human motion tracking for rehabilitation—a survey. *Biomedical Signal Processing and Control*, 3(1):1–18, 2008.

A Appendix-List of Publications

Academic Journal Papers

1. Li Zhiwei, Inoue Yoshio, Kodama Shunta, Liu Tao, and Shibata Kyoko. Dynamic analysis for the release point of the golf swing (Effect of parameters of golf club and player), Transactions of the JSME (in Japanese), Vol. 80, No. 820 (2014), DOI: 10.1299/transjsme.2014dr0385.
2. Li Zhiwei, Inoue Yoshio, Kodama Shunta, Liu Tao, and Shibata Kyoko. Dynamic analysis for the release point of the golf swing (Effect of acceleration pattern of the down swing), Transactions of the JSME (in Japanese). accepted
3. Li Zhiwei, Inoue Yoshio, Liu Tao, and Shibata Kyoko. A Swing Robot to Evaluate Wrist Rotation in Golf Swing base on a Wearable Sensor System. Journal of Intelligent & Robotic Systems. prepare to submit.

International Conference Proceedings

1. Li Zhiwei, Inoue Yoshio, Kodama Shunta, and Shibata Kyoko. The Effect of Swing Pattern on the Release Point and the Club Head Speed. 2014, The 3th Joint International Conference on Multibody System Dynamics (Busan, Korea).
2. Li Zhiwei, Tanaka Tsuyoshi, Inoue Yoshio, and Kyoko Shibata. A Novel Approach of Gait Analysis Based on a Wearable Sensor System. 2014, International Symposium on Test Automation and Instrumentation (Beijing, China).